University of Bergen

Masterthesis
in Measurement Science and Instrumentation

Characterization of a neutral helium beam for helium microscopy

---

Author:
Truls Andersen

Supervisor:
Prof. Bodil Holst
Co-Supervisor:
Dr. Sabrina Eder

June 29, 2015

Abstract

Neutral helium beam microscopy is a new development in scientific instrumentation where neutral helium atoms are utilized to image a sample. The main advantage of using neutral helium is the significantly smaller energy the atoms have for a given wavelength compared to electrons and photons. For example, the energy for a helium atom with a 0.1 nm wavelength is $\sim 0.02 \ eV$. The energies for an electron and a photon with similar wavelength are $\sim 150 \ eV$ and $1.2 \cdot 10^4 \ eV$, respectively. Other advantages include the facts that the atoms are both inert and neutral. This means that the samples remain undamaged, and therefore the direct imaging of fragile, insulating samples is possible. Due to the low polarization coefficient and neutrality of the helium beam, only classical optical elements such as mirrors or lenses can be used to manipulate the beam. The neutral helium beams are created in a supersonic expansion through a small nozzle. A skimmer is utilized in front of the beam to select the central part of the beam. This beam skimmer is a crucial part in the microscope because it defines the "object" that is focussed by the optical element (mirror or lens) onto the probe to be investigated. Given the geometrical limitations of such a microscope instrument, the size of the skimmer effectively determines the focal spot size through a demagnification factor, and thus the obtainable resolution of the microscope.

The main focus of this thesis has been to characterize neutral helium beams created using skimmers of three varying shapes and six different diameters. Skimmers with orifice diameters of 4 μm, 5 μm, 18 μm, 100 μm, 120 μm and 390 μm have been utilized to determine the center line intensity beam characteristics, and the 4 μm and 390 μm skimmers have been utilized in addition for the determination of the virtual source size characteristics and the determination of the beam's monochromaticity. Microskimmers have been used very little until now and so far there are only two papers in the literature investigating their properties. The work presented in this thesis can thus really be considered ground breaking.

The results obtained for this thesis show some surprising effects. Most importantly, the results show that the center line intensities for the small skimmers do not follow the theoretical models. It was observed that the reduction of the skimmer orifice causes a dramatic drop in the center line intensity. However, the time of flight measurements show that the monochromaticity of the beam is not influenced by the size of the skimmer orifice. The virtual source measurements show that we obtain a smaller virtual source size utilizing a small skimmer orifice diameter, which is really puzzling. The results presented here show that the ideal situation of utilizing a small skimmer opening diameter to gain a small focal spot size in a helium microscope proves to be challenging. While the monochromaticity of the beam remains unchanged, the reduced center line intensity affects the microscopes ability of actually generating an image. Overall the results presented show that a design change is probably required for the microscope.

Abstrakt

Nøytral helium stråle mikroskopi representerer en nyskapning innen vitenskapelig instrumentering der nøytrale helium atomer benyttes for å danne et bilde av en prøve. Hovedfordelen med bruk av nøytral helium er den vesentlig lavere energien atomene har ved en gitt bølgelengde sammenlignet med elektroner og fotoner. Eksempelvis vil energien for et helium atom være $\sim 0.02\ eV$ ved en bølgelengde på $0.1\ nm$. Energien for elekroner og fotoner vil være henholdsvis $\sim 150\ eV$ og $1.2 \cdot 10^4\ eV$ ved samme bølgelengde. Andre fordeler inkluderer det faktum at atomene er både inert og nøytrale. Det betyr at prøven forblir uskadet, og at direkte bildebehandling av skjøre, isolerende prøver er mulig. Grunnet den lave polariserende koeffesienten og nøytraliteten i heliumstrålen kan kun klassiske optiske elementer som linser og speil benyttes for å manipulere strålen. Den nøytrale heliumstrålen dannes av en supersonisk ekspansjon gjennom en liten dyse. En skimmer foran strålen selekterer den sentrale delen av strålen. Denne skimmeren er en avgjørende del i mikroskopet fordi den definerer «objektet» som fokuseres av det optiske elementet (speil og linse) på proben som skal undersøkes. Gitt den geometriske begrensningen for et slikt mikroskop, vil skimmerens størrelse faktisk bestemme fokalpunktets størrelse ved hjelp av en demagnifiserende faktor, og følgelig mikroskopets oppnåelige oppløsning.

Hovudfokuset for denne oppgaven har vært å karakterisere nøytrale heliumstråler dannet ved bruk av skimmere med tre varierende former og seks forskjellige diametre. Skimmere med åpningsdiameter på $4\ \mu m$, $5\ \mu m$, $18\ \mu m$, $100\ \mu m$, $120\ \mu m$ og $390\ \mu m$ er benyttet for bestemmelse av senterlinje intensitet for strålen, og $4\ \mu m$ og $390\ \mu m$ skimmere ble brukt for bestemmelse av den virtuelle kildens karakteristikker og bestemmelse av strålens monokromatisitet. Mikroskimmere har hittil vært benyttet i liten grad, og så langt er det kun 2 publikasjoner i litteraturen som har forsket på deres egenskaper. Arbeidet som presenteres i denne opgaven kan derfor betraktes som banebrytende.

Resultatene som er oppnådd i denne oppgaven viser noen overraskende effekter. Viktigst er at senterlinje intensitet resultatene for små skimmere ikke følger teoretiske modeller. Det ble observert at reduksjon i skimmeråpning fører til et dramatisk fall i senterlinje intensitet. Flukttidsmålinger viser imidlertid strålens monokromatisitet ikke påvirkes av skimmeråpningens størrelse. De virtuelle kilde målingene viser at man oppnår en mindre virtuell kilde størrelse når det brukes en liten skimmeråpning diameter, noe som er underlig. Resultatene som presenteres her viser at den ideelle situasjonen ved å benytte en liten diameter skimmeråpning for å oppnå et lite fokalpunkt i et helium mikroskop, har vist seg å være utfordrende. Mens strålens monokromatisitet forblir uendret, vil den reduserte senterlinje intensiteten påvirke mikroskopets evne til å faktisk generere et bilde. Generelt sett viser de presenterte resulatene at en endring i mikroskopets design sannsynligvis er nødvendig.

Acknowledgements

I would like to start by thanking my supervisor Professor Bodil Holst for allowing me to partake in this project and granting me the opportunity to complete such a challenging task. For allowing me to work with MAGIE and for all your help during the writing of this thesis.

A special thanks goes out to Sabrina Eder for all the help you have provided me during my thesis. You were always there when I got stuck and needed help, and you endured all my not-always-so clever questions. I truly would not be where I am today if it was not for you, thank you.

Thomas Kaltenbacher, thank you for all your help with my Matlab issues and for all your help teaching me concepts I did not fully understand.

I would like to thank my fellow students and office room-mates Sigve Naustdal and Mang Li for all the great moments we shared, for all the discussions and breaks we had during the semester to the weeks-long exam preparations we shared with blood and tears. I would also like to thank Håkon Eidsvåg, Kristoffer Johansen, André Adelsten Søvik and Kristian Austreim for the five years we spent doing a degree in physics. It has been an epic journey for us all, and it has been a fantastic five years since we first started our bachelor degrees.

I am extremely appreciative of the support I have had from my girlfriend, Jessica Strickland. You were always there for me when I needed you and you always supported and motivated me throughout my long days.

Finally I would like to thank my parents and my two brothers. You have supported me all the way, offering help and motivation. Without you this would not have been possible.

Contents

List of Tables

List of Figures

INTRODUCTION

Ever since the first description of a one-lens optical microscope by the Dutch scientist Zacharias Jansen in 1595 [1], microscopes have been enormously important in scientific exploration. The main purpose of microscopes remains the same: to observe objects that are too small for the human eye to see. The first microscopy technique utilized the wavelength of light, and is still a very useful microscopy technique today, although huge improvements have been made from the first design. Unfortunately, the optical microscopes can only go so far before they reach a limit in achievable resolution. As stated by the Abbe criterion [2] the minimum resolvable size of an object is $\lambda/2$, where λ is the wavelength of the imaging probe (i.e. light beam). To overcome the resolution limit of the optical microscopes, other imaging probes were tested. In 1931 Ernst Ruska developed the electron microscope [3], the first matter wave microscope. Instead of using light, this microscope utilizes electrons to obtain an image of a sample, but due to the high particle energy (typically at least 1 keV) it is difficult to image fragile samples. Furthermore, the electrons carry a charge, which means that insulating samples cannot normally be imaged without conducting coating. Various attempts have been made to overcome this in the environmental scanning electron microscope, but charging effects remains a big challenge in electron microscopy.

A solution to overcome the limitations of the electron microscope is to utilize a less energetic neutral particle probe. In 1911, Louis Dunoyer was the first man to generate a direct beam of neutral atoms, a so-called molecular beam [4]. In 1951, Arthur Kantrowitz and Jerry Grey developed a molecular beam produced by a gas expansion through a small pinhole nozzle [5]. This was the first molecular source that was not effusive and thus it had a much narrower velocity distribution and higher intensity than previous expansions [4]. Remarkable progress was made within vacuum technology the following years, and this paved the way for the development of supersonic beams and ultra-high vacuum based detection systems in the early 1970s [6]. Since the late 1970s, helium beam scattering has been an important technique to investigate the structural and dynamic properties of surfaces [7].

The idea of using helium as an imaging technique has been around for about 20 years. The biggest advantage setting neutral helium microscopy aside from the other existing microscopy techniques is the low energy of the beam particles. Helium has a lower energy

than most other particle probes, for example the energy is about 50 meV for a wavelength around 0.05 nm. Electron microscopes and X-ray microscopes both operate with a much higher beam energy, in the keV range or even higher [8]. In fact, the energy of the neutral helium atoms is so low that there is absolutely no penetration of the beam into the sample. Another big advantage of using neutral helium is the neutrality of the atoms. This avoids any charging of the investigated sample. These two key features allow the microscope to investigate the surface of metals, insulators, semiconductors and even extremely fragile samples without inflicting any damage. Helium is a noble gas, which means it is also chemically non-reactive, or inert. Therefore the neutral helium will not have any chemical reactions with the sample [9].

The creation of the neutral helium beam consists of a few different elements: a high pressure reservoir and a nozzle where the helium exits into the high-vacuum pressure chamber creating the free-jet expansion, and also a small conically shaped piece called a skimmer. The skimmer serves several purposes. It is the separating element between the source chamber and the neighbouring ultra high vacuum chamber and therefore works as a differential pumping stage. The skimmer also confines the helium beam by only selecting helium atoms with a straight forward trajectory, deflecting all other helium atoms with trajectories strongly deviating from the beam line. Lastly, the size of the skimmer orifice determines the final focus spot size achievable by the microscope. A small focus spot size is desired in the microscope, and thus a small skimmer orifice is ideal. The first images using helium atoms as an imaging probe were obtained by Holst et al. in 2008 [10]. These images were created by selecting the central part of the beam with a microskimmer and focus it with a zoneplate onto a grating structure. The image was obtained as a shadow image in transmission. In 2011, Witham and Sánchez created the first image in reflection using a very simple set-up with a microskimmer placed close to the sample and no focussing elements [11]. Both methods are presently limited by the intensity. The work of this thesis has been to investigate in a systematic manner how the beam characteristics are affected by the size of the skimmer orifice. Virtual source measurements, center line intensity measurements and time of flight measurements were conducted to determine the size of the virtual source, the intensity of the center line and the monochromaticity of the beam at different skimmer sizes. Very little prior work on a systematic characterization on microskimmers has been done to date. The first paper demonstrating the use of microskimmers was presented by Brown et al. in 1997 [12]. These results were limited by source alignment challenges (nozzle position relative to the skimmer), but suggested that good velocity distributions could be obtained. The microskimmers were then used in various microscopy experiments as described above and it was noted that the intensity seemed small, but this was ascribed largely to other effects and no proper beam characterization was done.

In 2006 DePonte et al. used a microskimmer source in Speckle pattern experiments [13]. They characterized the beam and determined the size of the virtual source at different pressures for a single microskimmer orifice. The task of this thesis work was to perform

the first systematic study of beams created with microskimmers. A unique advantage compared to earlier experiments is that a new source developed by Eder et al [14] could be used for the experiments. This source allows the skimmer and nozzle to be aligned relative to each other with sub-micron precision. It is the only source of this kind in the world.

Chapter 2 of the thesis discusses the theory required to understand the operating principles of the helium microscope, including the beam properties and principles of neutral molecular detection. Chapter 3 describes the microscope used during this thesis, and the various vacuum pumps and pressure gauge systems utilized by MAGIE (short for Makroskopische Gitter Experimente), one of the neutral microscopes under the care of the Nanophysics group at the University of Bergen. Chapter 4 describes the methods of the three experiments conducted during the work of this thesis. Chapter 5 presents the results from the experiments and compares them with theoretical simulations and previously obtained results from the Nanophysics group and other research groups (i.e. the DePonte group mentioned above). Finally, chapter 6 presents a conclusion. Three appendices have also been included. Appendix A presents the Matlab scripts used for the analysis of the various experiments. Appendix B presents check-lists on how to perform the various experiments with MAGIE, and finally appendix C presents uncertainty calculations.

THEORY

Some obstacles are encountered when a microscope utilizing a beam of neutral helium atoms is being created. Due to the neutrality of the atoms, the creation and focusing of the beam provides a challenge. This chapter focuses on the theoretical aspects of a molecular beam utilizing neutral helium. The wave nature of atoms and important properties, such as the de Broglie wavelength, are discussed, and the basic theory behind neutral beam sources is introduced. Properties such as beam intensity, terminal velocity, velocity distribution and virtual source are explained and finally common principles of neutral molecular beam detection is discussed.

2.1   The wave nature of atoms

Early in the 20th century, quantum mechanics was introduced in the world of physics, and with it came the concept that particles behave according to the particle-wave-duality. In 1905 Einstein postulated that light is absorbed as localized packets when illuminating a metal in his famous paper about the photoelectric effect [15]. The packets would have an energy:

$$E = h \cdot \nu \tag{2.1}$$

where ν is the frequency of the light and h is Planck's constant [16]. This phenomenon was later verified experimentally by Arthur Compton, and thus it was confirmed that light behaved with both wave- and particle-like properties. This validated Louis de Broglie's hypothesize claiming that all particles exhibit wave-like properties, and he postulated the equation now known as the de Broglie equation [17]:

$$\lambda = \frac{h}{p} \tag{2.2}$$

where λ is the particles wavelength, h is Planck's constant and p is the particle momentum. Equation (2.2) states that a particle acts like a wave with wavelength λ. This implies that particles are subject to diffraction and interference.

2.1.1   De Broglie wavelength of helium atoms

Using equation (2.3) we can describe the relation between the velocity v_t of our helium atoms and the wavelength:

$$\lambda = \frac{h}{p} = \frac{h}{m \cdot v_t} \longrightarrow v_t = \frac{h}{m \cdot \lambda} \tag{2.3}$$

where Planck's constant h is equal to $6.6261 \cdot 10^{-34}\ J \cdot s$ and the helium mass m equal to $6.647 \cdot 10^{-27}\ kg$. One of the largest advantages of the neutral helium microscope is the low energy of the atoms. The particle's kinetic energy is given by:

$$E = \frac{m \cdot v^2}{2} \tag{2.4}$$

Having a wavelength of 0.5 Å, which can easily be achieved with a nozzle temperature of $T \sim 380\ K$, the energy of the helium atoms is $E_{He} \sim 0.08\ eV$. Comparing this energy to that of an electron microscope, where the electrons have the same wavelength of 0.5 Å, the energy is $E_e \sim 600\ eV$. If we had an X-ray with with same wavelength, the energy of the wave would be $E_{X-ray} \sim 24000\ eV$. The much lower energy shows that the neutral helium atoms are less destructive than both electrons and X-rays of the same wavelength.

2.2   Neutral beam sources

The neutral (helium) beam sources used for helium microscopy are created by the expansion of a gas from a high pressure reservoir into vacuum through a small orifice (nozzle). The properties of such a beam will depend on the mean free path of the gas molecules and the expansion orifice. We can distinguish between two extreme cases. If the mean free path is significantly larger than the orifice diameter of the nozzle, hardly any collisions will take place as the atoms escape the nozzle. A beam generated like this is referred to as an effusive beam and it has an energy distribution similar to that of the reservoir gas. The velocity distribution of an effusive beam can be expressed as [18] :

$$F\left(v_x\right) = \frac{2}{\alpha^4} \cdot v_x^3 \cdot e^{-\left(\frac{v_x^2}{\alpha^2}\right)} \tag{2.5}$$

where v_x is the mean velocity at point x. The factor α is given as:

$$\alpha = \sqrt{\frac{2 \cdot k_b \cdot T}{m}}$$

where k_b is Boltzmann's constant, T is the reservoir temperature and m is the atomic mass of the beam particles. Equation (2.5) is a Maxwell-Boltzmann distribution, and thus the average velocity of the atoms can be given by:

$$\vec{v} = \sqrt{\frac{8 \cdot k_b \cdot T}{\pi \cdot m}} \tag{2.6}$$

The other extreme case occurs when the mean free path of the gas molecules is significantly smaller than the nozzle diameter. This occurs when either the pressure within the reservoir

is increased, or if the nozzle's orifice diameter is reduced. This case is called the free-jet expansion, or supersonic expansion, and it creates a high intensity beam with a small velocity spread [19]. The velocity distribution of a free-jet expansion beam along the beam axis is given by [20]:

$$f\left(v_x\right) = \sqrt{\frac{m}{2 \cdot \pi \cdot k_b \cdot T_\parallel}} \cdot e^{-\left(\frac{m \cdot (v_x - v_t)^2}{2 \cdot k_b \cdot T_\parallel}\right)} \tag{2.7}$$

where $T_\parallel$ is the temperature of the beam along the beam axis and v_t is the average terminal velocity within the particle beam:

$$v_t = \sqrt{\frac{5 \cdot k_b \cdot T}{m}} \tag{2.8}$$

The velocity distributions for the effusive and free-jet expansion beams, equations (2.5) and (2.7) respectively, are plotted in figure (2.1).
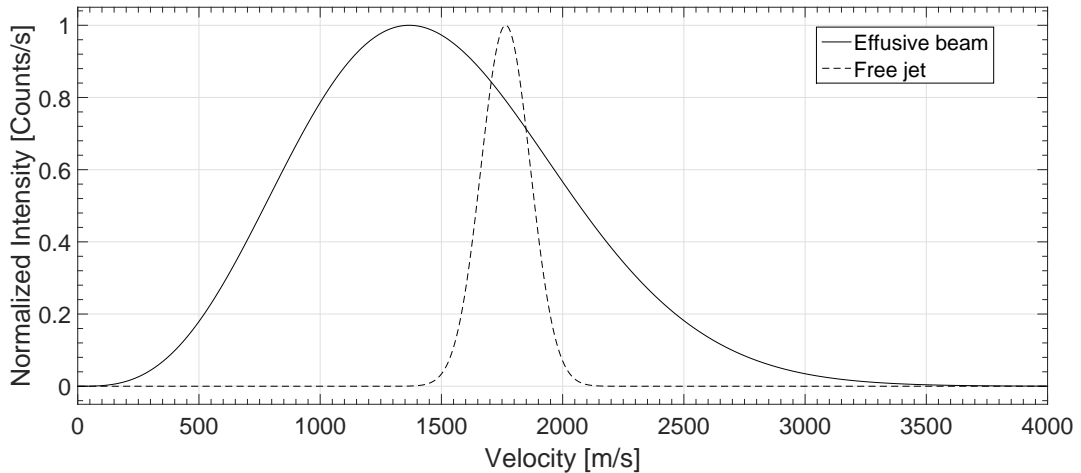
Figure 2.1: *shows the velocity distribution for an effusive and a free-jet beam expansion with a reservoir temperature of* 300 *K. The free-jet expansion exits the nozzle at 10 times the speed of sound and is shown to have a more narrow velocity distribution than the effusive beam expansion. Figure is modelled after figure 2.2 in reference [18].*

2.2.1 Free-jet expansion

The discussion is restricted to short and converging nozzles, so that we can assume our flow to be isentropic and the expansion adiabatic [20][21], meaning that energy loss and friction can be neglected. The nozzle is regarded as the main reservoir of the gas, where the gas has a temperature T and a pressure p_0. The ambient pressure outside the nozzle p_a is typically a high vacuum pressure such that $p_a \ll p_0$. Two different flow regimes are entered over the expansion area, the first one right after the gas leaves the nozzle. Here the gas flow is in the continuum flow regime [22]. This means that the gas density and hence the collision frequency is sufficiently high such that the equilibrium is maintained throughout the expansion process [18]. As the beam expands the density decreases, causing the collision frequency of the molecules to go down. This is the start of the second flow regime, free

molecular flow. In this region the gas molecules are in a (nearly) collision-free environment and follow straight trajectories from the transition area of the flow regimes. The boundary between continuum flow and molecular flow is called the 'Quitting surface' [22], and is shown in figure (2.2). Given that the molecules follow (nearly) straight trajectories after passing the quitting surface, geometrical optics can be applied to the beam [22]. Various attempts have been made to model the free-jet expansion, for example references [22] and [23]. However, it is a very complex problem. In particular the transition region between continuous and molecular flow is difficult to model. Including the effects of a background gas and skimmer interactions are even more difficult. Work is ongoing, and some of the theoretical results are used to compare with the experiments in the results chapter of this thesis (see chapter (5)). A detailed discussion of these simulations is beyond the scope of this thesis.

By tracing the molecules backwards towards the nozzle in straight lines from the quitting surface, there will be a point where all the molecules define a minimum cross-sectional area called the 'virtual source plane'. This plane defines the size of the source, and is discussed in more detail in section (2.2.2).
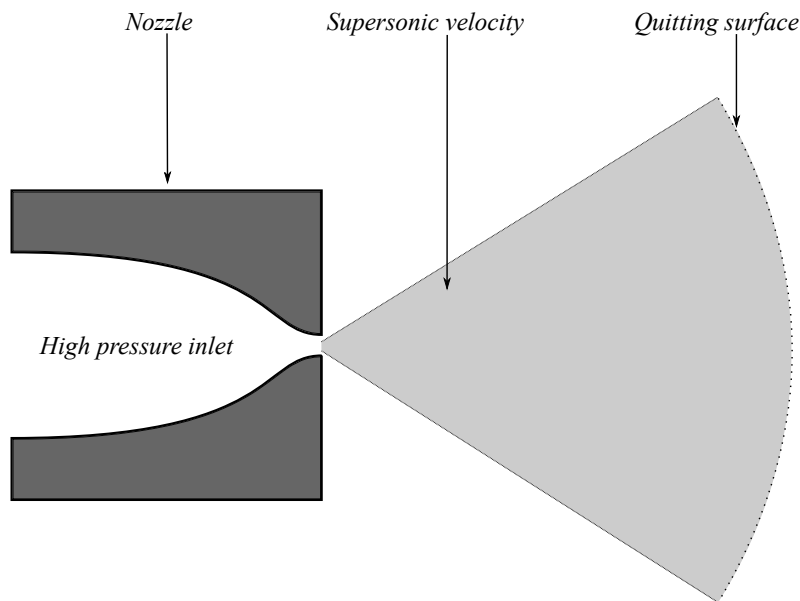
Figure 2.2: *shows the free-jet expansion in the molecular flow region for an expanding gas coming from a high pressure reservoir through a pinhole nozzle. The so-called 'quitting surface' is shown. This illustration was modelled from figure (10) in reference [11].*

2.2.2 Virtual source

During the free-jet expansion the mean free path of the atoms is small compared to the nozzle diameter. This means that the gas leaving the nozzle exits into the continuum flow regime. Figures (2.2) and (2.3) show this regime as the light grey area. As the expansion progresses the particles start to drift apart and the particle density decreases. As the particles drift from each other, the collision frequency of the particles will diminish

and eventually the particles enter the molecular flow regime. In this region the particles travel in straight trajectory lines where no further collisions take place [22]. The boundary between the continuum flow regime and the molecular flow regime is named the *quitting surface*, and is shown is both figures (2.2) and (2.3). This region is located at a distance of a few nozzle diameters from the nozzle. As the particles pass the quitting surface they follow straight trajectory lines. Geometrical optics can be applied to these beam particles and they can all be traced back to a point called the virtual source plane [14]. See figure (2.3).
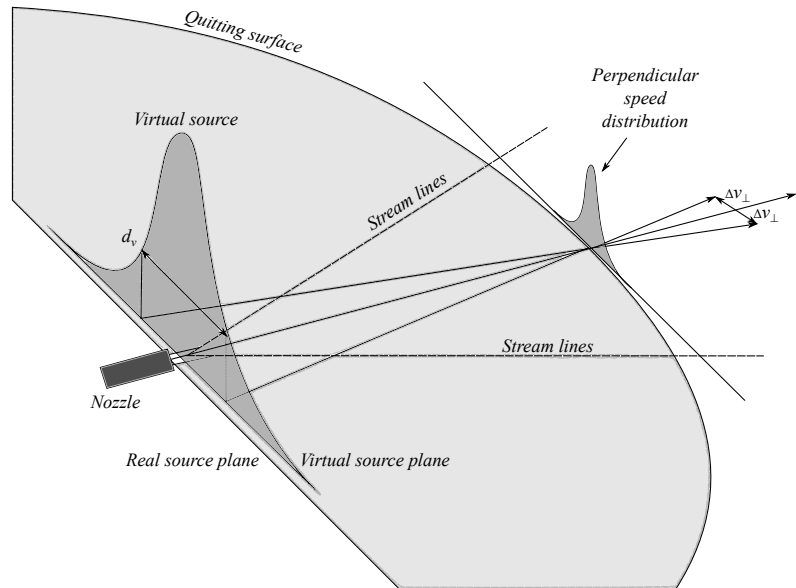
Figure 2.3: *shows a representation of a free-jet expansion and the virtual source. The helium atoms exits the nozzle into the source chamber in the continuum flow regime. After a few nozzle diameters the atoms cross the "quitting surface" and enters the molecular flow regime, where no collisions take part and the atoms travel in straight lines. These lines can be traced from the "quitting surface" backwards onto a plane that is perpendicular to the beam direction, z. By taking into account the velocity distribution perpendicular to the beam lines $\Delta v_\perp$, a spatial distribution function is obtained. This is what is known as the virtual source. The figure is modelled after figure 1 in reference [22].*

2.2.3 Beam intensity

The intensity of the beam is a very important factor. The free-jet expansion is a much 'sharper' distribution than the effusive expansion, meaning less intensity is lost to the sides. By being able to calculate the beam intensity at a distance from the nozzle, we can predict what the intensity should be expected to be before the actual measurement is taken. The beam's center line intensity can be estimated by finding the particle density at the nozzle. This can be done using the ideal gas law which provides a good approximation for an inert helium gas [21]:

$$n_0 = \frac{p_0}{k_b \cdot T} \tag{2.9}$$

where n_0 is the particle density at the nozzle, p_0 is the reservoir pressure, k_b is Boltzmann's

constant and T is the nozzle temperature. At a distance x away from the nozzle, the particle density can be calculated as [20]:

$$n\left(x\right) = 0.155 \cdot n_0 \cdot \left(\frac{d}{x}\right)^2 \tag{2.10}$$

where x is the distance from the nozzle and d is the diameter of the nozzle opening. Using equation (2.10) we can calculate the expected count-rate N at the detector to be

$$N = n\left(x\right) \cdot v_t \cdot A_{ap} \cdot f_{eff} \tag{2.11}$$

where v_t is the terminal velocity (see equation (2.8)), A_{ap} is the area of the scanning aperture, and f_{eff} is the detector efficiency.

2.2.4 Terminal velocity

Up until now we have assumed that the free-jet expansion can be treated as isentropic and adiabatic. Following these assumptions, the molecule's energy will depend on the temperature of the nozzle. The adiabatic assumption requires the conservation of the sum of enthalpy and the kinetic energy of direct mass flow as the gas expands into vacuum [18]:

$$h_e = \frac{1}{2} \cdot m \cdot v_t^2 = h_0 \tag{2.12}$$

where h_e is the enthalpy of the expanded gas per atom, m is the mass of the beam atoms, v_t is the mean velocity of the atoms, often called the terminal velocity, and h_0 is the enthalpy of the gas in the source reservoir per atom. For an ideal mono-atomic gas, h_0 is given by:

$$\begin{aligned} h_0 &= c_p \cdot T \\ &= \frac{\gamma}{\gamma - 1} \cdot k_b \cdot T \\ &= \frac{5}{2} \cdot k_b \cdot T \end{aligned} \tag{2.13}$$

where c_p is the constant pressure molar heat capacity, γ is the heat capacity ratio (for mono-atomic gasses this is equal to 5/3), k_b is Boltzmann's constant and T is the nozzle temperature [18]. By assuming that the gas fully expands into the vacuum, h_e in equation (2.12) can be set equal to 0. By inserting equations (2.12) and (2.13) into each other, we end up with the following:

$$\frac{5}{2} \cdot k_b \cdot T = \frac{1}{2} \cdot m \cdot v_t^2 \tag{2.14}$$

We see that equation (2.8) contains both the terminal velocity v_t and the nozzle temperature T, and thus we can show that the terminal velocity depends solely on the nozzle temperature T:

$$v_t = \sqrt{\frac{5 \cdot k_b \cdot T}{m}} \tag{2.8}$$

2.2.5 Speedratio

As discussed in section (2.2) the free-jet expansion velocity distribution is given as:

$$f\left(v_x\right) = \sqrt{\frac{m}{2 \cdot \pi \cdot k_b \cdot T_{\parallel}}} \cdot e^{-\left(\frac{m \cdot (v_x - v_t)^2}{2 \cdot k_b \cdot T_{\parallel}}\right)} \tag{2.7}$$

This velocity distribution has the standard deviation:

$$\sigma\left(v_x\right) = \sqrt{\frac{k_b \cdot T_{\parallel}}{m}} \tag{2.15}$$

The full width at half maximum corresponds to the spread of the velocity Δv_t, and this depends on the standard deviation of the distribution. The full width at half maximum is given by as:

$$\Delta v_t = 2 \cdot \sqrt{2 \cdot ln\left(2\right)} \cdot \sigma\left(v_x\right) \tag{2.16}$$

A common way of expressing the velocity distribution of the beam is by a factor called the *speedratio*. The speedratio depends solely on parameters that can be measured in a time of flight experiment, and is defined as [24]:

$$S = 2 \cdot \sqrt{ln\left(2\right)} \cdot \frac{v_t}{\Delta v_t} \tag{2.17}$$

2.2.6 Principles of neutral helium atom detection

Three main requirements should be fulfilled to have an ideal detector for neutral beam detection [24]:

1. The detector should give information about all the beam properties, i.e. intensity, chemical composition, kinetic and internal energy distribution

2. The detector should have an efficiency that is almost the same for all species

3. The detector should be able to discriminate against beam particles from residual vacuum background gas

No detector has been developed (to date) that fulfil all the requirements given above. The real detectors that are used for neutral beam detection can be grouped into three categories:

Ionization detectors
The ionization detectors have three main parts: an ion source that ionizes the neutral particles as they enter the detector, a mass filter that selects the desired ions as a function of their mass-to-charge ratio, and finally an ion detector to count the number of incident ions [25]. MAGIE utilizes an ionization detector, and this is described in section (3.2.5).

Laser-based detectors
The laser-based detectors are applied for spectroscopic detection of different atomic and

molecular species, and utilizes state selective detection [26]. This type of detector is not utilized by either MAGIE or NEMI (the other neutral helium microscope under the care of the Nanophysics group at the University of Bergen).

Accumulation detectors

The accumulation detectors work on the principle of measuring the increase in pressure as a tube is filled with atoms (a so-called Pitot tube). As the beam enters the accumulation chamber through a small pinhole entrance in front of the chamber, there will be an accumulation of atoms in the chamber. There will also be a diffusion of atoms through the small pinhole entrance, and at some point an equilibrium between the entering atoms and the diffusion out through the pinhole will be reached. A sensitive pressure measurement gauge can now measure the equilibrium pressure, as a measure for the beam intensity [27]. NEMI utilizes an accumulation detector.

HELIUM MICROSCOPE - MAGIE

This chapters starts by introducing the principle of scanning transmission neutral helium beam microscopy and then it provides a detailed description of the neutral helium microscope set-up. The five ultra-high vacuum chambers on MAGIE are subsequently described as they are encountered by the particle beam travelling along the beam path, starting with the source chamber. Following the source chamber is the chopper chamber holding the chopper disc. Then the mirror chamber, the piezo chamber and the detector chamber are described. Finally descriptions of the various vacuum pumps and measurement gauges used on MAGIE are presented.

3.1 Basic principle of scanning transmission helium beam microscopy

Figure (3.1) shows the basic principle of the scanning transmission neutral helium beam microscope. The neutral helium beam is created by a free-jet expansion into ultra-high vacuum, as described in section (2.2.1), from a nozzle with a diameter of 10 μm. A microskimmer selects the central part of the beam and a Fresnel zoneplate focuses it to a spot of minimal size (in the image) [28]. The image plane is located at a certain distance downstream of the zoneplate. Geometric optics can be applied and hence the Lens equation can be used to determine the position of the focused beam [29]:

$$\frac{1}{f} = \frac{1}{g} + \frac{1}{b} \tag{3.1}$$

where f is the focal length of the zoneplate, g is the distance from the source to the zoneplate, and b is the distance from the zoneplate to the image (image plane). The magnification factor is given by [30]:

$$M = \frac{b}{g} \tag{3.2}$$

While investigating a sample, the sample is located at the piezo table which is in the image plane. The sample is scanned in both X and Y direction perpendicular to the beam, and the detector picks up the helium atoms that pass through the sample. It is important to note that due to the low energy of the helium atoms, no atoms will penetrate through the

sample. Therefore, only free-standing structures can be imaged with scanning transmission helium beam microscopy. By scanning the sample and recording the intensity, a shadow image is obtained due to the non-penetrating nature of the helium atoms. For the beam characterization done in this thesis, there has been no imaging done, meaning that the zoneplates have been removed and there is no sample in the sample holder.
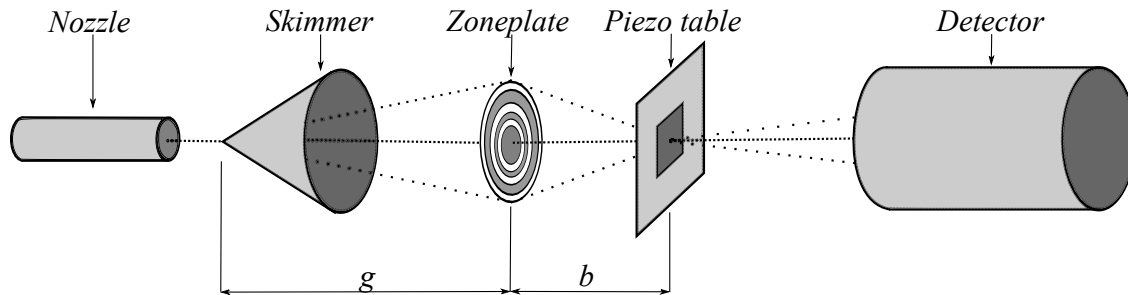
Figure 3.1: *illustrates the principle of scanning transmission neutral helium beam microscopy. A free-jet expansion is created and expands from the nozzle, where the central part of the expansion is selected by the skimmer (straight forward trajectory helium atoms). The selected beam is focused onto the sample by use of a zoneplate, and the helium atoms passing through the free-standing structured sample are counted by the detector.*

3.2 Design

This section gives an introduction to the design of the neutral helium beam microscope, MAGIE, that has been used to conduct all measurements for the work of this thesis. MAGIE is controlled via a Labview program, and a detailed description for the whole apparatus can be found in reference [31]. All the vacuum chambers of MAGIE are kept under high- to ultra-high vacuum. The different parts of the microscope can be split into five main chambers:

- Source chamber

- Chopper chamber

- Mirror chamber

- Piezo chamber

- Detector chamber

There are also two pumping stages, namely pumping stage 1 (PST1) and pumping stage 2 (PST2) to help maintain a good vacuum in the source and piezo chamber. A schematic of the microscope apparatus is shown in figure (3.2) including all of the chambers and the two pumping stages. Figure (3.3) shows a picture of the MAGIE apparatus.
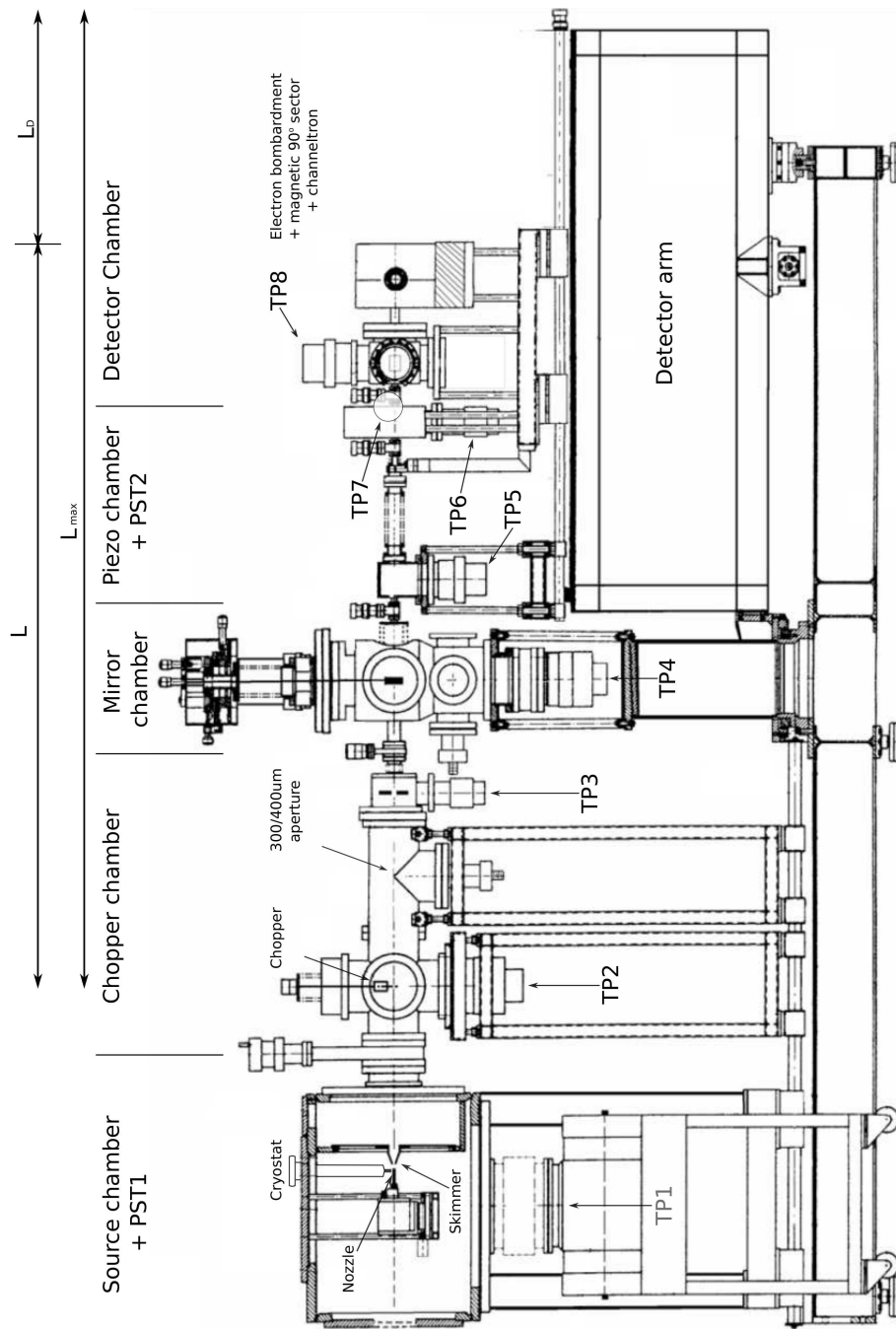
Figure 3.2: *shows a schematic of the neutral helium beam microscope MAGIE which has been used for all experiments conducted during this thesis. All the vacuum chambers are constantly kept under ultra-high vacuum. During measurements the source chamber holds a high-vacuum due to the high flow of helium from the source into the source chamber. Eight different turbo molecular pumps are shown in the figure, respectively named as TP1 to TP8. The two additional pumping stages, named PST1 and PST2, are also shown. PST1 is connected to the source chamber where there is a high flux of helium atoms coming from the expansion. PST2 is connected to the piezo chamber where the piezo table and sample is located. The chopper chamber contains a chopper disc used for time of flight measurements. The distance from the chopper disc to the detector is given by $L = L_{max} - L_D$, where L_{max} is the maximum length, obtained when the movable detector is positioned at zero, as far away as possible. L_D is the position of the detector and can be read off a scale on the side of the detector arm. The distance used for all measurements in this thesis has been $L_D = 710mm$. The detector arm can be rotated up to $90°$.*
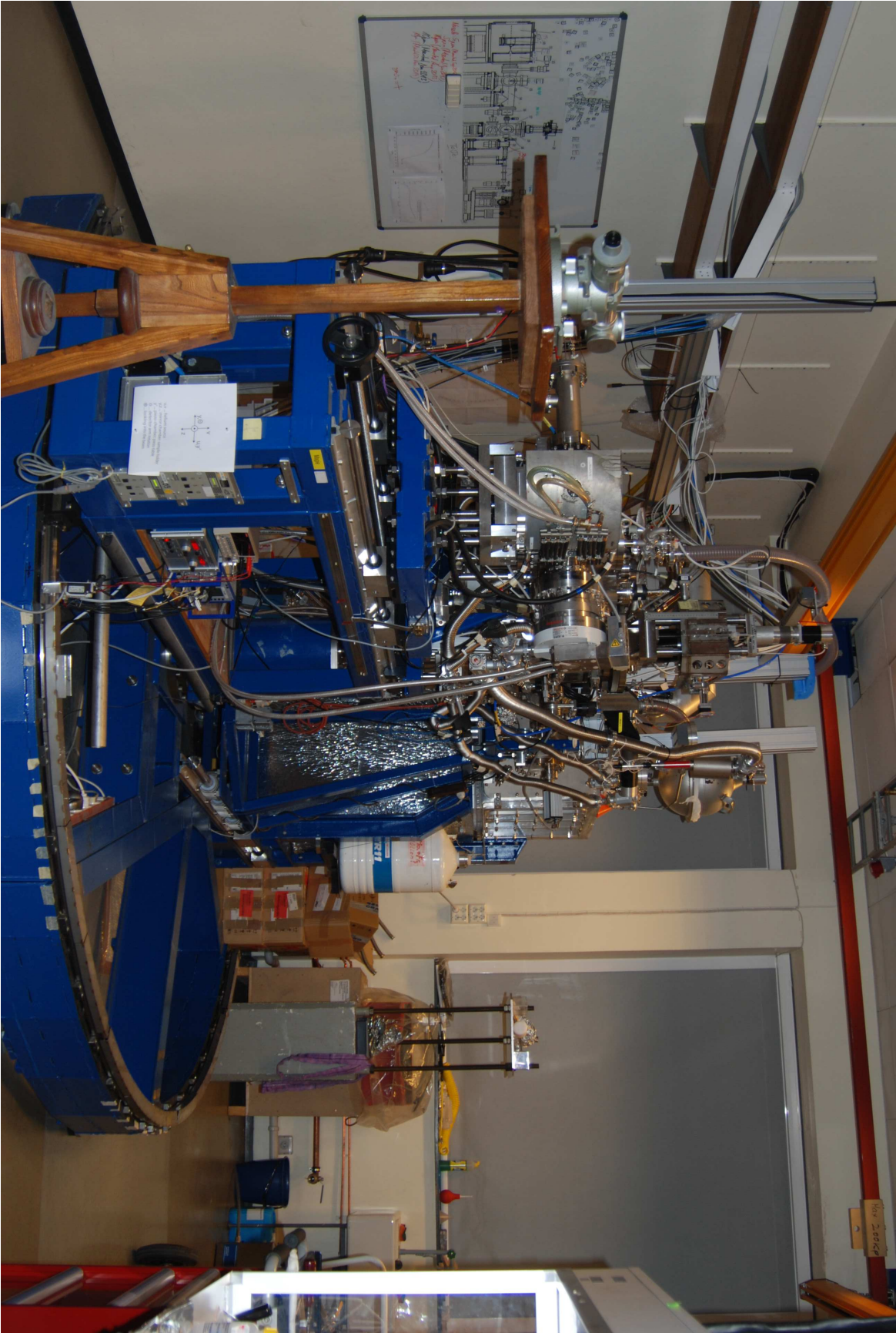
Figure 3.3: *shows an image of the neutral helium microscope MAGIE where all measurements for this thesis have been conducted.*

3.2.1 Source Chamber

The creation of the helium beam takes place in the source chamber, where a high-pressure gas bottle provides a source pressure reservoir of up to $200 \ bar$. During measurements the vacuum in the source chamber is in the range of $p_a < 1 \cdot 10^{-4} \ mbar$ and is sustained by a large turbo molecular pump able to pump $3600 \ L/s$. The helium coming from the high pressure reservoir exits through a small pinhole nozzle into the low-pressure source chamber vacuum. The ratio between the high-pressure reservoir and the vacuum of the chamber is big enough to cause the helium atoms to exit the nozzle with a free-jet expansion. The nozzle used in MAGIE throughout this thesis has an orifice diameter of $10 \pm 1 \ \mu m$. There is a continuous leak of helium into the chamber through this nozzle, thus requiring the high pumping speed from the molecular turbo pump. The free-jet expansion creates what is called a virtual source which is explained in section (2.2.2). The central part of the expansion is selected by a skimmer mounted opposite of the nozzle. As the name suggests, this part skims and collimates the helium beam. The skimmer is explained in section (3.2.1.1). The standard distance between the nozzle and the skimmer in MAGIE is $11.6 \ mm$. The nozzle can be moved either closer or further away from the skimmer. The maximum distance it can be moved is mechanically limited to $\pm 6 \ mm$ from the standard position. A cryostat is also part of the source chamber and is used to cool down the temperature of the beam using liquid nitrogen. As previously mentioned, pumping stage 1 (PST1) is also connected to the source chamber to maintain a good vacuum, and to make a smaller gradient between the source chamber and the chopper chamber.

3.2.1.1 Skimmer

The skimmer selects the central part of the expansion. After the expansion, when the particles reach the so-called quitting surface, where all atomic collisions cease, the skimmer selects the straight forward trajectory helium atoms. The skimmer is a conically shaped aperture and is interchangeable in the microscope. Besides selecting the straight forward trajectory helium atoms, the skimmer also has the purpose of transferring the helium beam into the better vacuum of pumping stage 1 without disturbing the expansion region [32]. The skimmer can have different shapes and orifice diameters. As part of this thesis, three different skimmer types have been used, each type having two different orifice diameters.

Glass skimmer
The glass skimmers have a copper conical body and a glass tip. The glass skimmers are more fragile than the beam dynamic (see section (3.2.1.1)) and Kurt (see section (3.2.1.1)) skimmers, and must be handled with more care than the others. The glass tips of the glass skimmers are created by pulling capillary tubes into fine pipette tips. This is a technique originally invented for patch clamping which is used in medicine [30], but it is also used to create the glass skimmers utilized by MAGIE and other similar apparatuses [12]. The glass skimmer is a rigid structure and the entire skimmer has to be changed if a different orifice diameter is to be used. A detailed description of how the glass skimmers are made can be found in reference [28].

The glass skimmers used in this thesis had two different orifice diameters, namely a $4 \pm +0.1$ μm orifice and an $18 \pm +0.1$ μm orifice. Figure (3.4) shows a picture of a 5.6 μm orifice diameter glass skimmer, while figure (3.5) shows the schematic illustration of the glass skimmer and copper cone body.

Figure 3.4: shows an image of a glass skimmer with 5.6 μm opening
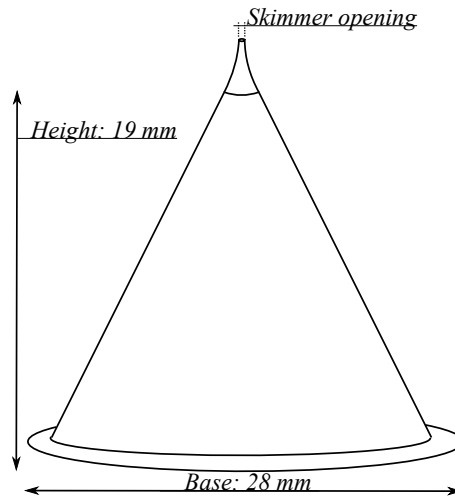
Figure 3.5: shows a schematic of the glass skimmer

Beam dynamic skimmer

The beam dynamic skimmer has a conical shape with a small orifice in front, and is made out of nickel. The structure is robust and easy to handle, but rigid so that the entire skimmer has to be changed if a different orifice diameter is to be used.

The beam dynamic skimmers used in this thesis had two different orifice diameters, namely a 120 ± 5 μm orifice and a 390 ± 5 μm orifice diameter. Figure (3.6) shows a picture of the 390 μm orifice diameter beam dynamic skimmer, while figure (3.7) shows the schematic illustration of the beam dynamic skimmers.
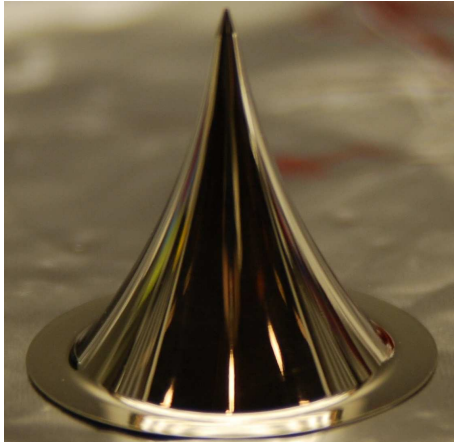
Figure 3.6: shows an image of a beam dynamic skimmer with 390 μm opening
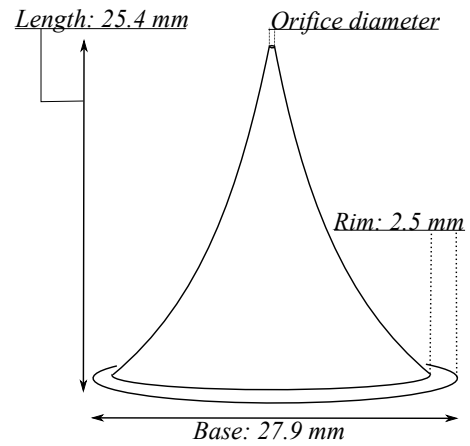
Figure 3.7: shows a schematic of the beam dynamic skimmers

Kurt skimmer

The Kurt skimmer is the newest acquired skimmer-type and it is unique because it is more convenient to use than the glass and the beam dynamic skimmers. It comprises a metal cone with a top part that can be removed. When the top is removed, the orifice diameter can be changed by an exchangeable pinhole aperture located in the small slot. The possibility of changing just the small aperture and not the entire skimmer makes the Kurt skimmer versatile and convenient to use. In contrast to the glass and beam dynamic skimmer, the Kurt skimmer has a flat top with a 0.5 mm hole before the small pinhole aperture is encountered. The Kurt skimmer is robust and easy to handle.

The Kurt skimmer used in this thesis has had two different pinhole apertures with different orifice diameters, namely a 5 ± 1 μm orifice and a 100 ± 5 μm orifice diameter. Figure (3.8) shows a picture of the Kurt skimmer containing a 5 μm pinhole aperture, while figure (3.9) shows a schematic illustration of the Kurt skimmer.
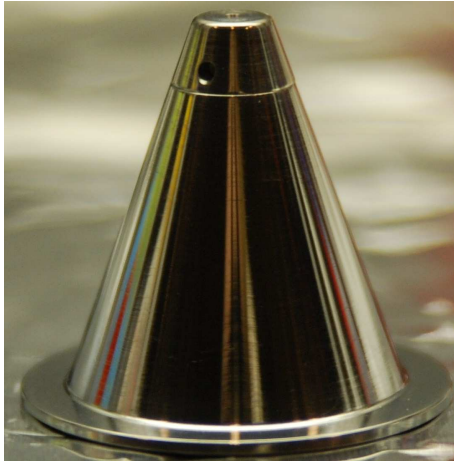
Figure 3.8: shows an image of a Kurt skimmer containing a 5 μm pinhole aperture
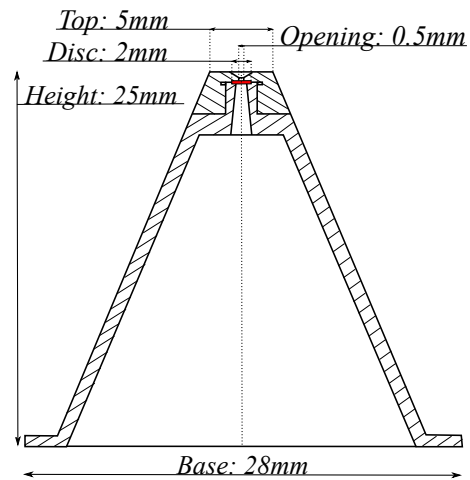
Figure 3.9: shows a schematic of the Kurt skimmers

3.2.1.2   Why use helium

The main reason for using helium for the free-jet expansion, in contrast to other gas particle beams, is due to the fact that helium has a low mass. Equation (2.2) shows that the wavelength is inversely proportional to the mass, which implies that a lower mass particle has a larger wavelength. With this larger wavelength, the zones in the zoneplates can be larger [28]. An additional advantage is that due to specific quantum mechanical properties of helium the velocity distribution in the free-jet helium expansion is particularly narrow [19].

Helium also has other advantages, such as having a very low contribution to the background gas in vacuum. Other gases suitable for using as a imaging probe have a much higher background, making helium an ideal gas to use. Helium is a mono-atomic will not cluster unless the temperature is very low or the pressure very high. Overall, the advantages of having a helium beam are [9][8]:

- Exceptionally high degree of monochromaticity

- No charging of the sample

- No intrusion into the sample due to the low energy

- No sample damage due to low energy

- A chemically inert beam, meaning that there will be no chemical reactions of deterioration of the samples

- The beam can be expanded for very high pressures without leading to clustering

There are challenges involved with utilizing a helium particle beam in comparison to other gases. Due to the high ionization energy of helium, 24.5 eV, it is challenging to ionize

the helium atoms so that they can be detected in a mass spectrometer. The difficulty of ionizing the helium atoms results in a decreased sensitivity of the detector, making a poor signal-to-noise ratio. The helium gas is also difficult to pump from a chamber with a turbo molecular pump because of the small size and light mass. As mentioned in chapter (3.2.1), there is a constant leak of helium from the nozzle into the source chamber. The helium can diffuse back through a running turbo molecular pump, making it hard to maintain a low background, for example in the detector chamber. For that reason the detector chamber has it own backing system.

3.2.2   Chopper Chamber

The main objective of this chamber is to make it possible to perform time of flight measurements of the helium beam to determine the beams velocity spread/monochromaticity. The chamber holds a metal disc which rotates with a set frequency f_{ch}. Two small slits located on the chopper disc chop the helium beam into small beam packages where the lengths of the packages are defined by the chopper frequency and the slit width. As the beam is cut, the beam package continues to travel along the beam path towards the detector which is located at a distance L (see figure (3.1)) from the chopper disc. After passing the chopper disc each beam package travels subsequently undisturbed through the rest of the ultra high vacuum set-up. At the end of the beam line, the flight time of the beam packages is recorded time-resolved. Due to the difference in the particles velocity, the recorded flight time spectrum shows a distribution of arrival times which can be connected to the beams speed distribution. This can be explained as more energetic and faster atoms reaching the detector before the slower atoms, and thus creating a difference in the arrival time of the atoms. Therefore, time of flight measurement provide information about the terminal (mean) velocity v_t (see section 2.2.4) and the the velocity distribution Δv_t. This is a way of measuring the degree of monochromaticity of the beam, which is often expressed by the speedratio S (see section (2.2.5)). Good monochromaticity, and therefore high speedratios, are a requirement for diffraction experiments and beam focusing with Fresnel zoneplates. The time of flight method is described in detail in section (4.2).

3.2.2.1   Chopper disc

The chopper disc is essential for the time of flight measurements, and a schematic is shown in figure (3.11). As the disc rotates with a set frequency, the beam is cut into packages by two slits located opposite each other on the chopper disc. Note that this method would also work with one slit, but the two slit version enables us to create two beam packages per rotation and therefore reduces the measurement time. The slits have a trapezoidal shape (see figure (3.10)) where the width at the top of the slit is 1 ± 0.025 mm and the bottom 3.67 ± 0.025 mm. The entire chopper disc can be moved in or out of the beam line by a vertical translation stage. Since the slits have trapezoidal shape, it enables us to vary the chopper slit width between 1 mm and 3.67 mm by adjusting the translational chopper position in respect to the beam line. This position is referred to as chopper position ε, and can be directly read off the translation stage's scale. At a chopper position of

$\varepsilon \sim 1.005\ inches$, the beam hits the edge of the slit, where the width w of the slit is at its smallest (1 mm). Moving the chopper disc further down increases the slit width w correspondingly up to the maximum of 3.67 mm. For the velocity distribution measurements done during this thesis, a series of time of flight measurements have been conducted over a range of chopper positions, starting from $\varepsilon = 0.66\ inches$ and ending at $\varepsilon = 1.05\ inches$. The method is described in section (4.2.3).

The distance from the bottom edge of the slit to the position where the beam is located on the slit, as a function of the chopper position ε, is described by the equation below (see figure (3.10)):

$$r_m = \varepsilon_{edge} - \varepsilon \qquad (3.3)$$

where ε_{edge} is the chopper position when the beam is at the bottom edge of the slit, and ε is the current chopper position. The uncertainty of equation (3.3) comes from the accuracy of the translation stage scale. This scale is relatively accurate and has an uncertainty of $\Delta(\varepsilon) = 0.0005\ inches$. Knowing the uncertainty of the chopper position, we can calculate the uncertainty of r_m by applying equation (C.2):

$$\Delta(r_m) = \sqrt{(\Delta(\varepsilon_{edge}))^2 + (-\Delta(\varepsilon))^2} \qquad (3.4)$$

The radius from the center of the chopper disc to the position of the beam on the slit with respect to the chopper position ε is given by:

$$r_{ch} = r_b + r_s - r_m \qquad (3.5)$$

where r_b is the radius from the center of the chopper disc to the bottom of the chopper slit and has a value of $59 \pm 0.025\ mm$, and r_s is the length of the slit, which is $10 \pm 0.025\ mm$. Applying equation (C.2) to equation (3.5) we find the uncertainty of the chopper radius:

$$\Delta(r_{ch}) = \sqrt{(\Delta(r_b))^2 + (\Delta(r_s))^2 + (-\Delta(r_m))^2} \qquad (3.6)$$

where the uncertainty of r_b and r_s is 0.025 mm representing the manufacturing tolerances. The uncertainty of r_m is given by equation (3.4).

To get a good description of the slit width w with respect to the chopper position ε, first we define a relationship between the largest slit width w_b and the length of the slit r_s. This relationship is given by

$$\beta = \left(\frac{w_b - w_t}{2} \cdot \frac{1}{r_s} \right) \qquad (3.7)$$

where the two factors w_b and w_t describe the width at the bottom of the chopper slit and the width at the top of the chopper slit, respectively. As previously, r_s describes the length of the chopper slit. See figure (3.10). We find the uncertainty of this relationship by applying equation (C.2) to equation (3.7):

$$\Delta\left(\beta\right) = \sqrt{\left(\frac{1}{2\cdot r_s}\Delta\left(w_b\right)\right)^2 + \left(\frac{1}{2\cdot r_s}\Delta\left(w_t\right)\right)^2 + \left(-\frac{w_b - w_t}{2\cdot r_s^2}\Delta\left(r_s\right)\right)^2} \qquad (3.8)$$

where $\Delta\left(w_b\right)$, $\Delta\left(w_t\right)$ and $\Delta\left(r_s\right)$ are the uncertainties of the bottom slit width, the top slit width and the length of the slit, respectively. All of these uncertainties are set to $0.025\ mm$ due to fabrication tolerances. Using this relationship, we can calculate the slit width as a function of the chopper position. The width of the slit is given by:

$$w = w_t + 2\left(\beta\cdot r_m\right) \qquad (3.9)$$

Applying equation (3.9) to equation (C.2) we obtain the uncertainty of the slit width:

$$\Delta\left(w\right) = \sqrt{\Delta\left(w_t\right)^2 + \left(2\cdot\beta\cdot\Delta\left(r_m\right)\right)^2 + \left(2\cdot r_m\cdot\Delta\left(\beta\right)\right)^2} \qquad (3.10)$$
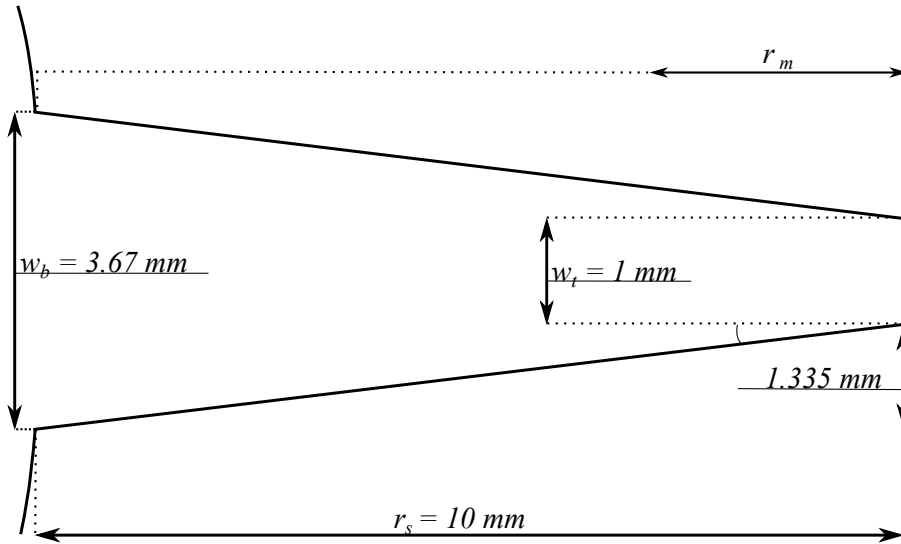
Figure 3.10: *shows the design and dimension of the chopper disc slits.*
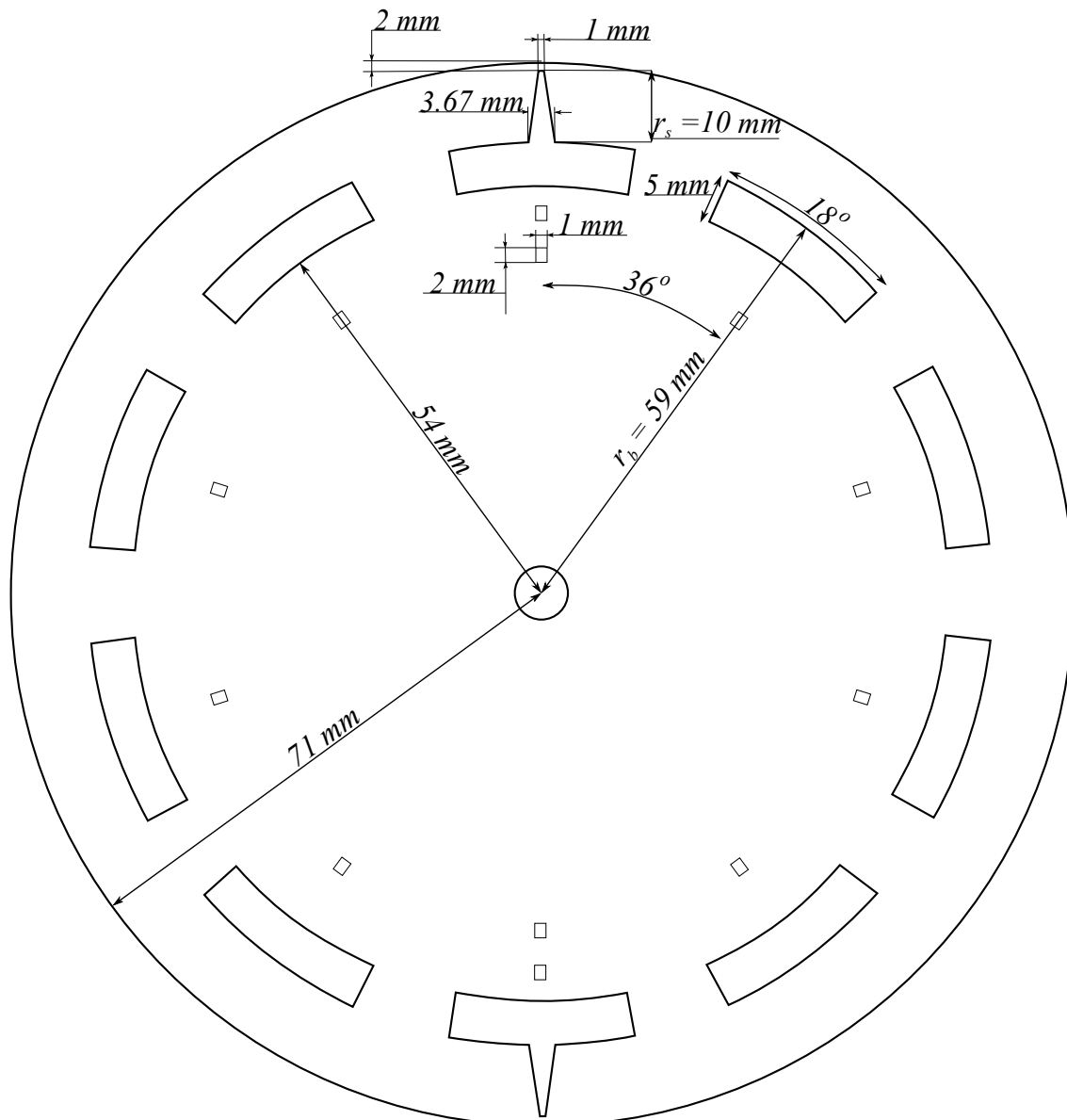
Figure 3.11: *shows the design and the dimensions of the chopper disc. The disc is made from stainless steel and is* 0.15 *mm thick.*

Figure (3.11) also shows two additional sets of 1 *mm* wide slits. The first set comprises two slits located in radial direction from the trapezoidal slits towards the center of the disc. These slits are assigned to deliver a trigger signal to provide the time of flight electronics with a starting pulse for the counting process. The second set located closer to the center of the chopper disc includes 10 slits providing an accurate measurement of the chopper frequency.

3.2.3 Mirror Chamber

The name of this chamber comes from an alternative microscope set-up where silicon mirrors were used to focus the beam. The mirror was mounted in this chamber and thus the chamber was named "mirror chamber" [33]. The benefits of using silicon mirrors to focus the beam is firstly that there is no chromatic aberration and secondly a large numerical

aperture. However, there are difficulties combined with the use of focusing mirrors, such as keeping the silicon mirrors clean over time. It is also difficult controlling the curvature of the mirror. Instead of silicon mirrors, MAGIE now utilizes Fresnel zoneplates as its focusing element. The zoneplates use the principle of diffraction of the helium atoms on a set of free-standing rings, where the outermost diameter of the zoneplate can be between 192 μm - 540 μm. The outermost line spacing of the Fresnel zoneplate rings is approximately 50 nm. A detailed description of the zoneplates can be found in reference [28]. The mirror chamber contains a sample holder where the zoneplates are mounted which can be manipulated in all directions and even tilted to multiple angles. The movements and tilting of the sample holder is used to optimize the zoneplate position. The sample holder is controlled by a stepper motor with a resolution of 400 $steps/mm$. Backlash can occur when moving the sample holder, so to ensure position accuracy we always move past the wanted position and back in either increasing or decreasing direction for all movement.

3.2.4 Piezo Chamber

During imaging, the piezo chamber is where the sample is located. This chamber houses a very high precision piezo table holder, where a piezo table is held. The piezo table contains several slots where samples, or slits, can be placed. The high precision piezo-driven holder can move the sample or slit as far as 80 μm, with a resolution of 0.02 μm in both the X and Y direction in closed loop mode [34]. During the experiments done for the work of this thesis, no sample or slit was mounted in the piezo chamber, since the experiments focus on the investigation of the properties of the neutral helium beam.

3.2.5 Detector Chamber

The final chamber on MAGIE is the detector chamber. The detector unit is an ionization detector where the helium atoms are ionized by electron bombardment. As mentioned in section (3.2.1.2) helium has an ionization potential of 24.5 eV. Electrons are freed by heating up a filament, and accelerated over the beam by an electric potential. As the helium atoms enter the detector they get bombarded by the freed electrons, some of which will end up colliding with the helium atoms and ionize them. The helium ions that are created by the electron bombardment are then selected using a 90° magnetic field selector, and the collected helium ions are focused into a channeltron detector. This channeltron has a high time resolution. The signal is discriminated and picked up as a count rate in a National Instruments Labview Virtual Instrument via a CAMAC bus. Figure (3.12) illustrates the detection system on MAGIE.
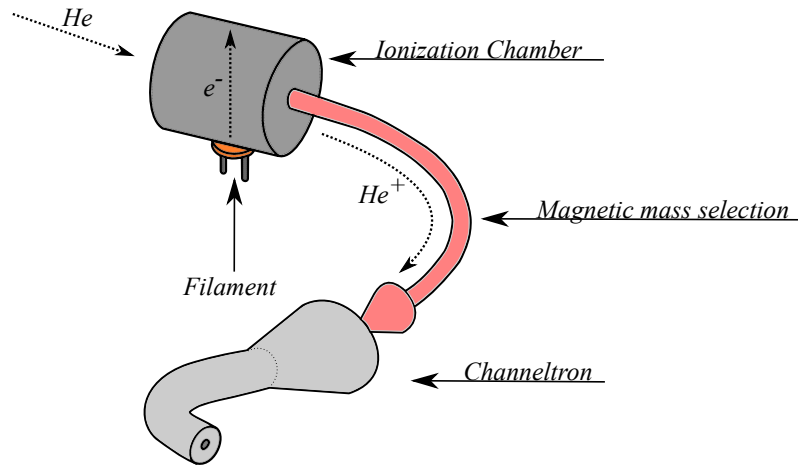
Figure 3.12: *shows the detection system on MAGIE. The helium atoms are ionized by electron bombardment in the ionization chamber. The helium ions are then selected using a magnetic mass selector and finally the ions are counted using a channeltron.*

3.3 MAGIE Vacuum

There are three different types of vacuum pumps: Pre-vacuum pumps (PV), High-vacuum pumps (HV) and ultra-high-vacuum pumps (UVH). In the following sections only the pump types used on MAGIE are described.

3.3.1 Pre vacuum pumps

3.3.1.1 Rotary vane pumps

A rotary vane pump comprises a cylindrical housing in which an eccentrically suspended and slotted rotor turns. The turning rotor has vanes which are usually forced outwards by the centrifugal force, but also by a spring located in between the two vanes. This forces the vanes to be pushed towards the edge of the housing walls at all times. Figure (3.13) shows the working principle of the rotary vane pump. The volume on the side of the intake increases as the vanes rotate with the rotor, letting gas enter from the intake. The volume on the side of the outlet is decreasing. This rotation forces the gas to be ejected out of the oil-sealed exhaust valve. A disadvantage of these pumps is that they are filled with oil, which makes them unsuitable to use where a clean vacuum is of utmost importance. Another disadvantage is the mechanical wear caused by the vanes constantly being in contact with the housing wall. The rotary vane pump is commonly used to provide backing pressure in the range of $10^{-2} - 10^{-3}$ *mbar* for ultra-high vacuum pumps [35]. MAGIE has one rotary vane pump, which is used to provide a backing pressure for the two roots pumps connected to the source chamber.

3.3.1.2 Roots pumps

A roots pump is a rotary positive-displacement type pump where two symmetrically shaped impellers rotate past each other in close proximity inside a casing. Similar to the rotary

vane pump, the gas is trapped in different pockets when it enters the pump from the intake. As the impellers rotate, pockets of gas are trapped and pushed along the casing towards the exhaust where it is ejected. The two rotating impellers have a clearance of a few millimetres between themselves and with the pump casing wall. Since there is no contact between the casing or in between the impellers themselves, the roots pump may be operated at very high speeds without causing mechanical wear on the impellers or pump housing. The roots pump is considered a "dry pump", meaning it does not contain any oil, in comparison to the rotary vane pump. The pressure range of the roots pumps is between $10^1 - 10^{-5}$ $mbar$ [35]. Figure (3.14) illustrates the principle behind the roots pump. MAGIE has two roots pumps pumps which are connected to the source chamber. Standard roots pumps cannot work at atmospheric pressure and require a backing pump. In MAGIE, this is provided by a rotary vane pump connected to the two roots pumps of the source chamber.
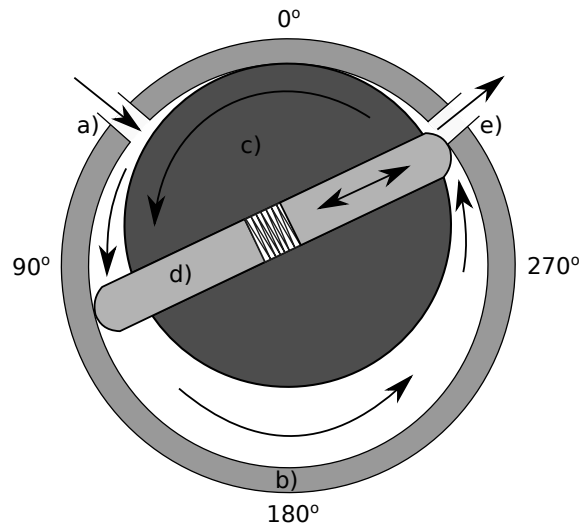
Figure 3.13: *shows the working principle of a rotary vane pump. a) The intake of the pump where the gas enters. b) The cylindrical pump casing. c) The turning rotor inside the pump casing. d) The vanes in the pump that gets pressed outwards towards the casing by a spring in between the two vanes. e) The oil-sealed exhaust valve of the pump*

3.3.1.3 Scroll pumps

A scroll pump uses two interleaved Archimedean spiral-shaped scrolls that pump or compress liquids or gases. One of the scrolls is fixed while the other orbits eccentrically without rotating. This leads to pockets of fluid, or gas, being trapped and compressed between the two scrolls. Another method for producing the compression motion is co-rotating the scrolls in a synchronous motion, but with different centres of rotation. The relative motion is the same as if one scroll was kept stationary while the other was orbiting. The scroll pump operates very smoothly, and does not make a lot of noise, and is known to operate very reliably. Attainable pressures range from atmospheric pressure to 10^{-2} $mbar$ [35]. Figure (3.15) illustrates the principle behind the scroll pump. MAGIE has scroll pumps connected to every chamber except the source chamber
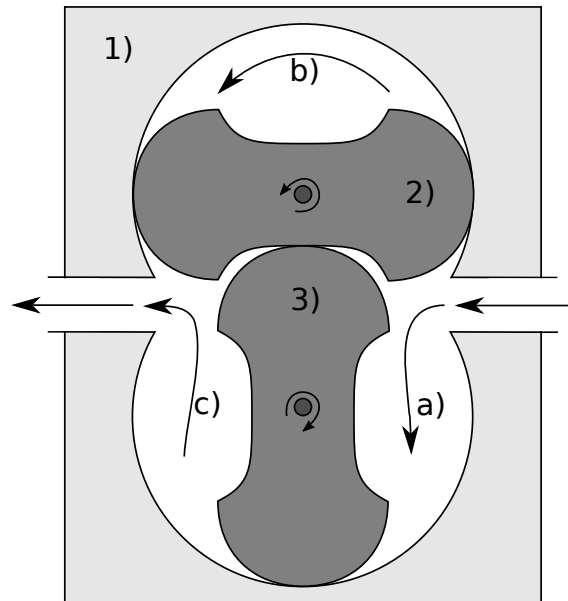
Figure 3.14: *shows the working principle of a roots pump. As the two impellers rotate in their respective directions, pockets of gas are pushed towards the exhaust. 1) Roots pump casing. 2) Impeller rotating counter clock-wise. 3) Impeller rotating clock-wise. a) Pocket of gas pushed by clock-wise rotating impeller. b) Pocket of gas pushed by counter clock-wise impeller. c) Pump exhaust where pockets a) and b) are pushed out.*
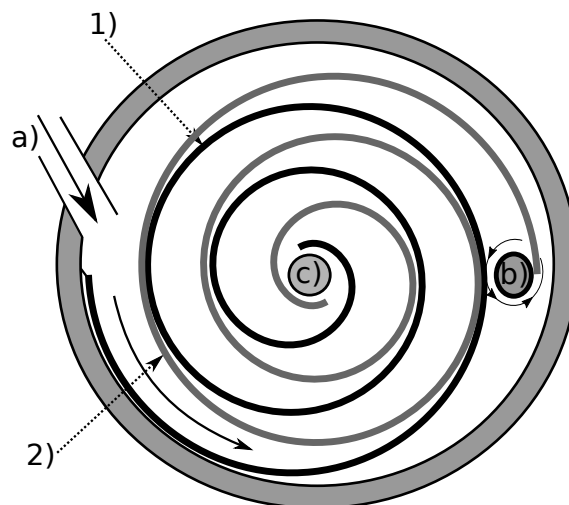
Figure 3.15: *shows the working principle of a scroll pump. As the inner spiral (black) twirls inside the outer spiral (grey), gas is trapped and pushed towards the pump exhaust. 1) Static spiral. 2) Twirling spiral. a) Pump intake. b) Turning point of twirling spiral. c) Pump exhaust*

3.3.2 Ultra-High vacuum pumps

3.3.2.1 Turbo molecular pump

As gas enters the turbo molecular pump, the gas particles receive an impulse in the direction of the exhaust. This happens when they are impacted by the rapidly moving surface of a rotor. Gas particles being hit by the first rotor are pushed towards the next section, which is a stator. A stator is basically a rotor where the vanes of the stator are normal to the vanes of the rotor (See figure (3.16)). The molecules then encounter the next rotor, which again pumps the gas further down. Through a succession of rotors and stators, the gas particles are pushed in the direction of the exhaust where they are finally ejected. The space between the rotors and stators is in the order of millimetres. For the turbo molecular pump to function, it requires molecular flow conditions, hence a backing pump is required. Vacuum pressures of 10^{-11} $mbar$ can be achieved [35]. All chambers on MAGIE have a turbo molecular pump to create an ultra-high vacuum.
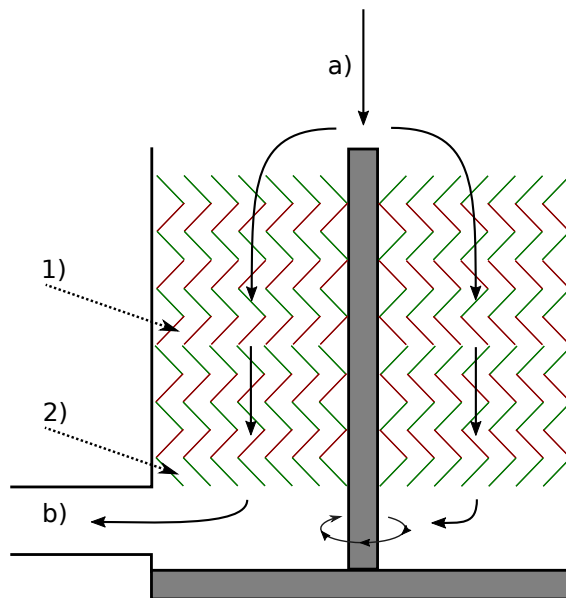
Figure 3.16: *shows the working principle of a turbo molecular pump. As the spinning rotor blades hit molecules, a momentum is given to the molecules which propels them downward. They then hit the stator and are sent further down the chain of rotors and stators, until the molecules are finally ejected through the exhaust of the pump. 1) Rotor. 2) Stator. a) Molecules enter the pump. b) Molecules are ejected through the pump exhaust.*

3.3.3 Pre vacuum pressure measurement gauges

3.3.3.1 Pirani gauges

The Pirani gauge utilizes thermal conductivity to measure the pressures in vacuum systems. A filament is exposed to the gas whose pressure is going to be measured. This filament is heated by an electric current flowing through it. The extent of heat conducted from the filament to its surroundings depends on the gas pressure around the filament. Therefore, pressure controls the thermal equilibrium of the filament. The electrical resistance of the

heated filament depends on its temperature, thus making the pressure of the chamber related to the resistance of the heated filament. The filament is connected to an electrical circuit (Wheatstone bridge) from which, after calibration, a pressure reading may be taken. The Pirani gauge can measure pressures in a range of $10^3 - 10^{-4}$ $mbar$ [36] [35]. MAGIE has Pirani gauges in all chambers.

3.3.4 Ultra-high vacuum pressure measurement gauges

3.3.4.1 Bayart-Alpert gauge

The Bayart-Alpert Gauge (BAG) (or hot filament ionization gauge) has a hot filament that emits electrons and accelerates them towards a cylindrical cathode cage. As the electrons traverse the space enclosed by the grid, which is fully open to the vacuum chamber, the electrons can collide with the gas molecules, causing them to ionize. A wire is located at the center of the ionization volume. This wire collects the resulting ions, and produces a current that is proportional to the pressure at the gauge. If the temperature is held constant, the relationship between the current and the pressure in the chamber is linear. This linear dependence is one of the largest advantages over the Penning gauge. The BAG is also considered to be more accurate, stable and reproducible than its cold filament counterpart. The useful operating range of a conventional BAG extends between 10^{-3} and 10^{-10} $mbar$. Most of the problems for the BAG occurs at $\sim 10^{-10}$ $mbar$, where the X-ray limit, electron stimulated desorption and out-gassing set a limit to the usefulness of the gauge. To minimize the effects of the electron stimulated desorption and out-gassing, the gauge can be degassed and baked. In the absence of degassing and bake-out, the accuracy may be seriously compromised. The Bayart-Alpert's operating life is determined by the lifetime of the filament, which can vary. This is a big disadvantage for hot cathode gauges, and one of the reasons one might choose to use cold cathode gauges instead. That being said, the lifetime of the filaments may be many thousands of hours, making filament lifetime a low importance consideration in most cases [37]. MAGIE has Bayart-Alpert gauges connected to pumping stage 2 and the detector chamber.

3.3.4.2 Penning gauges

Unlike the Bayart-Alpert gauge (see section (3.3.4.1)), the penning gauge (or the Cold Cathode ionization Gauge (CCG)) does not have a filament. The outer cylinder of the gauge works as a cathode. The reason it is described as a cold cathode is due to the fact that the cathode is at an ambient temperature. A wire loop is mounted in the cylinder center, or tube center, and is connected to an electrical feed-through. The wire works as the anode of the penning gauge. A potential is applied to the anode, about $3 - 4$ kV, which causes electrons to travel from the cathode to the anode via field emission. The electrons ionize gases inside the vacuum chamber, and the charged products are collected as a current. The pressure in the chamber is proportional to the collected current and the species of gas present. Outside the gauge tube, a magnet is mounted to increase the travel length of the electrons, thus amplifying their effectiveness. The penning gauge has

a tendency of getting dirty, due to the ionization collected at either the cathode or the anode, and have to be cleaned periodically to function properly. The measurement range of the Penning gauge ranges from $10^{-2} - 10^{-9}$ *mbar* [37]. MAGIE has Penning gauges in all chambers except for the detector chamber and pumping stage 2.

METHOD

This chapter describes the three type of measurements that have been conducted in this thesis. The method of analysing the virtual source scans is shown, and the theory behind the time of flight is explained. The method for analysing the time of flight measurements are shown and finally the center line intensity measurements are described.

4.1 Virtual source scan

The reason for performing the virtual source scans is to obtain information about the size of the virtual source and therefore the beam expansion. The virtual source was described in section (2.2.2) and is illustrated in figure (2.3). The beam intensity is measured as the nozzle is scanned across the skimmer in two dimensions, namely the U and V direction, as shown in figure (4.1). The recorded intensity spectrum, shown in figure (4.2), contains the information about the size of the virtual source. This information can be extracted as explained below.
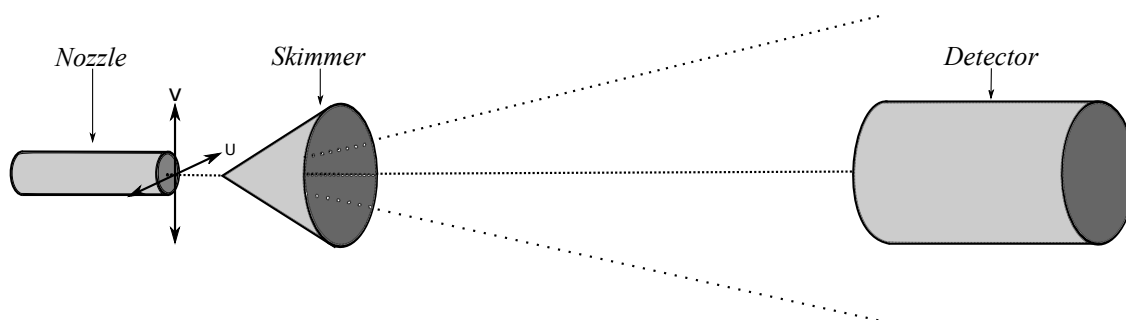
Figure 4.1: *shows an illustration of how the virtual source scans are taken. As helium is ejected through the nozzle pinhole, the whole nozzle is scanned across the skimmer. This scan is done in two dimensions, indicated as U and V.*
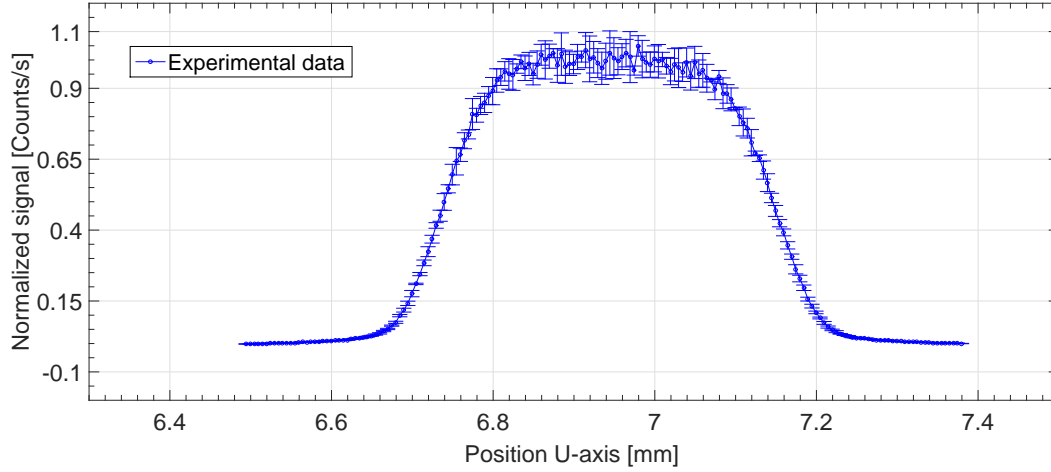
Figure 4.2: *shows a typical virtual source scan conducted with a beam temperature of* 125 K, *a pressure of* 60 bar *and a* 390 μm *skimmer. The source-nozzle position was set to sn* = −6.

4.1.1 Convolution

We assume that the spatial distribution of the virtual source is Gaussian shaped [22] (see figure (2.3)). The Gaussian distribution is given by the equation below [38]:

$$g\left(x\right) = \frac{1}{\sigma \cdot \sqrt{2\pi}} \cdot e^{-\frac{(x-\mu)^2}{2 \cdot \sigma^2}} \tag{4.1}$$

where σ is the standard deviation and μ is the mean value of the distribution. To simplify the calculations the circular skimmer is modelled in each scan direction as a slit opening. The slit opening can be modelled as:

$$s\left(x; a, b\right) = \begin{cases} 0 & x \leq a \\ 1 & a \leq x \leq b \\ 0 & b \leq x \end{cases} \tag{4.2}$$

where $b - a$ is the skimmer diameter. A similar expression is used in the other scan direction. We can do a convolution of the two functions $g\left(x\right)$ and $s\left(x\right)$ and tune the parameters of the Gaussian distribution so that the convoluted product fits the measured virtual source scan spectrum. Equation (4.3) below shows the equation for the convolution:

$$f\left(x\right)_{convolution} = \sum_x g\left(x\right) \cdot s\left(x\right) \tag{4.3}$$

When the convoluted product of functions $g\left(x\right)$ and $s\left(x\right)$ fits the measurement data, the standard deviation of the Gaussian distribution can be extracted and used to calculate the full width at half maximum of the Gaussian. This is found by using equation (2.16), and this is the virtual source size.

Figures (4.3) and (4.4) shows a two-dimensional virtual source scan, the first figure being scanned over the U-axis, and the second figure the V-axis. For all measurements performed

here the calculated virtual source sizes in each direction overlapped each other within the margins of error as expected. An average of the two source sizes has been used when presenting the results obtained for this thesis. All the virtual source scan results found during this thesis have been obtained using this convolution method.
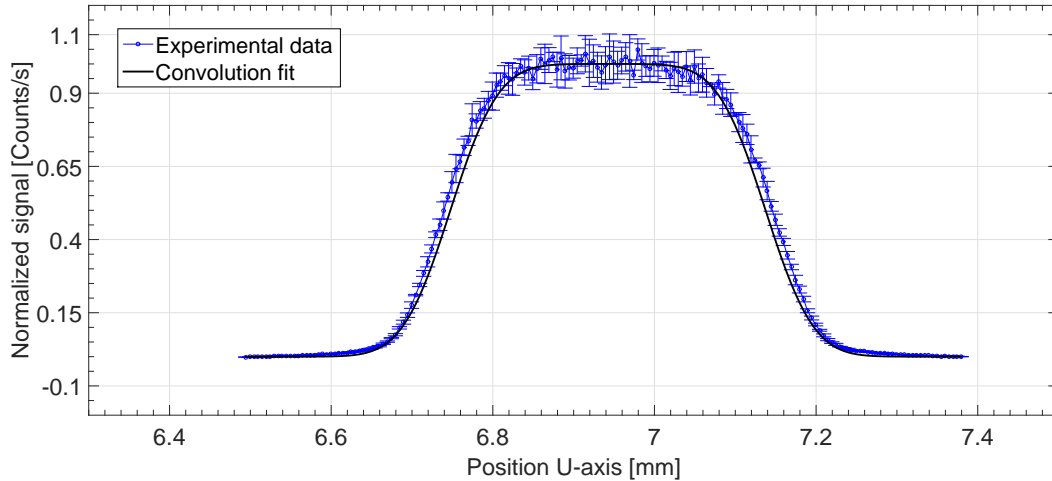
Figure 4.3: *shows the intensity spectrum of file AXIS1_0924. This scan was conducted with a beam temperature of 125 K, a pressure of 60 bar and a 390 μm skimmer. The source-nozzle position was set to sn = −6. The calculated full width at half maximum is: 110 ± 4 μm*
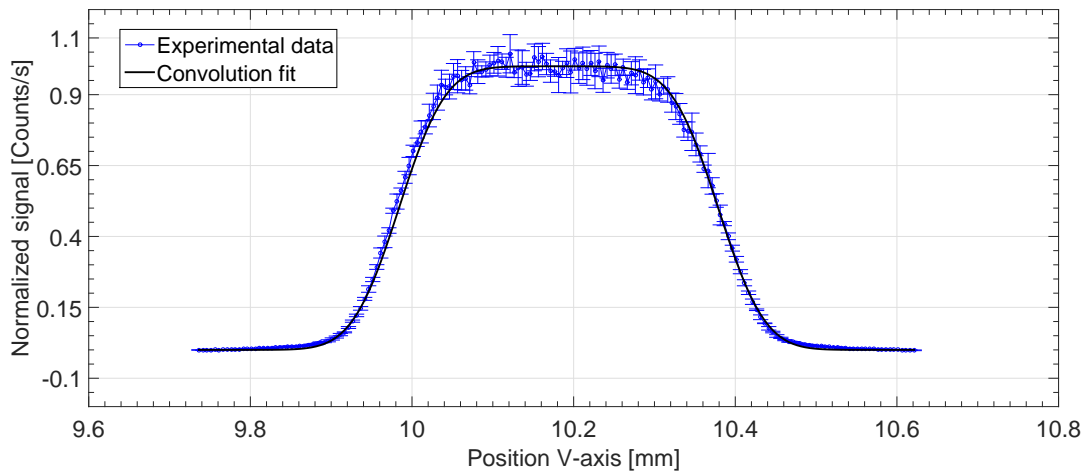
Figure 4.4: *shows the intensity spectrum of file AXIS2_0865. This scan was conducted with a beam temperature of 125 K, a pressure of 60 bar and a 390 μm skimmer. The source-nozzle position was set to sn = −6. The calculated full width at half maximum is: 107 ± 5 μm*

4.2 Time of flight

Time of flight measurements were used to obtain information about the terminal velocity (see section (2.2.4)) and the velocity distribution of the beam. The time of flight measurement is a time distribution due to particles having different velocities arriving at the detector at different times. If the distance that the particles travel (L) is known, and the time of flight (t_f) it takes for the particle to travel a distance of L is measured, the terminal velocity of the particles can be calculated as [39]:

$$v_t = \frac{L}{t_f} \tag{4.4}$$

A measure of the velocity distribution can be found by calculating the speedratio (see chapter (2.2.5)). The speedratio is a measure of the monochromaticity of the beam, and is related to the terminal velocity v_t, and the width of the velocity distribution Δv_t. The recorded time of flight spectrum can be fitted with a Gaussian distribution [40] where the mean value, in our case the peak time t_p, and the standard deviation $\sigma(t)$ can be extracted. Figure (4.5) illustrates the time of flight measurement principle from the moment the chopper disc cuts the beam to the moment the signal has been detected by the detector. Figure (4.6) shows a time of flight measurement, and figures (4.8) and (4.9) show time of flight measurements fitted with Gaussian distributions. As mentioned in section (2.2.5) the standard deviation of the Gaussian distribution is related to the full width at half maximum. The full width at half maximum is given by equation (2.16):

$$\Delta t = 2 \cdot \sqrt{2 \cdot ln(2)} \cdot \sigma(t) \quad \longrightarrow \quad \Delta v_t = 2 \cdot \sqrt{2 \cdot ln(2)} \cdot \sigma(v) \tag{2.16}$$

where $\sigma(t)$ is the standard deviation of the Gaussian fitted to the time of flight measurement data. The full width at half maximum of the recorded time of flight spectrum is then used to calculate the speedratio given by equation (2.17):

$$S = 2 \cdot \sqrt{ln(2)} \cdot \frac{t_f}{\Delta t} \; = \; 2 \cdot \sqrt{ln(2)} \cdot \frac{v_t}{\Delta v_t} \tag{2.17}$$

where t_f is the time of flight of the neutral helium atoms and Δt is the full width at half maximum of the time of flight spectrum.

4.2.1 Time of flight module

The time of flight measurements are done by measuring the flight time of a beam package travelling a distance L from the chopper disc to the detector. As the helium beam travels along the beam path from chamber to chamber, it eventually arrives in the chopper chamber. In this chamber, there is a chopper disc with two small slits (the chopper disc and the chopper slits are explained in section (3.2.2.1)). The chopper disc is rotating with a set frequency f_{ch}. The two slits in the chopper disc chop the beam into small packages that continue along the beam path towards the detector. Each time one of the slits pass
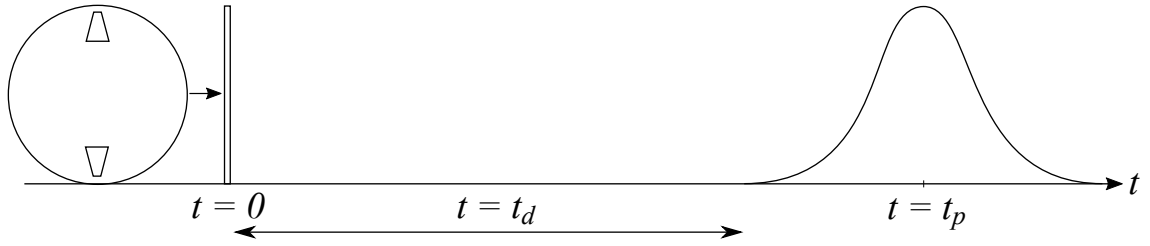
Figure 4.5: *shows an illustration of a beam package as it travels in time from the chopper disc to the detector. From the moment the beam is chopped, the pulse starts at time $t = 0$. The pulse travels along the beam path, and after waiting the set delay time t_d, the detection of the pulse starts. The center position of the detected pulse signal is the peak time t_p.*

the beam, a LED light sends a pulse triggering the measuring electronics. Four different parameters are important for the time of flight:

1: The first parameter is the channel width t_{ch} of the recorded signal. The beam package is detected over 400 channels, N_{ch}, where the channel width of each channel can be set to choose the specific resolution for the time of flight measurement. The channel width is pre-set in the time of flight measurement software.

2: The second parameter is the delay time t_d so that the electronics does not start to count until a short interval before the atoms arrive at the detector. At a beam temperature of $125\ K$, the atoms travel slower than at $300\ K$, and thus a longer delay time is required. The frequency of the chopper disc is set so that the measuring time is as short as possible, and only one trigger is used. Due to the different beam velocities at warm and cold beam temperature, the beam package is detected at different times. To ensure the beam packages for the two beam temperatures are measured in the time of flight window the delay time has to be adjusted respectively. So the chopper frequency has to be adjusted ($230\ Hz$ for cold beam, and $310\ Hz$ for warm beam).

3: The third parameter is the peak time t_p of the recorded time of flight spectrum, which is defined as the center position of the measured Gaussian distribution given by the time of flight measurement. The peak time also corresponds to the mean velocity of the beam particles.

4: The fourth parameter is called the correction time t_c, and will be explained in the next section.

To have a complete equation for the flight time, the delay time, the correction time and the channel width must also be taken into account. Table (4.1) below shows the settings used for the time of flight measurements conducted in this thesis.

Settings	Symbol	Value	Unit
Chopper-Detector distance	L	1981	m
Delay time	t_d	0.7	s
Number of channels	N_{ch}	400	
Channel width	t_{ch}	$0.8 - 2.5$	$\mu s/channel$
Chopper frequency	f_{ch}	$230 - 310$	Hz
Chopper position	ε	$0.66 - 1.005$	$Inches$
Chopper radius at beam center	r_{ch}	$60.24 - 69$	mm
Chopper slit width at beam center	w	$1 - 3.34$	mm

Table 4.1: *shows the settings used for the time of flight measurements conducted in this thesis.*
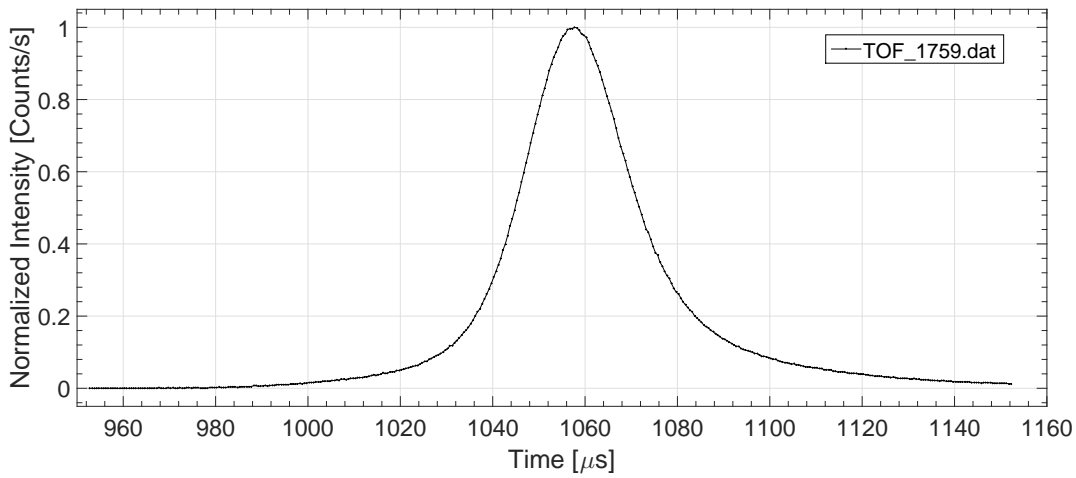
Figure 4.6: *shows the measured time of flight spectrum for file* $TOF\_1759.dat$ *for the* 390 μm *skimmer at room temperature* $(300$ $K)$. *The chopper position is set to* $\varepsilon = 0.95$ *inches and the source-nozzle position is set to* $sn = +6$ mm *(Distance between nozzle and skimmer is* 17.6 $mm)$.

4.2.1.1   Time of flight corrections

The correction time t_c is built up by three different contributing factors [14]:

$$t_c = t_1 + t_2 + t_3$$

t_1: The trigger signal delivered by the LED every time the slits on the chopper disc passes the beam will be given too early due to the diode set-up in connection to the rectangular shaped trigger slits. The early signal from the LED leads to $t_1 < 0$.

t_2: A potential misalignment between the trigger slits on the chopper disc and the photo diode giving off the LED pulse signal, creating an offset. Depending on the rotational direction of the disc, this offset may be positive or negative.

t_3: By having a nearly infinite small straight line we could have a perfect slit opening, however, this is not reasonable, and we are left with having a finite slit width. This

causes a negative offset to the time, which cannot be positive, as it does not depend on the rotational direction of the chopper disc [14].

We can determine the correction time t_c experimentally, as it depends on the frequency and the rotational direction of the chopper disc. This is done by performing a succession of time of flight measurements, changing the rotating frequency of the chopper disc for each measurement. The peak time t_p from the time of flight scans can be plotted against the inverse chopper frequency, and a linearly increasing curve is found. The gradient of the linear curve, α, is related to the correction time as stated by equation (4.5).

$$t_c = \frac{\alpha}{f_{ch}} \tag{4.5}$$

In figure (4.7) the linear regression for two different sets of measured peak times and frequencies are shown for the 390 μm skimmer, one set at chopper position $\varepsilon = 0.66$ *inches* and one set at chopper position $\varepsilon = 0.98$ *inches*. The measured alpha value used for all the 390 μm skimmer time of flight measurements is $\alpha_{390} = 9000 \pm 500$ $\mu s Hz$. An alpha value of $\alpha_4 = 10000 \pm 500$ $\mu s Hz$ was measured for the 4 μm skimmer.

The time of flight measurements are conducted at two different temperatures: cold beam temperatures of 125 K and warm beam temperatures of 300 K. The cold beam temperature of 125 K is achieved by cooling the beam using liquid nitrogen. Depending on the beam temperature, two different chopper frequencies are used for the time of flight measurements. A chopper frequency of $f_{ch} = 230$ Hz for cold beam measurements and a chopper frequency of $f_{ch} = 310$ Hz warm beam measurements. Using equation (4.5) we can calculate the correction time at the different temperatures. The correction time t_c for the 390 μm skimmer at cold beam temperatures can be calculated to be $t_c^{cold} = 39.8$ μs, and the correction time for the warm beam temperatures can be calculated to be $t_c^{warm} = 29.5$ μs.
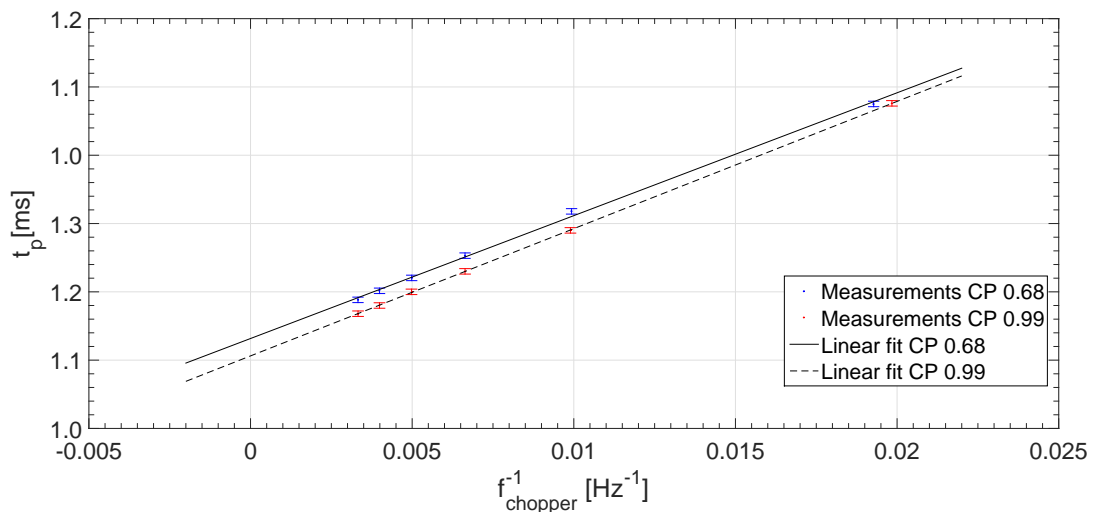
Figure 4.7: *shows the measured peak time t_p as a function of the inverse frequency f_{ch}^{-1} and the linear regressions of the two curves for the 390 μm skimmer time of flight measurements at chopper positions $\varepsilon = 0.68$ inches and $\varepsilon = 0.99$ inches. Both measurement sets were conducted at 300 K.*

The last correction to be made comes from the channel width t_{ch}. Because the channel time is associated with ending time, the entire measurement is shifted in time. To compensate for this shift, we subtract half of the channel width so that we are in the middle of the channels interval instead of at the end [41].

Taking all of the parameters into account, the time of flight (t_f) can be defined as:

$$t_f = t_p + t_d - t_c - \frac{t_{ch}}{2} \tag{4.6}$$

4.2.2   Standard deconvolution

As mentioned in section (4.2), the measured time of flight spectrum is fitted with a Gaussian model, so that the peak time t_p and the full width at half maximum, Δt, can be determined. This Δt is not the actual value of the beams flight time distribution, but is in fact built up by a convolution of three distributions. The three contributions are:

Δt_{actual} : The actual velocity (speed) distribution of the beam.

Δt_C : The slits have finite widths. The contribution of the finite slit width to the width of the measured time of flight spectrum can be estimated as:

$$\Delta t_C = \frac{w}{2\pi \cdot r_{ch} \cdot f_{ch}} \tag{4.7}$$

where w is the width of the slit at the beam position, r_{ch} is the radius of the chopper disc from the center of the disc to the position of the beam and f_{ch} is frequency of the chopper disc.

Δt_D : The filament used to ionize the helium atoms has a certain length. This means that atoms can ionize at different positions instead of all being ionized at one point. The ionization length has been approximated to be $X_D = 4.6\ cm$ [31]. The time contribution caused by this depends on the terminal velocity of the beam, and can be estimated by:

$$\Delta t_D = \frac{X_D}{v_t} \tag{4.8}$$

where X_D is the ionization length and v_t is the terminal velocity of the beam.

These three contributions comprises our measurement spectrum. One common interpretation of the time of flight measurement results is to approximate all of the three previously mentioned contributions by Gaussian functions [40], so that their full width at half maximums can be added together quadratically, as shown in equation (4.9):

$$\Delta t^2 = \Delta t_{actual}^2 + \Delta t_C^2 + \Delta t_D^2 \tag{4.9}$$

Equation (4.9) can be rearranged, so that we get an expression for the actual full width at half maximum for our signal:

$$\Delta t_{actual} = \sqrt{\Delta t^2 - \Delta t_C^2 - \Delta t_D^2} \tag{4.10}$$
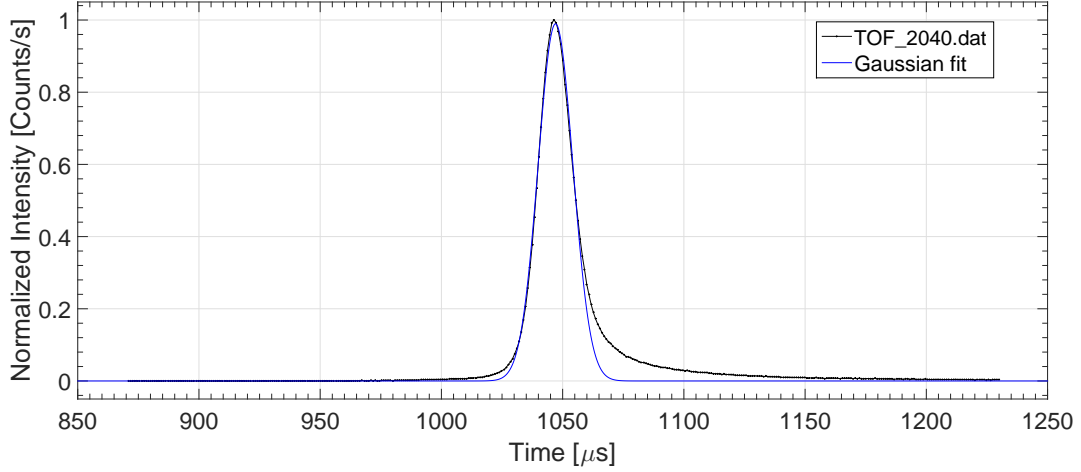
Figure 4.8: *shows the measurement file $TOF\_2040.dat$. This is for the $390\ \mu m$ skimmer, at $158bar$, chopper position $\varepsilon = 0.99$ inches and a source-nozzle position of $sn = +6\ mm$ (Total distance $17.6\ mm$). The bad fit to the right is most likely related to background collisions. The used settings was a chopper frequency of $f_{ch} = 310\ Hz$, a distance $L = 1.905\ m$, delay time of $t_d = 591\ \mu s$ and a channel width of $t_{ch} = 0.9\ \mu s$. The terminal velocity has been measured to $v_t = 1819 \pm 6\ m/s$, and the speedratio to $S = 103 \pm 5$. Using the standard deconvolution method (see section (4.2.2)) the corrected speedratio becomes $S_{corr} = 119 \pm 7$.*
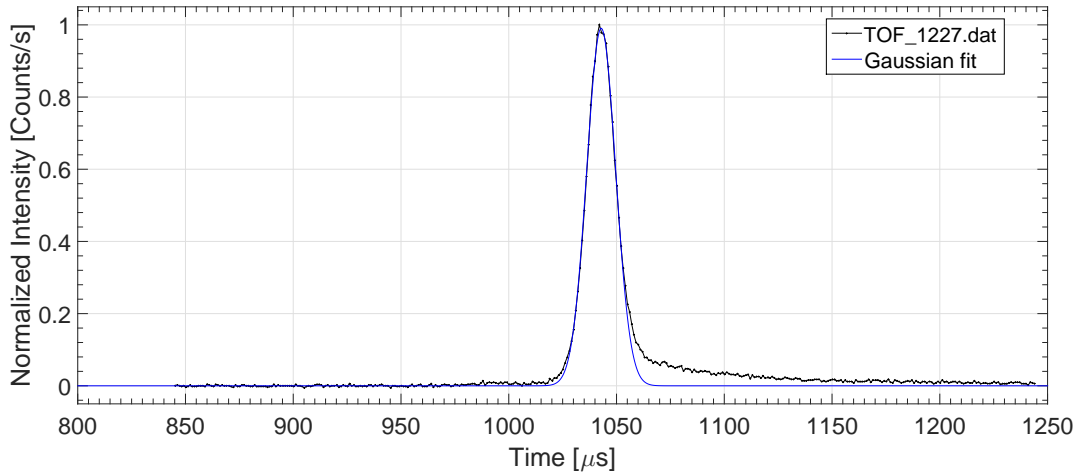
Figure 4.9: *shows the measurement file $TOF\_1227.dat$. This is for the $4\ \mu m$ skimmer, at $160\ bar$, chopper position $\varepsilon = 0.99$ inches and a source-nozzle position of $sn = 6\ mm$ (Total distance $17.6\ mm$). The bad fit to the right is most likely related to background collisions. The used settings was a chopper frequency of $f_{ch} = 310\ Hz$, a distance $L = 1.905\ m$, delay time of $t_d = 875\ \mu s$ and a channel width of $t_{ch} = 1.0\ \mu s$. The terminal velocity has been measured to $v_t = 1827 \pm 6\ m/s$, and the speedratio as $S = 110 \pm 3$. Using the standard deconvolution method (see section (4.2.2)) the corrected speedratio becomes $S_{corr} = 130 \pm 5$.*

4.2.3 Linear approximation

At high speedratios, when there is a small velocity distribution, the standard deconvolution procedure becomes unreliable. For the high speedratios the full width at half maximum of the beams velocity distribution is small compared to that of the chopper transmission function. This means that a slight error in the determination of the slit width can lead to large changes in the calculated speedratio. At a beam temperature of $T = 125\ K$ and a pressure of $80\ bar$ a slit width variation of $\Delta w = 0.1\ mm$ leads to a deviation in the calculated speedratio of approximately $\Delta S = \pm 40$ [14]. The variation in the slit width is due to three factors:

- As shown in section (3.2.2.1), the slits on the MAGIE chopper disc has a trapezoidal shape meaning that the width of the slit w will change depending on the height position of the chopper disc ε with respect to the beam line. The beam position may vary slightly and hence the slit width is not constant.

- The vertical translation stage used to position the skimmer (when changing source-nozzle position) has a high inaccuracy especially when it comes to repeatability [14].

- Although small, the manufacturing tolerances of the chopper slit also have an influence on the exact slit width

To avoid the influence of the chopper slit function, a new evaluation method for the speedratio was developed by Eder et al. [14][42]. A number of time of flight measurements are conducted in succession at different height positions (chopper position ε) of the trapezoidal slit. The determined speedratio of each time of flight measurement is plotted against the chopper height position the measurement was conducted at. A linear curve can then be extrapolated to an infinitely small slit width ($w = 0$) and the speedratio of this point determined. Having a slit width of 0, the chopper slit's transmission function will no longer broaden the beams real flight time distribution, and hence no longer influence the speedratio.

The intensity at every chopper height position is also recorded. The intensity is recorded at decreasing slit widths until there is no more beam signal. At this point, the beam has passed the edge of the slit at its smallest width ($w = 1$). An illustration of the chopper slit is shown in figure (4.10).
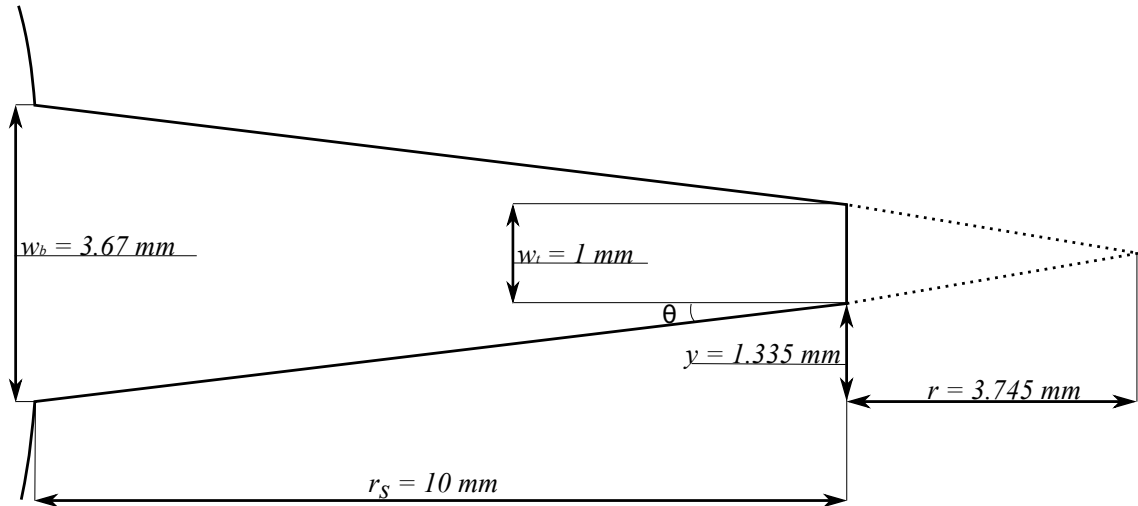
Figure 4.10: *shows an illustration of the trapezoidal chopper slit and the extrapolation to an infinitely small slit width. Using the dimensions of the slit, it can be calculated that the perfect slit would be 3.745 mm longer than the current trapezoidal slits.*

Figure (4.11) shows the measured intensity at the corresponding chopper position ε. As the beam touches the edge and begins to move out of the slit, the intensity will start to drop more rapidly than before (seen as the steeper curve slope in the figure). The measured intensities make it possible to determine the height position of the chopper when the beam position is at the edge of the slit. Assuming the intensity loss before the steep slope and at the steep slope is linear, the exact edge of the slit can be found by fitting these two areas with linear functions. The intersection between the linear curves is the height position of the chopper at the edge of the slit. The two linear curves and the intersection can be seen in figure (4.11). The equation for a linear function is given by [43]:

$$y = a \cdot x + b \tag{4.11}$$

where a is the gradient and b is the intersection with the y-axis. Having two linear functions, the coordinate on the x-axis of the intersection point between the two functions can be found by the equation below:

$$a_1 \cdot x + b_1 = a_2 \cdot x + b_2$$
$$x(a_1 - a_2) = b_2 - b_1$$
$$x = \frac{b_2 - b_1}{a_1 - a_2}$$
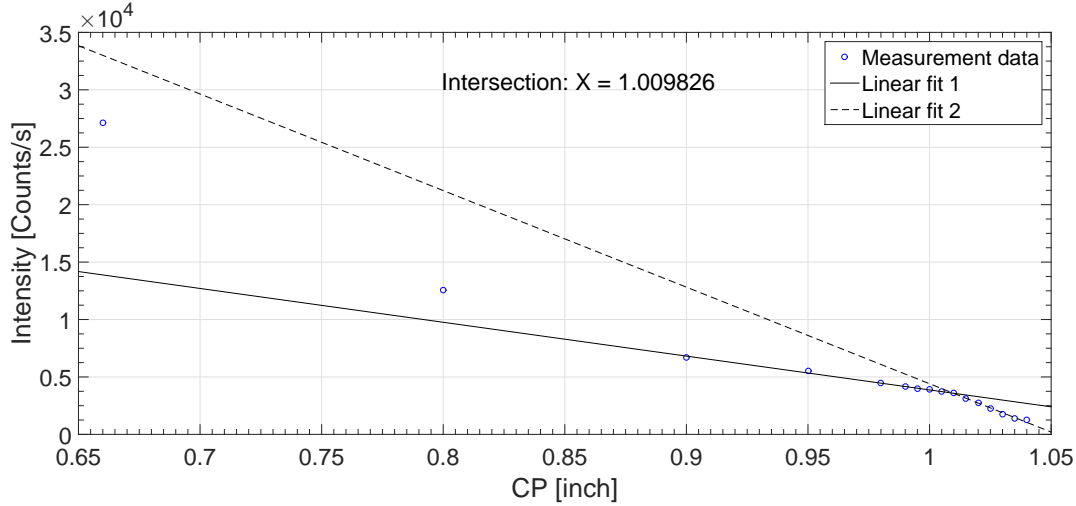
Figure 4.11: *shows a 4 μm skimmer intensity measurement series from files SCAN_00862 and SCAN_00863. The scan was conducted at a beam temperature of 300 K, with a pressure of 120 bar and at source-nozzle position sn = −6. Two linear fits have been fitted, one before the larger slope, and one at the larger slope. The intersection point of the two linear fits have been calculated to a height position of 1.009 inches.*

Knowing the chopper position of the slit's edge, the chopper position of the ideal slit can be found. This is done by linearly extrapolating the trapezoidal slit the point of an infinitely small slit width, $w = 0$. The illustration shown by figure (4.10), shows the extrapolation of the trapezoidal chopper slit to the point of an infinitely small slit width. The extended length of the ideal slit can be obtained by the use of trigonometric functions. The angle between the sides of the chopper slit is found by:

$$Tan\ \theta = \frac{y}{r_s}$$
$$\theta = Tan^{-1}\left(\frac{y}{r_s}\right)$$

where r_s and y are the length of the sides of the trapezoidal slit. Having the angle θ, the additional length can be calculated:

$$Tan\ \theta = \frac{0.5}{r}$$
$$r = \frac{0.5}{Tan\ \theta}$$

Using the equations above, the additional length is $r = 3.745\ mm$, which equals $\sim 0.14745\ inches$. By adding r to the chopper position at the edge of the trapezoidal slit, the chopper position of an infinitely small slit width is found:

$$\varepsilon_{w=0} = \varepsilon_{edge} + r \tag{4.12}$$

As mentioned earlier, a linear curve can now be fitted to the experimentally measured speedratio values. The speedratio value of the linear curve at the chopper position of the infinitely small slit width can then be found. Figure (4.12) shows a series of time of flight measurements and their measured speedratio values plotted against chopper position. A linear curve is fit to the data points and the speedratio at $\varepsilon_{w=0}$ is found.
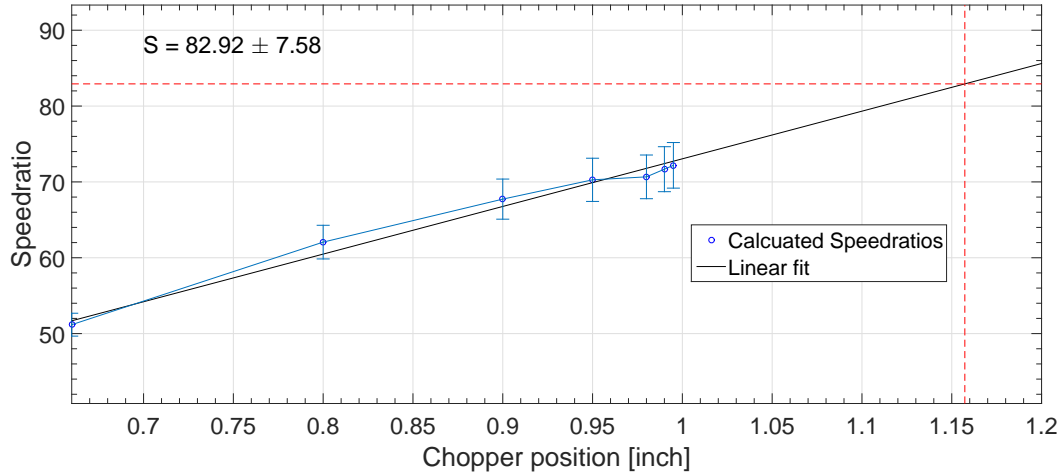
Figure 4.12: *Figure shows linear extrapolation of the speedratios from file SCAN _ 00862. A linear function has been fitted to the speedratios and the intersection of the linear function and the chopper height of the ideal slit edge is shown.*

All time of flight measurement results presented in this thesis have been obtained using this linear extrapolation method.

4.2.4   Non-linear approximation

A new non-linear approximation of the speedratio is under development. This follows the same method of taking a series of time of flight and intensity measurements at different chopper height positions. Instead of linearly extrapolating the speedratio up to the point where there is an infinitely small slit width, a non-linear model is applied. The non-linear extrapolation can be done either analytically or numerically, and these methods have so far showed significant reduction in the speedratio uncertainty in comparison to both the standard deconvolution method and the linear approximation [42].

4.3   Center line intensity

It is important to know how the center line intensity behaves depending on the different skimmer sizes and shapes. The theoretical center line intensity follows the equations described in section (2.2.3).

The center line intensity measurements are done with two apertures obstructing the beam path. One aperture is a 400 μm pinhole aperture positioned after the skimmer. This aperture reduces the excess of helium atoms arriving at the detector, effectively reducing the background intensity. After the 400 μm aperture, and before the detector, a second aperture is placed. This aperture can be selected to be either a 50 μm pinhole aperture or a 200 μm pinhole aperture, depending on the desired size of the beam. For all center line intensity measurements conducted in this thesis, the 50 μm pinhole aperture has been used. This pinhole aperture selects the center of the beam and the atoms going through is measured as the center line intensity in the detector. Figure (4.13) shows illustrates the principle of the center line intensity measurements.
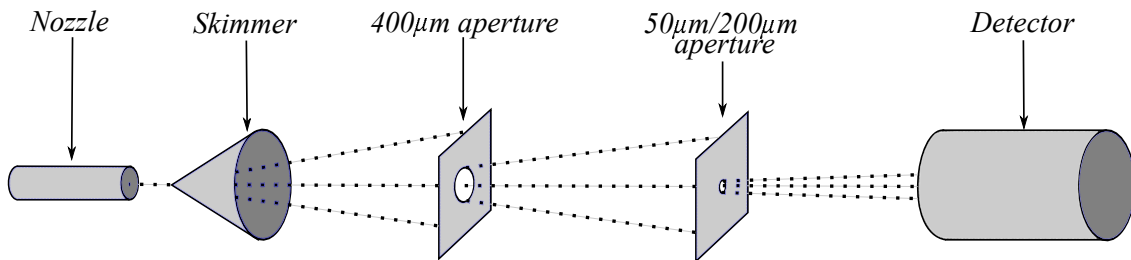
Figure 4.13: *shows an illustration of how the center line intensity measurements are taken. As helium travels along the beam path, two apertures are placed in the beam path. The first aperture, the 400 μm aperture, is located behind the skimmer. This is here to reduce the amount of background in the detector. The second aperture is a 50 or a 200 μm aperture, and this is located in front of the detector. This aperture selects the center of the beam such that only the central part of the beam hits the detector.*

Theoretically the center line intensities should be the same regardless of the skimmer used (see section (2.2.3)). Figure (4.14) shows the measured center line intensity at a cold beam temperature for the 390 μm skimmer at source-nozzle position $sn = +6$. The theoretical center line intensity is also shown, calculated using a detector efficiency of $2.1 \cdot 10^{-6}$ due to the 4 A emission current used by the ionization detector [44]. The center line intensity measurements for this thesis have been conducted with six different skimmer orifice diameters, and three different skimmer types (see chapter (3.2.1.1)).
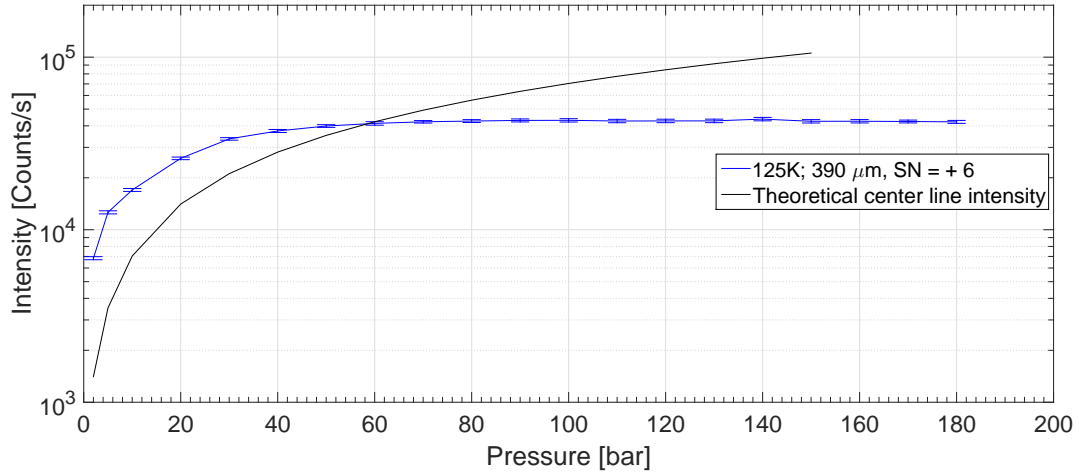
Figure 4.14: *shows the measured center line intensity for the 390 μm skimmer at a beam temperature of 125 K. The source-nozzle position is set to sn = +6. The figure also shows the theoretical center line intensity using a detector efficiency of* $2.1 \cdot 10^{-6}$ *[44].*

RESULTS AND DISCUSSION

This chapter presents the results from the virtual source measurements, center line intensity measurements and time of flight measurements. The results from the different measurements are compared and discussed up against theory and, where possible, other measurements published in the literature.

The aim of these experiments is to test the properties of the molecular beam produced with microskimmers, in particular how the properties of these beams deviate from beams created with larger skimmers. In order to get the most detailed information the experiments have been designed to test as large an experimental parameter range as possible. All the measurements presented in this chapter have been conducted at three or more source-nozzle distances, or so-called *sn* positions. The standard distance between the nozzle and skimmer in molecular beam instruments is approximately 10 *mm*. In the MAGIE apparatus, the standard distance is 11.6 *mm*. Following the standard MAGIE notation used in the group, this is equivalent to source-nozzle position $sn = 0$. Experiments at extreme values of the source-nozzle distances, limited by the mechanical movement of the source, have also been conducted. The minimum distance at 5.6 *mm* and the maximum distance at 17.6 *mm* are referred to as source-nozzle positions $sn = -6$ and $sn = +6$ respectively. All measurements, with the exception of the "Kurt skimmer" center line intensity measurements (Only 300 *K*), have also been conducted at two different temperatures. One where the beam has been cooled by liquid nitrogen to the minimum achievable stable temperature of 125 *K*, and one where the beam is at a room temperature of 300 *K*.

5.1   Virtual source measurements

Figure 5.1: *shows the measured virtual source diameter for the 4 μm and 390 μm skimmer against increasing pressures at a beam temperature of 125 K. Three different source-nozzle distances were used. The figure also show the simulated virtual source diameter with the continuum expansion model(CE) and the Bose-Einstein model (BE) for a Lennard-Jones potential (LJ) and a Hurly-Moldover potential (HM). Virtual source measurements conducted by Eder et al [23] have also been included in the figure. The simulations and measurements are taken from reference [23].*

Figure (5.1) shows the measured virtual source diameter for the 4 μm and 390 μm skimmers against increasing pressures at a beam temperature of 125 K. Three different source-nozzle distances were used. A description of the virtual source can be found in section (2.2.2). The measurements were conducted as explained in section (4.1). The virtual source diameters were extracted from the raw data following the procedure described in section 4.1.1. Apart from the measurements carried out as part of this thesis work, the figure also includes simulations of the virtual source size using the continuum-expansion model (CE) and the Bose-Einstein model (BE) with a Lennard-Jones potential (LJ) or a Hurly-Moldover potential (HM). Measurements conducted by Eder et al. are also included in this figure to compare our measurements with previously obtained virtual source measurements. These measurements were done with a 10 μm nozzle and a 400 μm skimmer

using the same helium microscope apparatus. Eder et al. measured the virtual source size using a Fresnel zoneplate to image the virtual source. They performed "Detector Arm" scans on the image of the virtual source utilizing a 25 μm slit or a 10 μm pinhole aperture. These results are referred to as *dv Slit Scanline* and *dv Pinhole Scanline* in figure (5.1). Eder et al. also measured the virtual source size with "Piezo Table" scans using the same slit or pinhole as the detector arm scans. These measurements are referred to as *dv Slit Piezo* and *dv Pinhole Piezo* in figure (5.1). The measurements and simulations are taken from reference [23]. Eder et al. concluded that the best description of the virtual source size experimental data is obtained with a continuum expansion model combined with a Lennard-Jones potential [23]. This simulation is referred to as $d_{CE}LJ$ $125K$ in the figure.

Comparing the experimental results from the 390 μm skimmer to the $d_{CE}LJ$ $125K$ simulation and previously published experimental results, good agreement is seen between the previous results and source-nozzle position $sn = +6$. However, there seems to be a dip in the curve between about 40 and 100 *bar* which is not visible in previous experimental results or theory. As the distance between skimmer and nozzle decrease the size of the virtual source is also observed to decrease, likely due to the free-jet expansion having not quite finished. In other words, we measure the virtual source while it is still expanding. Theoretical work on finding the exact "quitting surface" (see section (2.2.2)) is ongoing and these experiments can be used to contribute to that.

The effect is illustrated in figure (5.2) which shows three skimmer scans across the virtual source at a sec pressure with the three different source-nozzle distances.
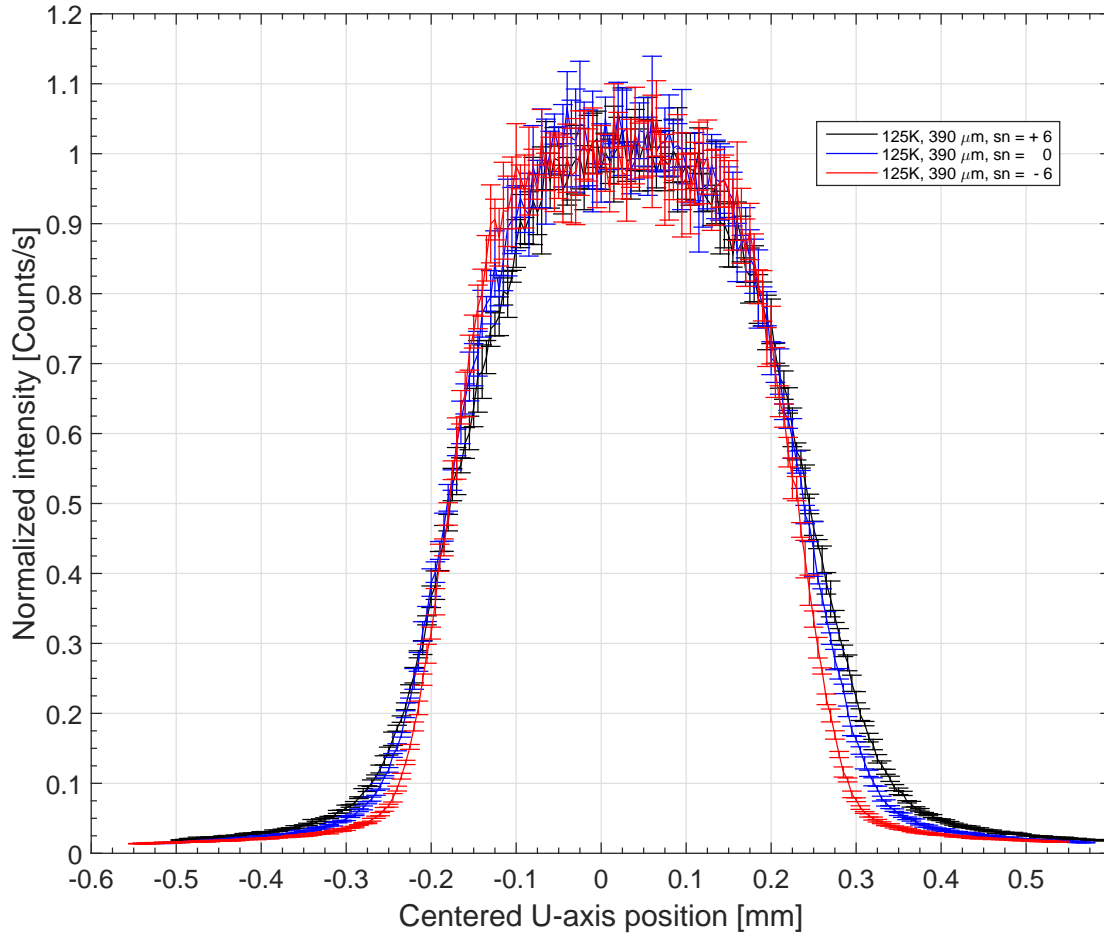
Figure 5.2: *shows the virtual source scans for the* 390 *μm skimmer with a beam temperature of* 125 *K at* 60 *bar for source-nozzle positions sn = +6, sn = 0 and sn = −6*

Surprisingly, the 4 μm skimmer does not follow the theoretical simulations or the previously conducted measurements at any source-nozzle distance. Given that the deconvolution (see section (4.1.1)) takes into account the skimmer size, it is expected to get the same result regardless of skimmer size, if anything the results measured with the small skimmer should be more correct. However, in reality they do not agree well with simulations or previous experimental results. We see the same trend that the closer the nozzle is to the skimmer, the smaller the virtual source size, but the overall size is significantly smaller. A possible explanation as to why the smaller skimmer yields a smaller virtual source size is related to the smaller cross sectional area of the skimmer orifice, and is discussed in section (5.1).
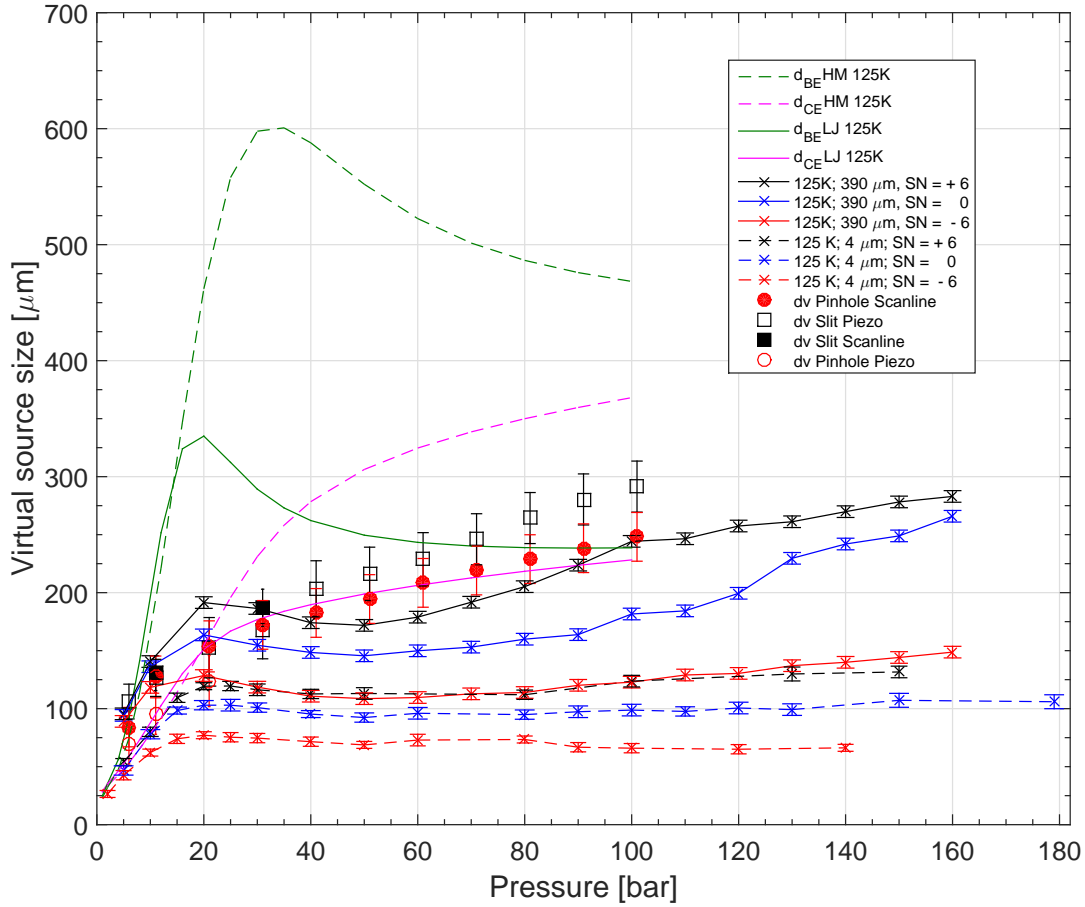
Figure (5.3) shows the measured virtual source diameter for the 4 μm and 390 μm skimmer against increasing pressures at a beam temperature of 300 K. Three different source-nozzle distances were used. The figure also includes simulations of the virtual source size using the continuum-expansion model with a Lennard-Jones potential or a Hurly-Moldover potential. Measurements conducted by Reisinger et al. [22] and DePonte et al. [13] are also included in this figure to compare our measurements with previously obtained virtual source measurements. The measurements done by Reisinger et al. were also performed

with MAGIE using a similar method for the measurements performed by Eder. et al., as described above. The measurements by DePonte et al. were carried out by another research group using another apparatus. They did their measurements by scanning a field ionization detector directly across the beam at a distance of 19.4 cm and then they extrapolated backwards to get the source size. The conclusion made by Reisinger et al. was also that the best description of the virtual source size experimental data is obtained with a continuum expansion model combined with a Lennard-Jones potential [22]. This simulation is referred to as $d_{CE}LJ$ 320K in the figure.
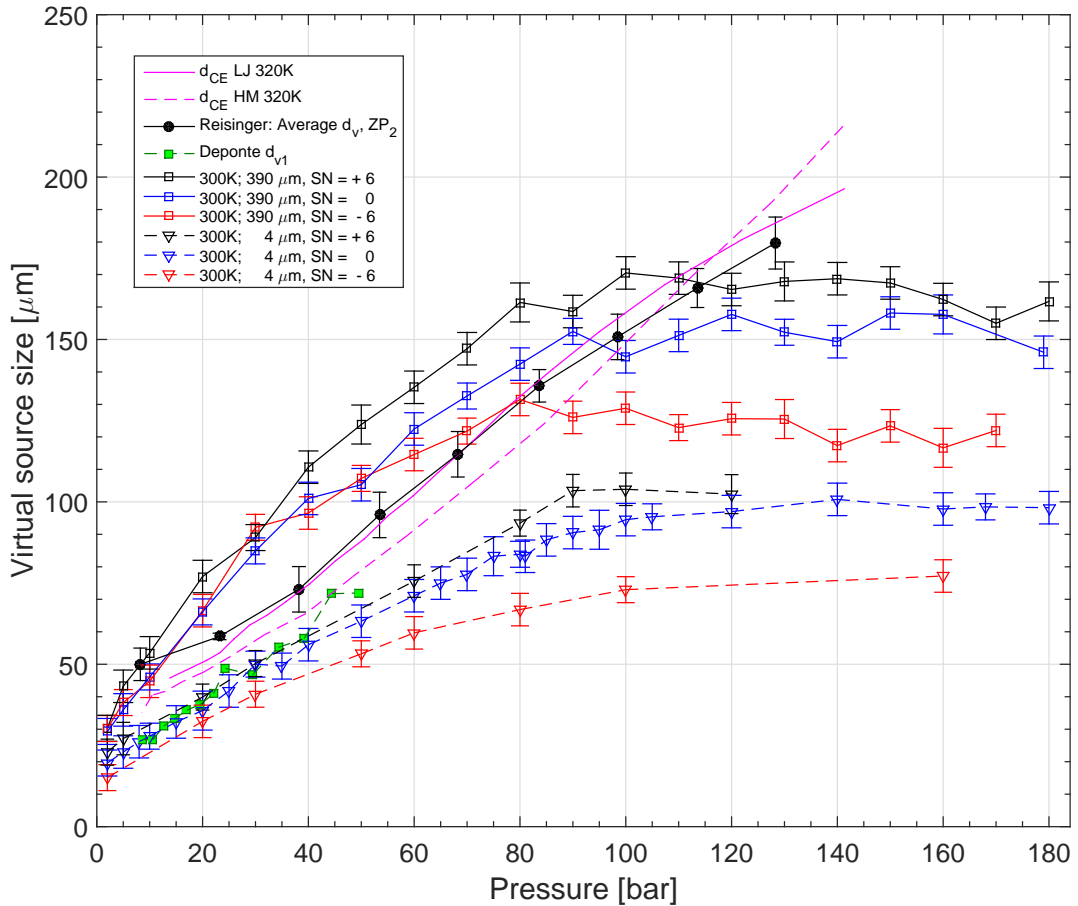
Figure 5.3: *shows the measured virtual source diameter for the 4 μm and 390 μm skimmer against increasing pressures at a beam temperature of 300 K. Three different source-nozzle distances were used. The figure also show the results of the measured virtual source diameter from DePonte [13] obtained using a 4.3 μm skimmer and a nozzle diameter of 9.5 μm at a temperature of 300 K (Our nozzle diameter is 10 μm). The virtual source size was obtained by forming an image of the virtual source using a 1.3 mm by 2 μm collimating slit aperture. Measurement results from Reisinger et al. conducted at a beam temperature of 320 K and a nozzle diameter of 10 μm [22] are also included. The figure also show the simulated 320 K virtual source diameters with the continuum expansion model for a Lennard-Jones potential (LJ) and a Hurly-Moldover potential (HM). These simulations are taken from reference [22].*

Firstly we observe that there is an excellent agreement between the experiments presented

here for the microskimmer and previously measured experimental results from DePonte et al. Comparing the experimental results from the 390 μm skimmer to the $d_{CE}LJ$ 320K we see there is still a reasonable agreement between our measurement data and the theoretical simulations, though not quite as good as for the cooled beam. In particular we can note that the virtual source size simulations have a larger virtual source at a cold beam temperature, and that the simulations conducted by Reisinger et al. were done with a beam temperature of 320 K. Therefore we can assume that the simulation curve should be a bit larger than it is. Eventually the measured virtual source size flattens out, and stays fairly consistent after a certain pressure is reached. This behaviour may be related to background interactions. As for the cold beam temperature, we see that the measured virtual source size for the smaller skimmer is much smaller than that of the larger skimmer. The curves for the small skimmer follow the same tendencies as the larger skimmer, having a larger virtual source size the further away the nozzle is to the skimmer. An explanation as to why there is a deviation from the larger skimmer measurements will be discussed below.

Discussion

The comparison between the cold and warm beam temperatures shown in figures (5.1) and (5.3) shows that the virtual source size at cold beam temperatures is larger. This is in agreement with [23] [22]. The most puzzling effect in the results is that the virtual source appears much smaller regardless of warm or cold when measured with the 4 μm skimmer compared to the 390 μm skimmer.

A possible explanation as to why the small skimmer provide a smaller virtual source could be related to the smaller cross sectional area of the small skimmer orifice. Because of the smaller orifice, helium atoms that would normally go through the orifice of a larger skimmer (390 μm) may instead collide with and be deflected off the conically shaped skimmer structure. The deflected helium atoms may then interact with the free-jet expansion itself, as the scattered helium atoms collide with helium atoms from the expansion. This backscattering of helium atoms interfering with the expansion atoms may cause the virtual source size to appear smaller than it actually is. This phenomenon would be particularly strong at low temperatures where the flow is higher and this is what can be see. However, one could just as well argue the other way around that the scattered atoms would cause a broadening of the beam leading to the virtual source size appearing larger. More detailed calculations that include the nozzle-skimmer interaction in the simulations are required. At present we must conclude that the effect is clearly there, but we cannot explain it.

5.2 Time of flight measurements
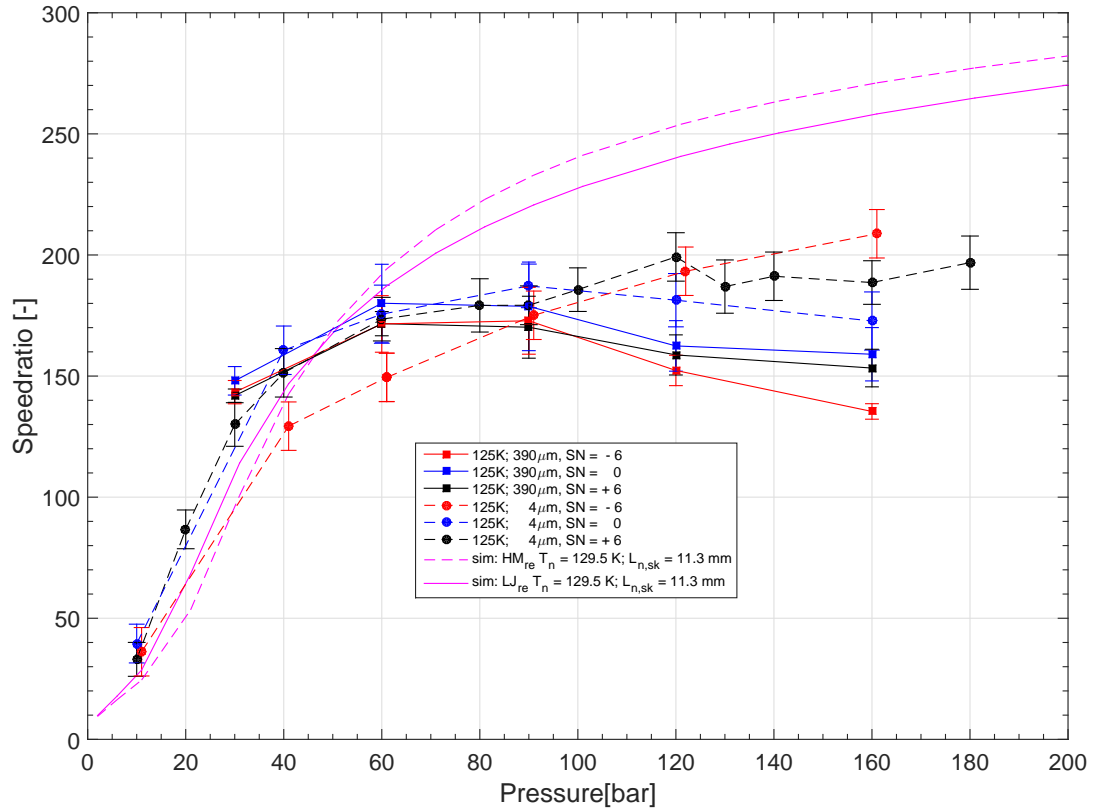
Figure 5.4: *shows the 125 K measured speedratios for the 4 μ skimmer and the 390 μm skimmer at source-nozzle position sn = 0 alongside theoretical speedratio simulations using a Lennard-Jones potential (LJ) and a Hurly-Moldover potential (HM). The simulations have been simulated for a beam temperature of 129.5 K and a source-nozzle distance ($L_{n,sk}$ in the plot legend) of 11.3 mm (Equivalent to a source-nozzle position of sn = −0.3)*

Figure (5.4) shows the measured speedratios at 125 K for the 4 μm skimmer and 390 μm skimmer at source-nozzle positions $sn = -6$, $sn = 0$ and $sn = +6$. The figure also includes theoretical simulations of the speedratios, where the speedratios have been simulated with a Lennard-Jones potential (LJ) and a Hurly-Moldover potential (HM) [45].

Figure (5.5) shows the 300 K measured speedratios for the 4 μm skimmer and 390 μm skimmer at source-nozzle positions $sn = -6$, $sn = 0$ and $sn = +6$. The figure also includes theoretical simulations of the speedratios, where the speedratios have been simulated using a Lennard-Jones potential (LJ) and a Hurly-Moldover potential (HM).
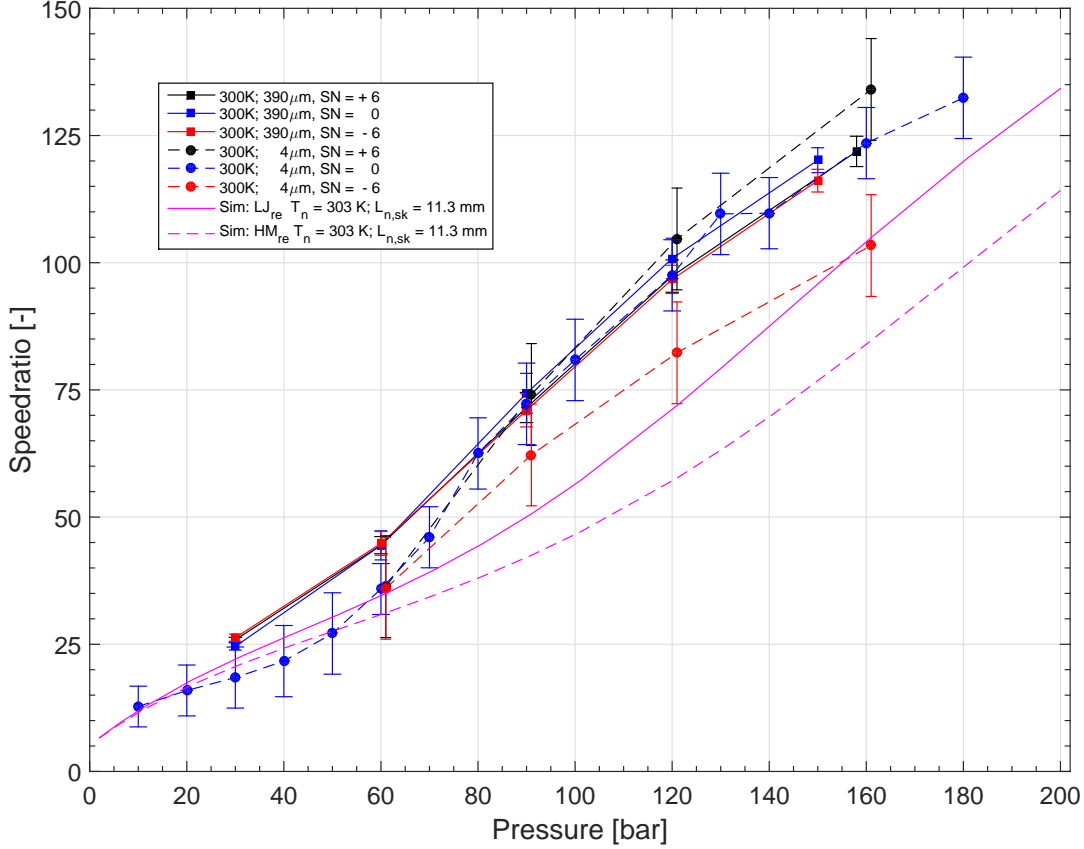
Figure 5.5: *shows the* 300 *K measured speedratios for the* 4 *μ skimmer and the* 390 *μm skimmer at source-nozzle position sn = 0 alongside theoretical speedratio simulations using a Lennard-Jones potential (LJ) and a Hurly-Moldover potential (HM). The simulations have been simulated for a beam temperature of* 303 *K and a source-nozzle distance ($L_{n,sk}$ in the plot legend) of* 11.3 *mm (Equivalent to a source-nozzle position of sn = −0.3)*

Discussion

The results shown in figures (5.4) and (5.5) show that the speedratios from the 390 *μm* and 4 *μm* skimmer are not deviating much from each other. This suggests that the beams monochromaticity, a very important parameter of the beam, is not affected by the diameter of the skimmer orifice. Both of these figures shows that the measured results follow the theoretical simulations at lower beam pressures, but start to deviate from the simulated speedratios at higher pressures. The measured speedratios appear larger than the simulations having a warm beam temperature, and they appear smaller than the simulations having a cold beam temperature. The flattening out of the speedratios that is observed for the warm beam, has often been observed in other molecular beam instruments. The general belief is that it is related to insufficient pump performance. The gas-inlet at larger pressures is too high and the increased background in the chamber leads to an increase in the collisions of the beam with the background gas, which gives the broadening. As for the cold beam, we do not at present have a satisfying explanation as to why the speedratio appears better than what theory predicts.

5.3 Center line intensity measurements
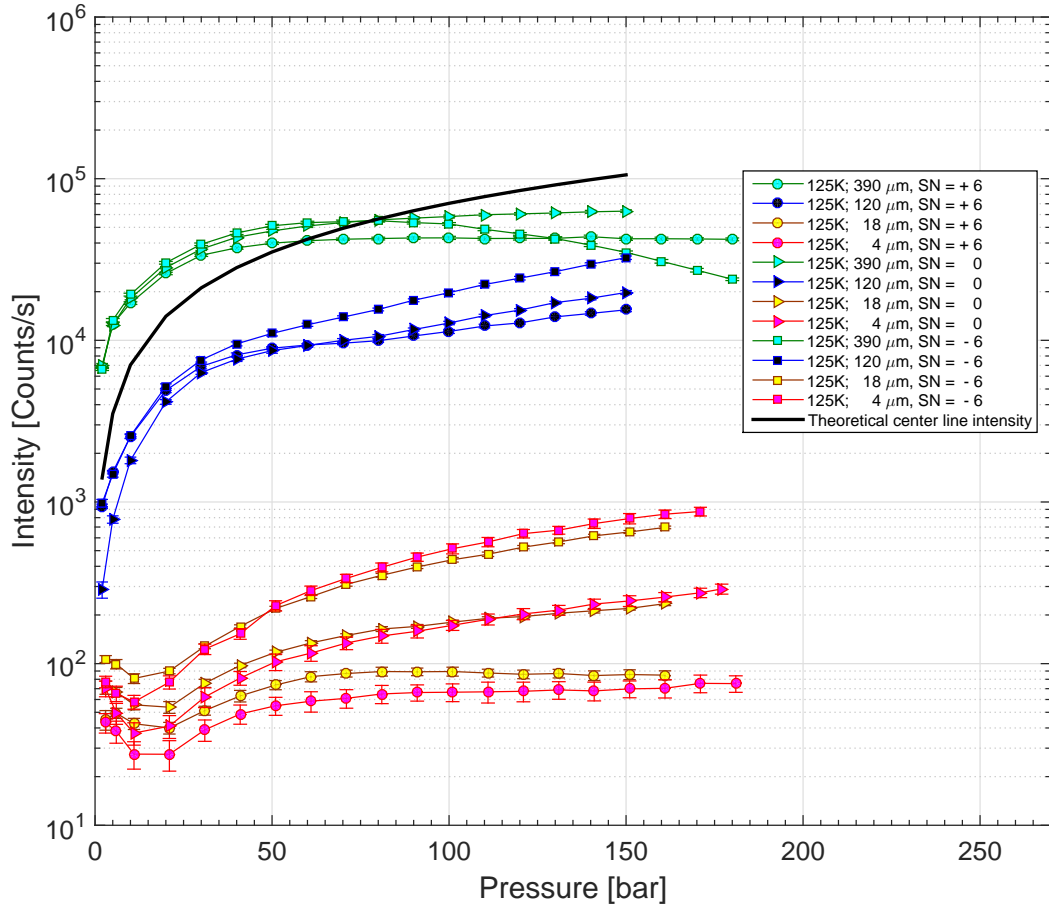
Figure 5.6: *Figure shows the* 125 *K cold beam measured center line intensity for all skimmer at different pressures for source-nozzle positions sn = +6, sn = 0 and sn = −6. The figure also shows the theoretical center line intensity obtained with a detector efficiency of* 2.1 *ionizations per incident helium atom [44].*

Figure (5.6) shows the measured center line intensities at 125 K for the all skimmers skimmer at source-nozzle positions $sn = +6$, $sn = 0$ and $sn = -6$. A description of how the measurements were carried out can be found in section (4.3). The figure also includes the theoretical center line intensity with a detector efficiency of $2.1 \cdot 10^{-6}$. This comes from our detector utilizing an emission current of 4 A and is shown in reference [44]. The theoretical center line intensity is discussed in section (2.2.3). Here it is important to remember that in theory the center line intensity should be independent of the skimmer size. The 390 μm skimmer seems to follow the theoretical center line intensity fairly well. The exception is at source-nozzle position $sn = -6$, where we see a drop in intensity at higher pressures. This may be due to over saturation in the detector or background interaction. For the other skimmers the shortest distance between nozzle and skimmer seems to provide the largest center line intensity. It is very clear that the reduction of the skimmer orifice has a strong influence on the center line intensity. The smaller the

skimmer orifice the smaller the intensity. The 18 μm and 4 μm skimmers fall far below
the theoretical center line intensity.
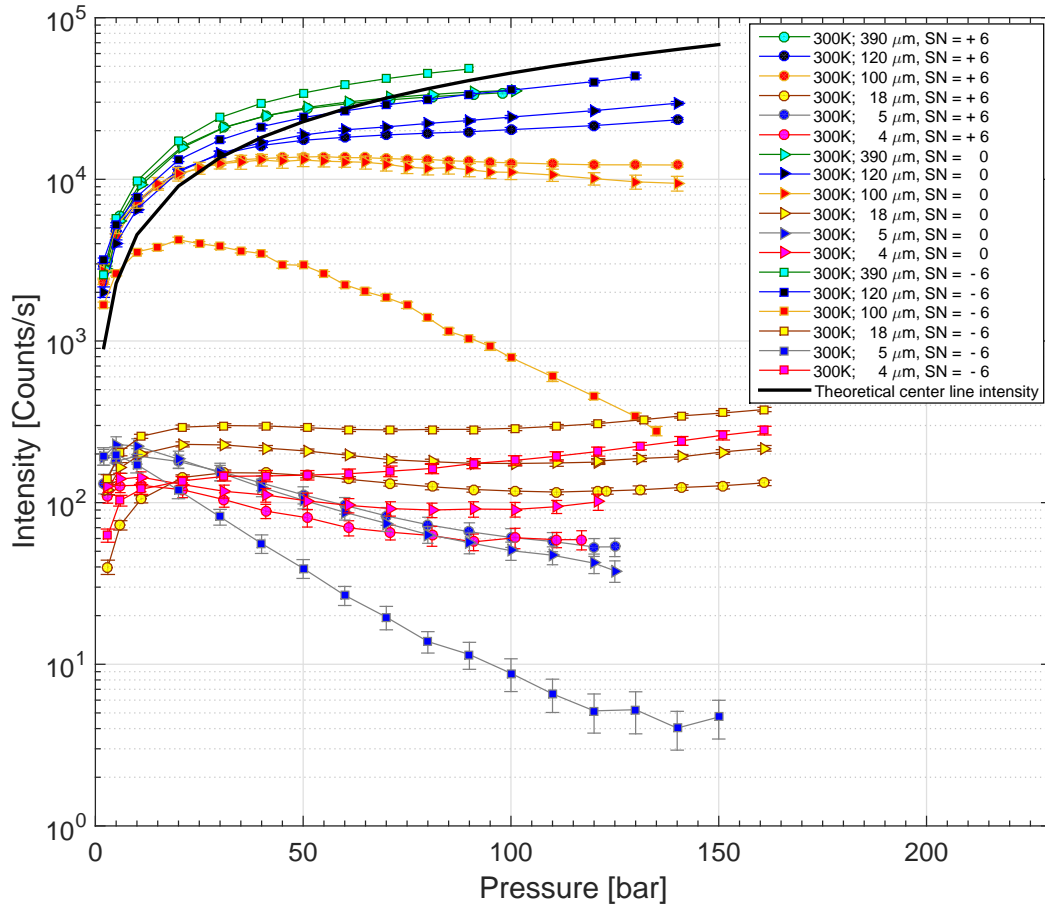
Figure 5.7: *shows the* 300 *K warm beam measured center line intensity for all skimmer at
different pressures for source-nozzle positions sn* = +6, *sn* = 0 *and sn* = −6. *The figure
also shows the theoretical center line intensity obtained with a detector efficiency of* 2.1
ionizations per incident helium atom [44].

Figure (5.7) shows the measured center line intensities at 300 K for the all skimmers skim-
mer at source-nozzle positions $sn = +6$, $sn = 0$ and $sn = -6$. The figure also includes the
theoretical center line intensity with a detector efficiency of $2.1 \cdot 10^{-6}$ as stated in reference
[44] by use of a 4 A emission current for the detector. At a warm beam temperature,
we see the same trend as we did for the cold beam temperature: There is a huge loss in
intensity having a smaller skimmer orifice. The 390 μm and 120 μm skimmers both follow
the theoretical center line intensity very well, and as for the cold beam temperature we
see a larger center line intensity at short skimmer-nozzle distances. This is not the case
however for the behaviour of the 5 μm and 100 μm Kurt skimmer. For the Kurt skimmer,
there is a larger center line intensity at long nozzle-skimmer distances, and at source-nozzle
position $sn = -6$ there is a huge loss in intensity with increasing pressure.

Discussion

The main conclusion that can be drawn from the center line measurement presented in figures (5.6) and (5.7) is that the smaller the skimmer, the larger the intensity loss along the center line. Theoretically the center line intensity should remain unaffected by the skimmer size (see section (2.2.3)), but as seen in the experimental results this is clearly not the case. This is a very important result since it affects the whole design of the helium microscope, which was based on the assumption that the center line intensity would be constant [14]. It is also very surprising given that the time of flight measurements showed no noticeable difference in beam quality. A possible explanation as to why there is a reduction in the center line intensity for the smaller skimmer diameters is related to the mean free path of the helium atoms at the skimmer orifice opening. If the mean free path of the helium atoms entering the skimmer orifice and the orifice diameter is of the same magnitude, there will be additional collisions between the helium atoms. The increased collision frequency will interfere with the straight forward trajectory helium atoms, scattering them out of the center line. This will lead to a reduction in the intensity of the center line without changing the velocity distribution of the beam.

The Kurt skimmer appears to have an even stronger loss in intensity than the other skimmers, particularly at small source-nozzle distances, i.e. $sn = -6$. A possible explanation for this is the shape of the skimmer. The front of the Kurt skimmer is flat with a small hole, and inside this hole the small pinhole aperture is located. A picture and a schematic are shown in figures (3.8) and (3.9). The two flat surfaces in front of the skimmer provides the helium atoms with ample opportunity to collide head-on with the skimmer instead of being deflected away by hitting the side of the skimmer. The helium atoms reflected in front of the skimmer can then interact with the helium atoms that would otherwise go through the skimmer orifice opening.

CONCLUSION AND OUTLOOK

In this thesis the behaviour of free-jet expansion beams have been studied in three different measurement series: The virtual source scans, the center line intensity measurements and the time of flight measurements. The measurements were conducted using skimmers of varying shape and orifice diameter to investigate how the characteristics of the beam change. The results were compared with previously published measurements and theoretical calculations. The work presented here is the first larger study of molecular beams created using microskimmers. The results are reproducible, consistent and, where there is an overlap, they agree well with previously published measurements. The three major effects that were observed are:

1. The virtual source appears significantly smaller when observed with a microskimmer. In the range where there is an overlap, the measurements agree extremely well with previous microskimmer measurements performed by DePonte et al. The effect must be related to skimmer interactions, but at the moment we have no proper explanation.

2. One of the main characteristics of the beam is the monochromaticity, and this is a very important factor when it comes to imaging. In the microscope the beam is focussed using a Fresnel zoneplate which suffers from chromatic aberrations [28], so the larger the speedratio, the better the monochromaticity and the better the focus. As previously mentioned, the skimmers that would give the smallest focal spot size are the small skimmers. The time of flight measurement results yield a very positive result for us. The results from figures (5.4) and (5.5) show that the monochromaticity stays much the same for the 4 μm skimmer and 390 μm skimmer, meaning we can use a small skimmer and maintain the same degree of monochromaticity as if we had a larger skimmer in place.

3. From the center line intensity measurements we see that the micro skimmers do not follow the expected theoretical center line intensity given by equation (2.11), and this is a result that is very bad for us and our microscope. What we see from figures (5.6) and (5.7) is that the center line intensities for the microskimmers are very low, and this makes the detection of the signal much harder. A possible explanation for the decreasing center line intensities at smaller skimmer orifices is related to the mean free path within the orifice opening. A local pressure increase surrounding the orifice

hole will reduce the mean free path in this area. In cases where the orifice diameter and this mean free path are of the same magnitude, additional collisions between the helium atoms might lead to a reduction of the beam intensity by scattering atoms out of the center line.

6.1   Future work

During this thesis not all measurements were conduced for all skimmers. To get a complete picture of the effect that the microskimmers have on the beam properties this has to be done. The virtual source measurements for the 5 μm, 18 μm, 100 μm and 120 μm skimmers have not been measured at either warm or cold beam temperatures. This also applies to the time of flight measurements. However, there is currently a large data set available for theoretical work. Hopefully a more complete model of the beam creation will soon be available, allowing us to find the optimum design parameters for the microscope design. It is quite possible that the microskimmers will have to be abandoned all together and an alternative solution developed.

MATLAB CODE

A.1 Source scan analysis

```matlab
1  % This program is used for the analysis of the virtual source scans. The
2  % scan files are accessed and the wanted variable data sets extracted.
3  % The program generates a fitted curve to the data points by utilizing two
4  % different approaches; Error functions and convolution. Parameters are
5  % extracted from the fits, and the virtual source size is calculated.
6  clear all;
7
8  slit_width_um = 390; %Of users choosing (skimmer opening diameter)
9  x0_U = [0.100/(2*sqrt(2*log(2))),6.9,slit_width_um]; %[sigma, mu, slit_width_um
        ]';
10  x0_V = [0.100/(2*sqrt(2*log(2))),10.1,slit_width_um];
11
12  l = 10;
13  U_peak_mean_index_1 = 105;
14  U_peak_mean_index_2 = 120;
15
16  V_peak_mean_index_1 = 95;
17  V_peak_mean_index_2 = 110;
18
19  Source_scan_file_U = '0988';
20  Source_scan_file_V = '0925';
21  pressure = '160';
22
23  temperature = '125K';
24  SNpos = 'minus6mm_pos';
25
26  path_end = '\';
27  path_base = 'C:\Users\Truls\Desktop\Data\MEASUREMENTS_SOURCE_SCANS\390
        um_skimmer_Source_scans\';
28  path = sprintf('%s%s%s%sbar%s%s',path_base,temperature,path_end,pressure,
        path_end,SNpos);
29  filename_U = sprintf('%s%sFind Beam_AXIS 1_%s.dat', path,path_end,
        Source_scan_file_U);
```

```matlab
30  filename_V = sprintf('%s%sFind Beam_AXIS 2_%s.dat', path,path_end,
        Source_scan_file_V);
31
32  header_end = '%end_header
        ################################################################';
33
34  [C_U,A_U] = ImportData(filename_U,header_end);
35  [C_V,A_V] = ImportData(filename_V,header_end);
36
37  bGround_U = mean(A_U.data(1:l,4));
38  bGround_V = mean(A_V.data(1:l,4));
39
40  x_U_mm = (A_U.data(:,2) *(1e3));
41  y_U = (A_U.data(:,4)- bGround_U)/mean(A_U.data(U_peak_mean_index_1:
        U_peak_mean_index_2,4)- bGround_U);
42  err_U = A_U.data(:,5)/(mean(A_U.data(U_peak_mean_index_1:U_peak_mean_index_2,4)
        - bGround_U));
43
44  xBackground_U = x_U_mm(1:l);
45  yBackground_U = y_U(1:l);
46  xPeak_mean_U = x_U_mm(U_peak_mean_index_1:U_peak_mean_index_2);
47  yPeak_mean_U = y_U(U_peak_mean_index_1:U_peak_mean_index_2);
48
49  x_V_mm = A_V.data(:,3)*(1e3);
50  err_V = A_V.data(:,5)/(mean(A_V.data(V_peak_mean_index_1:V_peak_mean_index_2,4)
        - bGround_V));
51  y_V = (A_V.data(:,4)- bGround_V)/mean(A_V.data(V_peak_mean_index_1:
        V_peak_mean_index_2,4)- bGround_V);
52  xBackground_V = x_V_mm(1:l);
53  yBackground_V = y_V(1:l);
54  xPeak_mean_V = x_V_mm(V_peak_mean_index_1:V_peak_mean_index_2);
55  yPeak_mean_V = y_V(V_peak_mean_index_1:V_peak_mean_index_2);
56
57
58  %% ERROR FUNCTION
59  ft_U = fittype('((a/2)*(erf((x - mu - 0.390/2)/(-sigma*sqrt(2))) - erf((x - mu
        + 0.390/2)/(-sigma*sqrt(2))))) + b');
60  Fitted_U = fit(x_U_mm,y_U,ft_U,'StartPoint',[1,0,x0_U(2),x0_U(1)]);
61  error_fit_U = confint(Fitted_U,0.95);
62  Coefficients_fit_U = coeffvalues(Fitted_U);
63  FWHM_U = 2*sqrt(2*log(2))*(Coefficients_fit_U(1,4))*(1e3);
64  FWHM_U_err = (abs(error_fit_U(1,2)-error_fit_U(2,2)))*(1e3);
65
66  ft_V = fittype('((a/2)*(erf((x - mu - 0.390/2)/(-sigma*sqrt(2))) - erf((x - mu
        + 0.390/2)/(-sigma*sqrt(2))))) + b');
67  Fitted_V = fit(x_V_mm,y_V,ft_V,'StartPoint',[1,0,x0_V(2),x0_V(1)]);
68  error_fit_V = confint(Fitted_V,0.95);
69  Coefficients_fit_V = coeffvalues(Fitted_V);
70  FWHM_V = 2*sqrt(2*log(2))*(Coefficients_fit_V(1,4))*(1e3);
71  FWHM_V_err = (abs(error_fit_V(1,2)-error_fit_V(2,2)))*(1e3);
72
73  %% CONVOLUTION
```

```matlab
74   [x_U,resnorm_U,residual_U,exitflag_U,output_U,lambda_U,jacobian_U] =
         lsqcurvefit(@my_convolution,x0_U,x_U_mm,y_U);
75   FWHM_mm_conv_U = (2.*sqrt(2.*log(2))).*x_U(1);
76   ci_conv_U = nlparci(x_U,residual_U,'Jacobian',jacobian_U);
77   FWHM_mm_conv_U_err = abs(ci_conv_U(1,1)-ci_conv_U(1,2))*(1e3);
78
79   [x_V,resnorm_V,residual_V,exitflag_V,output_V,lambda_V,jacobian_V] =
         lsqcurvefit(@my_convolution,x0_V,x_V_mm,y_V);
80   FWHM_mm_conv_V = (2.*sqrt(2.*log(2))).*x_V(1);
81   ci_conv_V = nlparci(x_V,residual_V,'Jacobian',jacobian_V);
82   FWHM_mm_conv_V_err = abs(ci_conv_V(1,1)-ci_conv_V(1,2))*(1e3);
83
84
85   %% PLOT
86   output = sprintf('Erf_U\tErf_err_U\tConv_U\tConv_err_U\tErf_V\tErf_err_V\
         tConv_V\tConv_err_V\n%f\t%.0f\t%.0f\t%.0f\t%.0f\t%.0f\t%.0f\t%.0f\t%.0f\n',
         str2double(pressure),FWHM_U,FWHM_U_err,FWHM_mm_conv_U.*(1000),
         FWHM_mm_conv_U_err,FWHM_V,FWHM_V_err,FWHM_mm_conv_V.*(1000),
         FWHM_mm_conv_V_err)
87
88   Convolution_U = my_convolution(x_U,x_U_mm);
89   Convolution_V = my_convolution(x_V,x_V_mm);
90
91   %% Plotting
92   figure_Source_scans = figure(01);
93
94   %% SUBPLOT 1
95   subplot(2,1,1);
96   errorbar(x_U_mm,y_U,err_U,'-ob','markersize',3);
97   hold on;
98   plot(Fitted_U,'black');
99   plot(x_U_mm,Convolution_U,'-or','markersize',3);
100  plot(xPeak_mean_U,yPeak_mean_U,'-og','markersize',3);
101  plot(xBackground_U,yBackground_U,'-ok','markersize',7);
102  hold off;
103
104  legend('Experimental data','Error function fit','convolution fit');
105  title('Source scan: U - Axis')
106  ylabel('Intensity [Counts/s]');
107  xlabel('Position U - Axis [mm]');
108  grid on;
109
110  %% SUBPLOT 2
111  subplot(2,1,2);
112  errorbar(x_V_mm,y_V,err_V,'-ob','markersize',3);
113  hold on;
114  plot(Fitted_V,'black');
115  plot(x_V_mm,Convolution_V,'-or','markersize',3);
116  plot(xPeak_mean_V,yPeak_mean_V,'-og','markersize',3);
117  plot(xBackground_V,yBackground_V,'-ok','markersize',7);
118  hold off;
119
```

```matlab
120  legend('Experimental data','Error function fit','convolution fit');
121  title('Source scan: V - Axis')
122  ylabel('Intensity [Counts/s]');
123  xlabel('Position V - Axis [mm]');
124  grid on;
125
126
127  %% Save plot
128  savePathPDF = 'C:\Users\Truls\Documents\MATLAB_figures\PDF\';
129  savePathFIG = 'C:\Users\Truls\Documents\MATLAB_figures\FIG\';
130
131  pdf_file_save_name = sprintf('Source_Scan__at_%sbar_%s_U_%s_V_%s.pdf',pressure,
         SNpos,Source_scan_file_U,Source_scan_file_V);
132  pdf_save = strcat(savePathPDF, pdf_file_save_name);
133  saveas(gcf,pdf_save,'pdf');
134
135  figure_file_save_name = sprintf('Source_Scan__at_%sbar_%s_U_%s_V_%s.fig',
         pressure,SNpos,Source_scan_file_U,Source_scan_file_V);
136  figure_save = strcat(savePathFIG, figure_file_save_name);
137  savefig(gcf,figure_save,'compact');
```

Function: ImportData.m

```matlab
1   % Function extacts the data and the text from a file and seperates them
2   % into two seperate arrays. The arrays are returned.
3
4   function [Textfile,Datafile] = importData(path_and_filename,header_end)
5
6   delimiter = '\t';
7   formatSpec = '%s%[^\n\r]';
8   Textfile = textread(path_and_filename, '%s','delimiter', '\n');
9
10  len = length(Textfile);
11
12  line_nr_before_data = 0;
13
14  for j=1:len,
15      tf = strcmp(Textfile(j,1),header_end);
16    if tf == true,
17          line_nr_before_data = j;
18    end
19  end
20
21  header_line = line_nr_before_data;
22  Datafile = importdata(path_and_filename,delimiter,header_line);
```

Function: define_slit.m

```matlab
1   % Function takes inn a vector containing a mean value, a standard deviation
2   % and a set of coordinates. The set of coordinates are used to generate a
```

```matlab
3    % trapezoidal slit. The slit values are returned to the user.
4    function slit = define_slit(x,xdata)
5        slitwidth_mm = x(3)/1000;
6
7        slit_x_coordinate_1 = x(2) - slitwidth_mm/2;
8        slit_x_coordinate_2 = x(2) + slitwidth_mm/2;
9
10       slit = trapmf(xdata,[slit_x_coordinate_1 slit_x_coordinate_1
              slit_x_coordinate_2 slit_x_coordinate_2]);
11   end
```

Function: gaussian_pdf.m

```matlab
1    % Function takes inn a vector of a mean value, a standard deviation and
2    % a set of coordinates. An array of datapoints is also taken inn. A
3    % gaussian function is created with the set mean value and standard
4    % deviation over the data array. The array of gassian values is returned.
5    function return_value = gaussian_pdf(x,x_data)
6
7    sigma = x(1);
8    mu = x(2);
9
10   return_value = (1/(sigma.*sqrt(2*pi))).*exp((-(x_data-mu).^2)/(2.*sigma.^2));
11   end
```

Function: my_convolution.m

```matlab
1    % Function takes an array of data and a vector containing a mean value,
2    % a standard deviation and a set of coordinates for a slit. A gaussian is
3    % created, along with a slit, and the convolution of the gaussian and the
4    % slit is made to fit the data by adjusting the mean value and standard
5    % deviation of the gaussian. The normalized convolution data is returned.
6
7    function convolution_norm = my_convolution(x,xdata)
8
9    my_gauss = gaussian_pdf(x,xdata);
10   trap = define_slit(x,xdata);
11
12   convolution = conv(my_gauss,trap,'same');
13   convolution_norm = convolution/max(convolution);
14
15   end
```

A.2   Center line intensity analysis

```matlab
 1  % This program opens the center line intensity measurement files and
 2  % extracts the wanted variable data sets. The center line intensity is then
 3  % plotted in a graph.
 4  clear all;
 5
 6  file_scan = '01098';
 7  file_background = '01099';
 8
 9  path_end = '\';
10  path = 'Z:\MEASUREMENTS\Center_Line_Intensity_Scans\5um\200um_aperture\
         plus3mm_pos';
11
12  headerend = '%end_header
         ################################################################';
13
14  filename_scan = sprintf('%s%sSCAN_%s.dat', path,path_end,file_scan);
15  [C_scan,A_scan] = ImportData(filename_scan,headerend);
16
17  filename_background = sprintf('%s%sSCAN_%s.dat', path,path_end,file_background)
         ;
18  [C_background,A_background] = ImportData(filename_background,headerend);
19
20  pressure = A_scan.data(:,4);
21  signal = A_scan.data(:,2);
22  background = A_background.data(:,2);
23
24  corrected_signal = signal - background;
25  error = A_scan.data(:,3);
26
27  fig = figure(01);
28  errorbar(pressure,corrected_signal,error);
29  grid;
30  ylabel('Signal [Counts/s]');
31  xlabel('Pressure [bar]');
32  legend('300K; 390\mum, SN = + 6 mm');
```

A.3 Time of flight analysis

```matlab
% This program is used for the linear time of flight analysis of the
% speedratios. The time of flight measurement files are accessed, and
% the wanted variable data sets are extracted. The intensity curve is
% created and two linear fits are fitted to their respective sections
% of the curve. The intersection is found, and the 'perfect slit' edge
% is calculated. The uncertainties of the speedratios are calculated and
% a weighted linear fit is fitted to the speedratio curve. The intersection
% of the linear speedratio curve and the perfect slit edge is found,
% and hence the speedratio value with the linear extrapolation is found.
clear all;

Pressure = '120';
fileScanIntTOF = '00862';
fileScanInt = '00863';
date = '12062014';

temp = '300K';
SNpos = 'minus_6mm_pos';

lin_fit_index_line1_1 = 6;
lin_fit_index_line1_2 = 9;
lin_fit_index_line2_1 = 10;
lin_fit_index_line2_2 = 12;

uncertainty_tf  = 1*(1E-6);
uncertainty_FWHM = 1*(1e-6);

path_end = '\';
path_base = 'Z:MEASUREMENTS\';
path = sprintf('%s%s%s%s%s%sbar%s%s',path_base,date,path_end,temp,path_end,
    Pressure,path_end,SNpos);
headerend = '%end_header
    ################################################################';

filenameScanIntTOF = sprintf('%s%sSCAN_%s.dat', path,path_end,fileScanIntTOF);
[CScanIntTOF,AScanIntTOF] = ImportData(filenameScanIntTOF,headerend);

filenameScanInt = sprintf('%s%sSCAN_%s.dat', path,path_end,fileScanInt);
[CScanInt,AScanInt] = ImportData(filenameScanInt,headerend);

v = AScanIntTOF.data(:,4);
FWHM = AScanIntTOF.data(:,2);
tf = AScanIntTOF.data(:,1);

a = AScanIntTOF.textdata(:,2);
b = str2double(a);

CP1 = AScanIntTOF.data(:,9);
```

```matlab
47  CP2 = AScanInt.data(:,4);
48  Intensity1 = b(~isnan(b));
49  Intensity2 = AScanInt.data(:,2);
50
51  Intensity = [Intensity1;Intensity2];
52  CP = [CP1;CP2];
53  S = AScanIntTOF.data(:,3);
54
55  %% ERROR BARS
56  h = AScanIntTOF.textdata(:,4);
57  TOF_files = get_TOF_files_from_SCAN(h(45:end,1));
58
59  Uncertainty_S = [];
60
61  for i=1:length(S),
62  Uncertainty_S(i,1) = Calculate_uncertainty_S(path,TOF_files{i},tf(i,1)*(1e-6),
        FWHM(i,1)*(1e-6),uncertainty_tf,uncertainty_FWHM);
63  end
64  Error_bars_S = Uncertainty_S;
65
66  %% Fits to intensity curve
67  fit_line1 = fit(CP(lin_fit_index_line1_1:lin_fit_index_line1_2), Intensity(
        lin_fit_index_line1_1:lin_fit_index_line1_2),'poly1');
68  fit_line2 = fit(CP(lin_fit_index_line2_1:lin_fit_index_line2_2), Intensity(
        lin_fit_index_line2_1:lin_fit_index_line2_2),'poly1');
69
70  Coefficients_line1 = coeffvalues(fit_line1);
71  Coefficients_line2 = coeffvalues(fit_line2);
72
73  intersectX = ((Coefficients_line2(1,2) - Coefficients_line1(1,2))/(
        Coefficients_line1(1,1)-Coefficients_line2(1,1)));
74  edgeValue = intersectX + 0.1474534784;
75
76  %% Fit to speedratio curve
77  w = [];
78  for i = 1:length(Error_bars_S),
79      w(i,1) = 1/(Error_bars_S(i,1).^2);
80  end
81
82  fit_lin_to_Speedratios = fit(CP1,S(~isnan(S)),'poly1','Weights',w);
83  Coefficients_lin_fit_to_speedratios = coeffvalues(fit_lin_to_Speedratios);
84  error_fit_lin_S = confint(fit_lin_to_Speedratios,0.75);
85
86  x = (CP1(1,1):0.01:edgeValue);
87
88  Error_fit_lin_S_1 = error_fit_lin_S(1,1)*x + error_fit_lin_S(1,2);
89  Error_fit_lin_S_2 = error_fit_lin_S(2,1)*x + error_fit_lin_S(2,2);
90
91  intersect_linS = (Coefficients_lin_fit_to_speedratios(1,1)*edgeValue)+
        Coefficients_lin_fit_to_speedratios(1,2);
92  intersect_linS_error_1 = (error_fit_lin_S(1,1)*edgeValue)+error_fit_lin_S(1,2);
93  intersect_linS_error_2 = (error_fit_lin_S(2,1)*edgeValue)+error_fit_lin_S(2,2);
```

```matlab
 94
 95  uncertainty_intersection_lin_S = ((intersect_linS - intersect_linS_error_1) + (
         intersect_linS_error_2 - intersect_linS ))/2;
 96  pm = '\pm';
 97  strIntersect_linS = sprintf('S = %.2f %s %.2f',intersect_linS,pm,
         uncertainty_intersection_lin_S);
 98
 99  graph_plot_length = (S(end,1) - S(1,1));
100  L = graph_plot_length + intersect_linS;
101
102  strIntersect = sprintf('Intersection: X = %f',intersectX);
103  infoStr = sprintf('%s\n%s',strIntersect,strIntersect_linS)
104
105  fitArray1_X = lin_fit_index_line1_1:1:lin_fit_index_line1_2;
106  fitArray1_X_transposed = transpose(fitArray1_X);
107  fitArray1_Y = Intensity(lin_fit_index_line1_1:lin_fit_index_line1_2);
108
109  fitArray2_X = lin_fit_index_line2_1:1:lin_fit_index_line2_2;
110  fitArray2_X_transposed = transpose(fitArray2_X);
111  fitArray2_Y = Intensity(lin_fit_index_line2_1:lin_fit_index_line2_2);
112
113  fitIndexIntensity1 = fit(fitArray1_X_transposed, fitArray1_Y,'poly1');
114  fitIndexIntensity2 = fit(fitArray2_X_transposed, fitArray2_Y,'poly1');
115
116  %% Save figure output parameters
117  SNpos_split = strsplit(SNpos,'mm');
118  pmSNpos = SNpos_split(1,1);
119
120  k1 = strfind(pmSNpos, 'plus');
121  k1{1};
122  if k1{1} == 1
123      SN_num = '+6';
124  end
125
126  k2 = strfind(pmSNpos, 'minus');
127  if k2{1} == 1
128      SN_num = '-6';
129  end
130
131  k3 = strfind(pmSNpos, '0');
132  if k3{1} == 1
133      SN_num = '0';
134  end
135
136  total_SN_distance = 11.6 + str2double(SN_num);
137
138  %% Intensity CP edge determination plot
139  titlestring = sprintf('Linear extrapolation at p_0 = %s [bar], T_N = %s, Source
         -Nozzle position: %s (%.1f [mm])',Pressure,temp, SN_num,total_SN_distance);
140
141  Intensity_intersection = figure(01);
142  plot(CP,Intensity,'ob');
```

```
143   hold on;
144   plot(fit_line1,'-k');
145   plot(fit_line2,'--k');
146   text(0.7,2E4,strIntersect)
147   hold off;
148
149   title(titlestring);
150   ylabel('Intensity [Counts/s]');
151   xlabel('CP [inch]');
152   legend('Measurement data','Linear fit 1','Linear fit 2');
153
154   %% Linear extrapolation plot
155   Linear_fit_fig = figure(02);
156
157   plot(CP1,S(~isnan(S)),'ob');
158   hold on;
159   ylim([(S(1) - (L/100)*10) (intersect_linS + (L/100)*10)]);
160   xlim([0.66 1.2]);
161   yL = get(gca,'YLim');
162   plot(fit_lin_to_Speedratios,'black');
163   plot(([edgeValue edgeValue]),yL,'--r');
164   plot([0.66 1.2],[intersect_linS intersect_linS],'--r')
165   errorbar(CP1,S(~isnan(S)),Error_bars_S);
166
167   plot(x,Error_fit_lin_S_1,'k:');
168   plot(x,Error_fit_lin_S_2,'k:');
169
170   grid;
171   ylabel('Speedratio');
172   xlabel('CP [inch]');
173   title(titlestring);
174   text(0.7,(intersect_linS + (L/100)*5),strIntersect_linS);
175   legend('Calcuated Speedratios','Linear fit','location','best');
176   hold off;
177
178   %% Intensity Index plot
179   Intensity_vs_index_fig = figure(03);
180   plot(Intensity,'ob');
181   hold on;
182   plot(fitArray1_X,Intensity(lin_fit_index_line1_1:lin_fit_index_line1_2),'or');
183   plot(fitArray2_X,Intensity(lin_fit_index_line2_1:lin_fit_index_line2_2),'og');
184   plot(fitIndexIntensity1,'-k');
185   plot(fitIndexIntensity2,'--k');
186   hold off;
187
188   ylabel('Intensity [Counts/s]');
189   xlabel('Index');
190   title(titlestring);
191   legend('Measurement data','Data used for linear fit 1','Data used for linear
            fit 2','Linear fit 1','Linear fit 2','location','best');
192
193   %% SAVE LINEAR EXTRAPOLATION PLOT
```

```matlab
194  save_name_PDF = sprintf('%s_linear_extrapolation_for_SN_%s_at_%sbar.pdf',temp,
         SNpos,Pressure);
195  save_name_FIG = sprintf('%s_linear_extrapolation_for_SN_%s_at_%sbar.fig',temp,
         SNpos,Pressure);
196  savePathPDF = 'C:\Users\Truls\Documents\MATLAB_figures\PDF\TOF_analysis\
         Linear_extrapolation\';
197  savePathFIG = 'C:\Users\Truls\Documents\MATLAB_figures\FIG\TOF_analysis\
         Linear_extrapolation\';
198
199  Linear_fit_fig = tightfig(Linear_fit_fig);
200  pdf_save = strcat(savePathPDF, save_name_PDF);
201  saveas(Linear_fit_fig,pdf_save,'pdf');
202  figure_save = strcat(savePathFIG, save_name_FIG);
203  savefig(Linear_fit_fig,figure_save,'compact');
204
205  %% SAVE CP EDGE DETERMINATION INTERSECTION PLOT
206  save_name_PDF = sprintf('%s_CP_edge_determination_intersection_plot_for_SN_%
         s_at_%sbar.pdf',temp, SNpos,Pressure);
207  save_name_FIG = sprintf('%s_CP_edge_determination_intersection_plot_for_SN_%
         s_at_%sbar.fig',temp, SNpos,Pressure);
208  savePathPDF = 'C:\Users\Truls\Documents\MATLAB_figures\PDF\TOF_analysis\
         CP_edge_determination\';
209  savePathFIG = 'C:\Users\Truls\Documents\MATLAB_figures\FIG\TOF_analysis\
         CP_edge_determination\';
210
211  Intensity_intersection = tightfig(Intensity_intersection);
212  pdf_save = strcat(savePathPDF, save_name_PDF);
213  saveas(Intensity_intersection,pdf_save,'pdf');
214  figure_save = strcat(savePathFIG, save_name_FIG);
215  savefig(Intensity_intersection,figure_save,'compact');
```

Function: background.m

```matlab
1   % Function takes inn a integer number and a set of data arrays. The
2   % background is calculated from the first values of the data array up to
3   % the given integer. The background is returned.
4   function bground = background(l,A)
5   sum = 0;
6       for j=1:l,
7           sum = sum + A.data(j,2);
8       end
9
10  bground = (sum/l);
```

Function: get_TOF_files_from_SCAN.m

```matlab
1   % This function scans the folder structure for TOF files. The found
2   % TOF file names are added as string format to an array which is returned.
3   function TOF_files_transposed = get_TOF_files_from_SCAN(a)
4
```

```matlab
5        %a = text_array_from_SCAN_file(46:end,4);
6        TOF_files = {};
7        for i=1:length(a),
8            text_split1 = strsplit(a{i},'_')
9            text_split2 = strsplit(text_split1{2},'.')
10           dbl = str2num(text_split2{1});
11           str = num2str(dbl);
12           TOF_file = str
13           TOF_files = [TOF_files TOF_file];
14       end
15       TOF_files_transposed = transpose(TOF_files);
16   end
```

Function: Calculate_uncertainty_S.m

```matlab
1  % The function takes inn a file path, an array of TOF file names, an array
2  % of flight times, an array of full width at half maximums, an array of the
3  % uncertainty of the flight times and an array of the uncertainty of the
4  % full with at half maximum. This function uses these variables to
5  % calculate the speedratios of the TOF files and the uncertainty of the
6  % speedratios. An array of the speedratio uncertainties is returned.
7  function uncertainty_S = Calculate_uncertainty_S(path,TOFfile,flight_time,FWHM,
       delta_flight_time,delta_FWHM)
8      path_end = '\';
9      filename = sprintf('%s%sTOF_%d.dat', path,path_end,str2num(TOFfile));
10     headerend = '%end_header
           ###############################################################';
11     [C,A] = ImportData(filename,headerend);
12
13     strfreq = C{12};
14     linefreq = strsplit(strfreq,' ');
15     strtd = C{13};
16     linetd = strsplit(strtd,' ');
17     strtch = C{15};
18     linetch = strsplit(strtch,' ');
19     strLD = C{17};
20     lineLD = strsplit(strLD,' ');
21     strmaxL = C{18};
22     linemaxL = strsplit(strmaxL,' ');
23     stralpha = C{19};
24     linealpha = strsplit(stralpha,' ');
25
26     freq = str2double(linefreq{4});
27     delta_freq = 2;          %<--- guess
28     td = str2double(linetd{4});
29     tch = str2double(linetch{4});
30     LD = str2double(lineLD{5});
31     maxL = str2double(linemaxL{5});
32     alpha = str2double(linealpha{5})*(1e-6);
33
34     L = maxL - LD;
```

```matlab
35      delta_L  = 0.005;
36      tc = (alpha/freq)*(1E-6);
37
38      delta_alpha = 0.0005; %100*(1E-6); %<-- From fit
39      delta_t_d = 0;
40      delta_t_ch = 0.05*(1E-6);        %<--- Guess
41
42      delta_t_c = sqrt((((1/freq)^2)*((delta_alpha)^2))+(((-alpha/(freq^2))^2)*((
            delta_freq)^2)));
43      delta_t_f = sqrt(((delta_flight_time)^2) + ((delta_t_d)^2) + ((delta_t_c)
            ^2) +((delta_t_ch)^2)*((-1/2)^2));
44      S = 2.*sqrt(log(2)).*(flight_time/FWHM);
45      uncertainty_S = sqrt(((((2.*sqrt(log(2)))/FWHM)*delta_t_f).^2) + ((((-2.*
            sqrt(log(2)))/(FWHM.^2))*flight_time.*delta_FWHM)^2));
46      sprintf('S = %f +- %f',S,uncertainty_S)
47  end
```

CHECK LISTS FOR MAGIE

This appendix presents various check-lists on how to operate MAGIE, starting with a description on how to prepare MAGIE for measurements. Check-lists on how to conduct the virtual source measurements (Find beam), center line intensity measurements and time of flight measurements are presented. A check-list on how to shut down MAGIE after measurements is given, and finally a check-list on how to change the skimmers is presented.

B.1 Start-up procedure for MAGIE

1. Double check pressures. Values should roughly be the same as in table (B.1)

Gauge	Pressure [mbar]
PI-QK1	$9.9 \cdot 10^{-2}$
PI-QK2	$1.1 \cdot 10^{-1}$
P-QK1	$4.7 \cdot 10^{-4}$
PI-PST1	$1.1 \cdot 10^{-2}$
P-PST1	$2.9 \cdot 10^{-6}$
PI-CK	*Off*
P-CK	$2.9 \cdot 10^{-8}$
PI-IK	$2.1 \cdot 10^{-2}$
PI-SK1	$1.6 \cdot 10^{-2}$
P-SK	$2.0 \cdot 10^{-9}$
PI-PST2	$3.5 \cdot 10^{-2}$
P-PST2	$7.5 \cdot 10^{-9}$
PI-PIE1	$2.9 \cdot 10^{-2}$
PI-PIE2	$2.7 \cdot 10^{-2}$
P-PIE	$5.3 \cdot 10^{-7}$
PI-DK	$1.1 \cdot 10^{-2}$
P-DK	$4.8 \cdot 10^{-10}$

Table B.1: *shows typical pressure values for the pressure gauges on MAGIE. The values may vary, but should roughly be around the same pressure for MAGIE to function properly. The PI stands for Pirani gauges, while the P are the Penning and Bayart-Alpart gauges.*

2. Open up the valve between the source chamber and the chopper chamber: **CK-V**

3. Open up the valve between the chopper chamber and the mirror chamber: **SK-V**

4. Open up the valve for pumping stage 2: **PST2-V**

5. Open up the valve between mirror chamber and piezo chamber: **PIE-V**

6. Open up valve **DKV-V** (This should already be open, but open if it is not)

7. Turn on the power supply **FUC DC Power supply** by pressing the *ON* button

8. Turn on roots pumps **QK-Walzkp 1** and **QK-Walzkp 2** on **LT1**

9. Turn on surveillance for roots pumps **QK-Walzkp 1** and **QK-Walzkp 2** on **LT1**

10. Turn up the nozzle pressure to wanted pressure level (After set pressure, the high-vacuum pressure in the source chamber can be read off a pressure chart hanging on the left-hand side of rack **LT1**)

11. Start up LabVIEW software and go to temperature. Set the temperature to desired value

12. **OPTIONAL:** Power on the nozzle heating if this is required

B.2   Shut-down procedure for MAGIE

1. Turn off the nozzle heating if this is on

2. Turn down the nozzle pressure to $\sim 2\ bar$

3. Turn off surveillance for roots pumps **QK-Walzkp 1** and **QK-Walzkp 2** on **LT1**

4. Turn off roots pumps **QK-Walzkp 1** and **QK-Walzkp 2** on **LT1**

5. Turn off the power supply **FUC DC Power supply** by pressing the *ON* button (off when button is out)

6. Close the valve between the mirror chamber and the piezo chamber: **PIE-V**

7. Close the valve for pumping stage 2: **PST2-V**

8. Close the valve between the chopper chamber and the mirror chamber: **SK-V**

9. Close the valve between the source chamber and the chopper chamber: **CK-V**

B.3 Find beam

1. If MAGIE is not started up for measurements, follow the instructions in section (B.1) before continuing

2. On the LabVIEW software, open the **Counter** and turn on. Check if there is enough signal in the detector. If not, check that all valves are open, that the nozzle pressure is turned up and that no aperture or chopper disc is hindering the beam signal. Also check the detector sensitivity: $AB2$

3. Open **Find Beam** in the LabVIEW software

4. First thing to do is to run a reference run. To do so, press the **Reference Run** button. Wait until the program has settled before continuing

5. Move the beam position to the last stored position by pressing the **MOVE** button. Wait until the program has settled.

6. Go to the **Scan Crosswise** tab and do the following:

   - Set skimmer diameter
   - Set offset
   - Set the step size in which you want to scan (The resolution of the scan). The smaller the resolution, the longer the scan time due to an increase in measurement points

7. Press the **START** button and wait until the scan is finished (in both U- and V-axis)

8. Once the scan is complete, go to the **Evaluation** tab. Once there:

   - Place the marker in the middle of the graph. This can be done three different ways: By maximum, by plateau or by hand
   - Go to the other axis scan, either V or U depending on which axis you started with, and repeat the point above
   - Press the **MOVE AXIS** button, and write down the two positions of the axes.

9. Close the **Find beam** program

B.4 Time of flight measurements

Single Start-up and measurement

1. If MAGIE is not started up for measurements, follow the instructions in section (B.1) before continuing

2. Run a **Find Beam** (See section B.3)

3. Move chopper disc to desired starting point for TOF (~ 0.66 *inches*)

4. Turn on the chopper chamber water cooling system: **CK-CH** (This is a handle, located over by the source chamber, opposite where you set the nozzle pressure)

5. Turn on the chopper electronics: **CK Chopper** located on **LT2**

6. Open **Time of Flight** in the LabVIEW software. Go to the **Delay** tab, and input the temperature (Can be read off the temperature gauge on **rack 4**). Press the **Determine Delay** button and note down the delay time

7. Go to the **Info** tab, and get the best estimate for chopper frequency

8. Go to the **Chopper** tab, and set the frequency to the frequency you obtained from the point above by inputting the frequency, and press **Set Chopper**. The chopper disc will then ramp up (This takes a few minutes)

9. On the left-hand side of the **TOF** program, you can set the different parameters:

    - Check that the frequency is set to desired value. If not, go to the chopper tab and set this
    - Set the **Delay Time** as found earlier
    - Set the **Measure Time**
    - Set the **Channel Width** (the resolution of the scan)
    - Set the **No. of Channels** (Should be 400)
    - Set the **Distance LD**
    - Set the **Alpha minus** value, and make sure the turning direction is set to **Minus**

10. Press the **START** button and wait until the scan is finished

Multiple Scans Start-up and measurement

1. If MAGIE is not started up for measurements, follow the instructions in section (B.1) before continuing

2. Run a **Find Beam** (See section B.3)

3. Move chopper disc to desired starting point for time of flight (~ 0.66 *inches*)

4. Turn on the chopper chamber water cooling system: **CK-CH** (This is a handle located over by the source chamber, opposite where you set the nozzle pressure)

5. Turn on the chopper electronics: **CK Chopper** located on **LT2**

6. Open **Temperature** in the LabVIEW software. Input the desired temperature and press **Set Temperature**(Note that the nozzle heating has to be on if not room temperature measurement. Turn on Nozzle heating if not)

7. Open **Chopper** in the LabVIEW software. Input the desired chopper frequency and press **Set Frequency**

8. Open **Scan** in the LabVIEW software. Set the movement mode to **Point-by-Point**

9. Make sure that both the **Counter** and **TOF** is set to *ON*

10. Go to the **Counter** tab and do the following:

    - Set **N**
    - Set **No. of Cycles**
    - Set **Operation Mode** from *Program* to *OFF*

11. Go to the **TOF** tab and do the following:

    - Set the **Measure Time**
    - Set the **Channel Width** (the resolution of the scan)
    - Set the **No. of Channels** (Should be 400)
    - Set the **Distance LD**
    - Set the **Alpha minus** value, and make sure the turning direction is set to **Minus**
    - Check that the frequency is set to where you want it. If not, go to **Chopper** on the LabVIEW program and set this
    - Set the **Temperature** value. This can be done two ways: Automatically and by Input. If Auto is set, press **Determine Delay**. If input is set, input the temperature and press **Determine Delay**. These two methods will determine the delay time and automatically set this
    - Set the **Delay Time** as found earlier

12. Press the **START** button and wait until a window pops up. You can here enter a comment for each scan. For each time of flight, the chopper position is entered (Make sure chopper disc is set to correct CP value). Press **GO ON** and wait until the scan is finished

13. When the scan is complete, the window will pop up again. Change chopper position and input new CP value. Press **GO ON**. Continue this point until all desired CP values have been measured.

14. When all values have been measured, change from **GO ON** to **QUIT**

Shut-down TOF procedure

1. Go to **Chopper** and ramp down the frequency in intervals (in intervals of $\sim 100\ Hz$) until the frequency is set to $\sim 0\ Hz$

2. If temperature has been set, turn off nozzle heating

    - If cold beam scan, first set temperature to $\sim 70\ K$

3. When chopper frequency is down, shut off chopper electronics **CK-Chopper** on **LT2**

4. Turn off water cooling for the chopper: **CK-CH**

5. Remove chopper disc from beam line (Set CP to $\sim 1.4\ inches$)

6. If microscope is being shut down completely, follow instructions in section (B.2)

B.5   Center Line Intensity measurement procedure

If using skimmer for the first time

1. If MAGIE is not started up for measurements, follow the instructions in section (B.1) before continuing

2. Run a **Find Beam** (See section B.3)

3. Find the optimal position for the upstream pinhole aperture Φ : 400 μm:

   - Open **SCAN** on LabVIEW program

   - Set movement mode to **Point-by-Point**

   - Make sure the **Counter** is set to *ON*

   - Go to the **Counter** tab and set **N, No. of Cycles** and operation mode to **OFF**

   - Set the upstream pinhole aperture Φ : 400 μm to **10 mm** and press **START**

   - A window will pop up, and you input the current position of the pinhole aperture and press **GO ON**

   - The window will pop up again when finished, and you can change the position of the pinhole aperture (intervals of 5 mm should suffice). Input this and press **GO ON** again. Repeat until you see that the intensity has passed its maximum and returned to the background. Then change from **Continue** to **QUIT** and press **GO ON**

   - In the **Depict Measurement File** window on the LabVIEW software, go to **Evaluate**. Position the marker in the middle of the scan, and note down the position.

4. Set the upstream pinhole aperture Φ : 400 μm to the found optimal position

5. Find the optimal position for the downstream pinhole aperture Φ : 50 μm:

   - Repeat procedure in point 3, but set pinhole aperture to start at position **3 mm**

6. Set the downstream pinhole aperture Φ : 50 μm to the found optimal position

Measurement procedure

1. If MAGIE is not started up for measurements, follow the instructions in section (B.1) before continuing

2. Run a **Find Beam** (See section B.3)

3. Set upstream pinhole aperture Φ : 400 μm to the optimal position

4. Set downstream pinhole aperture Φ : 50 μm to the optimal position

5. Set **AB2** to **+1.6 V**

6. Open **SCAN** on the LabVIEW software

   - Select the movement mode to be **Point-by-Point**

   - Make sure the **Counter** is set to *ON*

   - Go to the **Counter** tab and set **N**, **No. of Cycles** and operation mode to **OFF**

   - Set nozzle pressure to 2 bar and press **START**

   - A window will pop up, and you input the current pressure value and press **GO ON**

   - The window will pop up again when finished, and you can change the nozzle pressure. Input this and press **GO ON** again. Repeat until you reach the desired pressure. Then change from **Continue** to **QUIT** and press **GO ON**

7. Set downstream pinhole aperture Φ : 50 μm to **14 mm** and repeat procedure in point 6 to make a background scan

Shut-down procedure

1. Close the LabVIEW program

2. Remove the downstream pinhole aperture Φ : 50 μm from the beam line

3. Remove the upstream pinhole aperture Φ : 400 μm from the beam line

4. If microscope is being shut down completely, follow instructions in section (B.2)

B.6 Source chamber venting procedure

1. Close valve **CK-V**

2. Turn off the nozzle heating if this is on

3. Reduce the nozzle pressure to ~ 2 *bar*

4. Open bypass valve **QK-VV2**

5. Turn off high voltage pressure measuring systems **PE-QK** and **PE-PST1**

6. Turn off surveillance systems **QK-WP1** and **QK-WP2** located on rack **LT1**

7. Turn off surveillance systems **QK-Turbo** and **PST1-Turbo** located on rack **LT1** and **LT2** respectively

8. Close pre-vacuum valves **QK-VV1** (Located in pump room) and **PST1-VV**

9. Turn off turbo pump **QK-Turbo** located on rack **LT1** and turn off turbo pump **PST1-Turbo** located on rack **LT2**

10. Wait $10 - 15$ minutes for the pumps to run down

11. When the pumps have stopped, vent the source chamber and pumping stage 1 by opening the bypass valve **QK-BV** (If the pumps have not completely stopped, open this valve by a short opening burst, and then close it again. Do this until its not noisy opening this valve)

12. While venting the source chamber, keep an eye on the pressure in the adjacent chopper chamber to make sure there is no leak from the valve closed between the two chambers.

13. After the venting is complete, close the bypass valve **QK-BV**

B.7 Source chamber pumping procedure (Starting up after venting)

1. If the bypass valve **QK-BV** is still open, close it

2. Open the pumping stage 1 pre-vacuum valve **PST1-VV**

3. Wait until **PI-PST1** and **PI-QK** are smaller than 30 *mbar* (On the gauges this shows as $3 \cdot 10^1$)

4. Open the source chamber pre-vacuum valve **QK-VV1** (Located in the pump room)

5. Turn on roots pumps **QK-Walzkp 1** and **QK-Walzkp 2** on **LT1** to help speed up the pumping process

6. Wait until **PI-QK** and **PI-PST1** is smaller than 0.1 *mbar* (On the gauges this shows as $1 \cdot 10^{-1}$)

7. Turn on the turbo pumps **QK-Turbo** and **PST1-Turbo** (**NOTE**: The turbo pump **QK-Turbo** has to be restarted several times because it shuts itself off after a while. When the pump stops, press the white restart button. Continue to do this until the pump is stable)

8. Turn on the High-pressure measurement gauges (Press the **HV** button) for the source chamber and pumping stage 1 (**NOTE:** Before turning these on, make sure that the upper green light on the source chamber turbo pump **QK-Turbo** is lit. If not, the gauges will not start)

9. Wait until the pumps are completely run up, and then turn on surveillance systems for the source chamber turbo pump **QK-turbo** and pumping stage 1 **PST1-Turbo**

10. Close bypass valve **QK-BV2** when the surveillance systems and pumps are fully operational

11. Turn off roots pumps **QK-Walzkp 1** and **QK-Walzkp 2** on **LT1**

UNCERTAINTY

The uncertainty of a non-linear multi-variable function with N variables is obtained by finding the absolute uncertainty propagation with respect to the N variables. Taking the absolute value of the first term of a Taylor series expansion of function y, with respect to each variable and multiply with the variable uncertainty, the uncertainty of a non-linear multi-variable function is obtained:

$$\Delta y = \left| \frac{\partial y}{\partial x_1} \right| \Delta x_1 + \left| \frac{\partial y}{\partial x_2} \right| \Delta x_2 + ... + \left| \frac{\partial y}{\partial x_{N-1}} \right| \Delta x_{N-1} + \left| \frac{\partial y}{\partial x_N} \right| \Delta x_N \qquad (C.1)$$

This equation can be extended to an overall standard deviation formula, given by equation C.2 [46].

$$\sigma\left(y\right) = \sqrt{\left(\frac{\partial y}{\partial x_1}\sigma\left(x_1\right)\right)^2 + \left(\frac{\partial y}{\partial x_2}\sigma\left(x_2\right)\right)^2 + ... + \left(\frac{\partial y}{\partial x_{N-1}}\sigma\left(x_{N-1}\right)\right)^2 + \left(\frac{\partial y}{\partial x_N}\sigma\left(x_N\right)\right)^2}$$
$$(C.2)$$

The uncertainty of the speedratio

As mentioned in section (4.2), the speedratio is defined by equation (2.17):

$$S = 2 \cdot \sqrt{ln(2)} \cdot \frac{t_f}{\Delta t} \;=\; 2 \cdot \sqrt{ln(2)} \cdot \frac{v_t}{\Delta v_t}. \qquad (2.17)$$

To find the uncertainty of equation (2.17), we can use the error propagation equation shown in equation (C.2). Utilizing this, we find that $\Delta\left(S\right)$ is given by:

$$\Delta\left(S\right) = \sqrt{\left(\frac{\partial S}{\partial t_f} \cdot \Delta\left(t_f\right)\right)^2 + \left(\frac{\partial S}{\partial \Delta t} \cdot \Delta\left(\Delta t\right)\right)^2} \qquad (C.3)$$

where $\Delta\left(t_f\right)$ is the uncertainty of the flight time, and $\Delta\left(\Delta t\right)$ is the uncertainty of the full width at half maximum. The full expression for the uncertainty of the speedratio ends up being:

$$\Delta\left(S\right) = \sqrt{\left(\frac{2 \cdot \sqrt{ln\left(2\right)}}{\Delta t} \cdot \Delta\left(t_f\right)\right)^2 + \left(-\frac{2 \cdot \sqrt{ln\left(2\right)}}{\Delta t^2} \cdot \Delta\left(\Delta t\right)\right)^2} \qquad (C.4)$$

Uncertainty of the flight time

As stated in section (4.2.1.1), the equation for the time of flight is given by equation (4.6):

$$t_f = t_p + t_d - t_c - \frac{t_{ch}}{2} \tag{4.6}$$

The peak time t_p was determined as the center point of our Gaussian fit. The uncertainty of t_p, $\Delta(t_p)$ was also given by the fit, and when we calculate the uncertainty of the flight time, we include the uncertainty of the delay time t_d in the peak time uncertainty (The same as saying that $\Delta(t_d) = 0$). The uncertainty of the channel width, $\Delta(t_{ch})$, is set to 0.05 μm. The uncertainty of the correction time changes depending on the alpha value and the frequency used for the time of flight measurement, and is given by the equation (C.5).

$$\Delta(t_c) = \sqrt{\left(\frac{1}{f_{ch}} \cdot \Delta\alpha\right)^2 + \left(-\frac{\alpha}{f_{ch}^2} \cdot \Delta f_{ch}\right)^2} \tag{C.5}$$

The uncertainty of the frequency is 2 Hz, while the uncertainty of the α-value changes depending on the skimmer used. For both the 390 μm skimmer and the 4 μm skimmer, the uncertainty of alpha was $\Delta(\alpha) \sim 500 \ \mu m$. Utilizing equation (C.2) we find an expression for the uncertainty of the flight time:

$$\Delta(t_f) = \sqrt{\Delta(t_p)^2 + \Delta(t_d)^2 + \Delta(t_c)^2 + \left(\frac{1}{2} \cdot \Delta(t_{ch})\right)^2} \tag{C.6}$$

Uncertainty of the terminal velocity

In section (4.2) it was shown that the terminal velocity was given by equation (4.4):

$$v_t = \frac{L}{t_f} \tag{4.4}$$

where L was the distance from the chopper disc to the detector and t_f the time of flight. The distance L is read off a scale on the side of the microscope, and has an uncertainty of 0.005 m. Applying equation (C.2) to equation (4.4) gives us the uncertainty of the terminal velocity:

$$\Delta(v_t) = \sqrt{\left(\frac{1}{t_f} \cdot \Delta(L)\right)^2 + \left(-\frac{L}{t_f^2} \cdot \Delta(t_f)\right)^2} \tag{C.7}$$

The speed of the atoms depends strongly on the temperature of the nozzle. The temperature is regulated with an automated controller and can be read off of a display screen on the control panel. The uncertainty of the temperature is stated to be $\pm \ 0.1° \ K$ in the data sheet, but due to instability in the controller and the temperature gauge not placed at the exact place of expansion, the uncertainty of the temperature is set to $\pm \ 0.5° \ K$.

Bibliography

[1] R. Hooke, *Micrographia: or Some Physiological Description of Minute Bodies, Made by Magnifying Glasses with Observations and Inquiries Thereupon.* (James Allestry, 1665).

[2] E. Abbe, "Contributions to the theory of the microscope and of microscopic perception," *Archive for Microscopic Anatomy*, vol. 9, no. 1, 1873.

[3] N. M. AB, "*Ernst Ruska - Biographical*," Wed. June 11th 2015.

[4] H. Pauly, *Atom, Molecule, and Cluster Beams I.* Berlin, Heidelberg, Germany: Springer-Verlag Berlin Heidelberg, 1st edition ed., 2000. Chapter 1, p. 1 - 34, ISBN: 978-3-540-66945-6.

[5] A. Kantrowitz and J. Grey, "A high intensity source for the molecular beam. part i. theoretical," *Review of Scientific Instruments*, vol. 22, no. 5, 1951.

[6] U. Buck, *Atomic and Molecular Beam Methods Volume I.* Oxford, New York, United States: Oxford University Press, 1st edition ed., 1988. Chapter 18, p. 449 - 471, ISBN: 978-0-195-04280-1.

[7] D. Farias and K. Rieder, "Atomic beam diffraction from solid surfaces," *Repors on Progress in Physics*, vol. 61, no. 12, 1998.

[8] T. Reisinger and B. Holst, "Neutral atom and molecule focusing using a fresnel zone plate," *Journal of Vacuum Science and Technology*, vol. B 26, no. 2374, 2008.

[9] R. B. Doak, R. E. Grisenti, J. P. Toennies, S. Rehbein, G. Schmahl, and C. Woll, "Towards realization of an atomic de broglie microscope: Helium atom focusing using fresnel zone plates," *American Physical Society Journals*, vol. 83, no. 21, 1999.

[10] M. Koch, S. Rehbein, G. Schmahl, T. Reisinger, G. Bracco, W. E. Ernst, and B. Holst, "Imaging with neutral atoms—a new matter-wave microscope," *Journal of Microscopy*, vol. 229, no. 1, 2008.

[11] P. Witham and E. Sánchez, "A simple approach to neutral atom microscopy," *American Institute of Physics Journals*, vol. 82, no. 103705, 2011.

[12] J. Braun, P. K. Day, J. P. Toennies, G. Witte, and E. Neher, "Micrometer-sized nozzles and skimmers for the production of supersonic he atom beams," *Review of scientific Instruments*, vol. 68, no. 8, 1997.

[13] D. P. DePonte, S. D. Kevan, and F. S. Patton, "Brightness of micronozzle helium source," *Review of Scientific Instruments*, vol. 77, no. 055107, 2006.

[14] S. D. Eder, *A Neutral Matter Wave Microscope (NEMI): Design and Setup.* PhD thesis, University of Bergen, 2011.

[15] A. Einstein, "On a heuristic point of view about the creation and conversion of light," *Annalen der Physik*, vol. 17, no. 132, 1905. Translated version published in American Journal of Physics v. 33, n. 5, May 1965.

[16] J. W. J. Jr. and T. A. Serway, *Physics for Scientists and Engineers with Modern Physics.* Boston, MA: Cengage Learning, 8th edition ed., 2010. ISBN: 978-1-4390-4875-7.

[17] P. A. Tipler and R. A. Llewellyn, *Modern Physics.* Houndmills, Basingstoke RG21 6XS, England: W. H Freeman and Company, 5th edition ed., 2008. ISBN: 978-0-7167-7550-8.

[18] F. Dunning and K. Winkelmann, *Atomic, Molecular, and Optical physics: Atoms and Molecules*, vol. 28B. San Diego: Academic Press Inc., 1996. ISBN: 978-0-12-475976-9.

[19] J. P. Toennies and K. Winkelmann, "Theoretical studies of highly expanded free jets: Influence of quantum effects and a realistic intermolecular potential," *Journal of Chemical Physics*, vol. 66, no. 3965, 1977.

[20] H. Pauly, *Atom, Molecule, and Cluster Beams I.* Berlin, Heidelberg, Germany: Springer-Verlag Berlin Heidelberg, 1st edition ed., 2000. ISBN: 978-3-540-66945-6.

[21] E. Lillestøl, O. Hunderi, and J. R. Lien, *Generell Fysikk for Universiteter of Høgskoler Bind 2: Varmelære og Elektromagnetisme.* Oslo, Norway: Universitetsforlaget, 2nd edition ed., 2006. ISBN: 978-82-15-00006-0.

[22] T. Reisinger, G. Bracco, S. Rehbein, G. Schmahl, W. E. Ernst, and B. Holst, "Direct images of the virtual source in a supersonic expansion," *The journal of physical chemistry*, vol. 111, no. 49, 2007.

[23] S. D. Eder, G. Bracco, T. Kaltenbacher, and B. Holst, "Two dimensional imaging of the virtual source of a supersonic beam: Helium at 125 K," *The Journal of Physical Chemistry A*, vol. 118, no. 1, 2014.

[24] G. Scoles, D. Bassi, U. Buck, and D. Lainé, *Atomic and Molecular Beam Methods Volume I.* Oxford, New York, United States: Oxford University Press, 1st edition ed., 1988. ISBN: 978-0-195-04280-1.

[25] D. Bassi, *Atomic and Molecular Beam Methods Volume I.* Oxford, New York, United States: Oxford University Press, 1st edition ed., 1988. Chapters 7 and 8, p. 169 - 192, ISBN: 978-0-195-04281-8.

[26] U. Hefter and K. Bergmann, *Atomic and Molecular Beam Methods Volume I.* Oxford, New York, United States: Oxford University Press, 1st edition ed., 1988. Chapter 9, p. 193 - 253, ISBN: 978-0-195-04281-8.

[27] M. Zen, *Atomic and Molecular Beam Methods Volume I.* Oxford, New York, United States: Oxford University Press, 1st edition ed., 1988. Chapter 10, p. 254 - 273, ISBN: 978-0-195-04281-8.

[28] M. Greve, "*Testing nano structured Fresnel zoneplates for neutral helium microscope on a supersonic expansion in a ultra high vacuum apparatus*," Master's thesis, University of Bergen, 2010.

[29] E. Hecht, *Optics*. 1301 Sansome St., San Francisco: Addison Wesley, 4th edition ed., 2002. ISBN: 0-321-18878-0.

[30] D. Brandon and W. D. Kaplan, *Microstructural Characterization of Materials*. Technion, Israel Institute of Technology, Israel: John Wiley and Sons, 2nd edition ed., 2008. ISBN: 978-0-470-02785-1.

[31] A. Apfolter, "*Wiederaufbau und test einer He-Streuapparatu und erste Streuexperimente an amopher sowie kristalliner SiO2-Oberflache*," Master's thesis, Technische Universität Graz, 2005.

[32] T. Reisinger, "*Fresnel atom-optics experiments with a supersonic helium beam*," Master's thesis, Graz University of Technology, 2007.

[33] B. Holst and W. Allison, "An atom-focusing mirror," *Nature*, vol. 390, no. 6657, 1997.

[34] M. Koch, "*2D He Beam Microscopy using Fresnel Zone Plates in an UHV Molecular Beam Apparatus*," Master's thesis, Graz University of Technology, 2006.

[35] O. L. Vacuum, "Fundamentals of Vacuum Technology." Brochure, 2007.

[36] J. Daintith, *A dictionary of physics*. Oxford: Oxford University Press, 6th edition ed., 2010. ISBN: 9780199233991.

[37] S. R. Systems, "Hot vs. Cold Ionization Gauges: Which One is Best for Me?." Application note.

[38] R. V. Hogg and E. A. Tanis, *Probability and Statistical Inference*. Upper Saddle River, New Jersey 07458: Pearson Education, Inc., 8th edition ed., 2010. ISBN: 978-0-321-63635-5.

[39] D. J. Auerbach, *Atomic and Molecular Beam Methods Volume I*, ch. 14 - Velocity Measurements by Time-of-flight Methods. In [24], 1st edition ed., 1988. ISBN: 978-0-195-04280-1.

[40] H. Pauly, *Atom, Molecule, and Cluster Beams II*. Berlin, Heidelberg, Germany: Springer-Verlag Berlin Heidelberg, 1st edition ed., 2000. ISBN: 978-3-540-67673-7.

[41] J. L. Luneng, "*Low-energy surface vibration measurements on the alpha-quartz (0001) surface*," Master's thesis, University of Bergen, 2011.

[42] A. S. Palau, S. D. Eder, T. Kaltenbacher, B. Samelin, and B. Holst, "A modified speed ratio evaluation method for time-of-flight measurement of an atom beam." Unpublished paper, 2015.

[43] R. A. Adams and C. Essex, *Calculus: A complete course*. Toronto, Ontario, Canada: Pearson Canada Inc., 7th edition ed., 2010. ISBN: 978-0-321-54928-0.

[44] B. Samelin, *Neu- und Weiterentwicklung von Elektronenstossionisationsdetektoren*. PhD thesis, Georg-August-Universität zu Göttingen, 1993.

[45] G. Bracco and T. Kaltenbacher, "Time of flight simulations." Private communication, 2015.

[46] J. P. Bentley, *Principles of Measurement Systems*. Essex CM20 2JE, England: Pearson Education Limited, 4th edition ed., 2005. ISBN: 978-0-130-43028-1.